SEMICONDUCTOR QUANTUM DOTS FOR MID-IR LIGHT EMISSION

BY

LAN YU

DISSERTATION

Submitted in partial fulfillment of the requirements
for the degree of Doctor of Philosophy in Electrical and Computer Engineering
in the Graduate College of the
University of Illinois at Urbana-Champaign, 2016

Urbana, Illinois

Doctoral Committee:

Associate Professor Daniel Wasserman, Chair
Professor Gary Eden
Professor Xiuling Li
Associate Professor Minjoo Lawrence Lee

ABSTRACT

Mid-infrared wavelength range (3 μm to 30 μm) is important in many applications such as environmental monitoring, industrial process control, biomedical imaging, security and defense. The mid-IR is the spectral home of the distinct vibrational and rotational absorption resonance signatures of a wide range of molecular species, giving mid-IR sensing systems the potential to enable the monitoring and identification of molecules for gas sensing or chemical and biological imaging applications. To enable many of the above applications, compact, high efficiency, and low-cost mid-IR emitters and detectors are required. The goal of this project is to develop highly efficient and low-cost mid-IR emitters.

The first part of this thesis gives an introduction to why mid-IR light is important and the state-of-the-art mid-IR sources. We discuss the working theory, structure, advantages and disadvantages of quantum cascade laser (QCL), interband cascade laser and type-I quantum well lasers, which together cover the wavelength range from 2 μm to 11 μm. Then, in the last part of chapter 1, we provide an introduction to quantum dots and a discussion as to why we might want to use quantum dots to improve the performance of QCLs. Here we will discuss primarily two types of quantum dots: those that are generally referred to as patterned (either etched top down, or site-selectively grown), and self-assembled QDs (SAQD). In this project, we studied studied mechanisms for control of energy states in both top-down nanolithographically defined QD and bottom-up InAs submonolayer QD grown by MBE.

We demonstrate strong carrier confinement in, and electroluminescence (EL) from, quantum nanostructures fabricated from epitaxially grown quantum wells (QWs) using a top-down nanosphere lithography (NSL), dry-etch, mass-transport, and overgrowth fabrication process. Optically active nanopillars with diameters as small as 90 nm are fabricated, and narrow linewidth

(18 meV) electroluminescence from a fabricated diode structure is observed, with an emission blue-shift of over 37 meV from the original quantum well sample luminescence. The results presented offer the potential for low-cost, large-area patterning of quantum nanostructures for optoelectronic applications. However, the NSL defined QD density is limited by the size of the NS used. For 200 nm diameter size NS, the QD density can only reach to $2.5 * 10^9/\text{cm}^2$ which is likely not nearly high enough for most optoelectronic applications. For this reason, we started to study InAs submonolayer quantum dots (in the next chapter), aiming to use InAs SML QD in the QCL active region.

The thesis then goes on to discuss work demonstrating control of energy states in epitaxially-grown quantum dot structures formed by stacked submonolayer InAs depositions via engineering of the internal bandstructure of the dots. Transmission electron microscopy of the stacked submonolayer regions shows compositional inhomogeneity, indicative of the presence of quantum dots. The quantum dot ground state is manipulated not only by the number of deposited InAs layers, but also by control of the thickness and material composition of the spacing layers between submonolayer InAs depositions. In this manner, we demonstrate the ability to shift the quantum dot ground state energy at 77K from 1.38 eV to 1.88 eV. The results presented offer a potential avenue towards enhanced control of dot energies for a variety of optoelectronic applications. The SML QD structures were then integrated into QCL-like structures, with our SML deposition in the active region.

We also demonstrate infrared light emission from thin epitaxially grown In(Ga)Sb layers in InAs(Sb) matrices across a wide range (3-8 μm) of the mid-infrared spectral range. Our structures are characterized by x-ray diffraction, photo-electron spectroscopy, atomic force microscopy and transmission electron microscopy. Emission is characterized by temperature- and power-dependent infrared step-scan photoluminescence spectroscopy. The epitaxial In(Ga)Sb layers are observed to form either quantum wells, quantum dots, or disordered quantum wells, depending on the insertion layer and substrate material composition. The observed optical properties of the monolayer scale insertions are correlated to their structural properties, as determined by transmission electron and atomic force microscopy.

In this work, we employ time resolved PL to study the carrier recombina-

tion mechanism in a thin type II material system. With the experimental system we set up and the analysis process developed, we are able to resolve the Shockley-Read-Hall and radiative rates from our materials. This provides a powerful way to study the emitter quality. According to our TRPL study as well as the optical study, we find that the sample with obvious nanostructure formation has the best optical performance and material quality, which makes the QD structure the best candidate for mid-IR emitter and laser applications.

Finally, the thesis ends with a study of the growth of InGaSb QDs using MBE by systematically changing growth parameters such as substrate temperature, Ga/In ratio and layer thickness. A high density and high uniformity QD sample is grown and studied at the end of chapter 6. This sample shows a better temperature performance and a better material quality than any other samples without QD formation. From this work we are able to draw the conclusion that the type-II QD structure has the best potential in the future to be made into a low-cost, simple structure and high-performance room-temperature mid-IR emitters.

To my parents, Zhihai Yu and Xin Wen, and to my wife, Xinran Yu, for their love and support

ACKNOWLEDGMENTS

I thank Professor Daniel Wasserman for helping me with great patience and knowledge. It is an honor to be your first PhD student at UIUC. In the past five years, I can feel my growth from a fresh graduate student knowing nothing to a person who can deal with all the equipment in the cleanroom, doing all kinds of semiconductor fabrication processes with no problem, operating and fixing the MBE system, setting up all kinds of visible and mid-IR optical systems and, more importantly, solving research problems by logical thinking and checking the literature. All the things I know are due to the guidance from my dear advisor, Professor Wasserman. Without you, I would not have made such a great improvement.

I also thank Professor Lee and his student Dr. Daehwan Jung since we had a very good time collaborating on the InAs QW laser project. I started to work with your group in the first year of my PhD life and it has been five years. I cannot remember how many PL samples I have tested for you, how many EL emitters I have fabricated and tested and how many laser bars I have fabricated and tested, but I do remember each time when we made some progress, how happy we were.

I thank my committee members, Professor Gary Eden and Professor Xiuling Li, for your patience and help in my prelim exam.

I thank Professor Eden; your talk with me about our God inspired me and made me think more about God and eventually open my heart to God.

I thank my group mates Will Streyer, Runyu Liu, Yujun Zhong, Sukrith Dev, Dan Zuo, Narae Yong and Andrew Taylor for their help in the past five years. I will never forget the days and nights spent together in the lab or in the cleanroom.

Special thanks to my family, my parents and my wife. Words are powerless to express how grateful I am to be in this family.

Finally I thank my God, my eternal Father, for being with me and guiding

me through all the difficulties. I can feel you every day and everywhere. I have faith in you and I will keep on trusting you for my future. Thank you, my Lord.

TABLE OF CONTENTS

CHAPTER 1

INTRODUCTION

1.1 Mid-Infrared Light

The mid-infrared (mid-IR) is generally considered to be the wavelength range from 2 to 30 μm, as shown in figure 1.1. Within this range, we can identify regions of the mid-IR with particular technological importance. Commonly, the mid-IR range can be divided into three subdivisions: short wavelength IR (SWIR, 1.4 μm to 3 μm), middle wavelength IR (MWIR, 3 μm to 8 μm) and long wavelength IR (8 μm to 30 μm). Each wavelength range has its own applications. SWIR is widely used in long distance communication (1550 nm)[1], in agriculture, for food product quality control, in astronomy, for cool star detection (large red giant stars and low mass red dwarfs) and in materials science, for thin film thickness measurement. MWIR is of great importance for military applications (heat guided missile), astronomy (locating dark asteroids) and environmental monitoring. LWIR is the region for thermal imaging, which can be used for night vision and bio-imaging. In the next section, we will discuss why mid-IR is becoming more important nowadays.

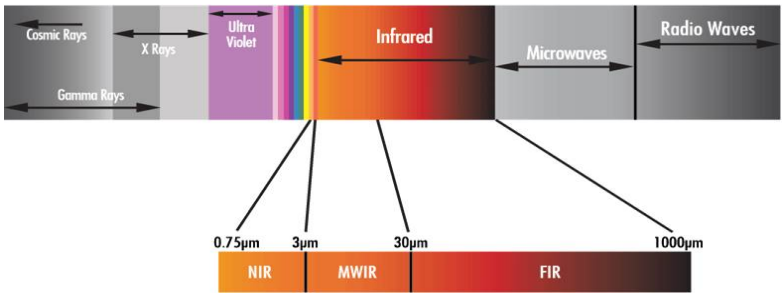

Figure 1.1: Infrared spectrum [2].

1.2 Molecular Vibration

The mid-IR is the home to vibrational and rotational resonances of molecules, and this is largely responsible for the mid-IR's technological importance. A molecular vibration can be treated using Newtonian mechanics using a spring-mass model, which obeys Hooke's law. It occurs when the bond between atoms within a molecule moves. Taking the liquid water molecule as an example, usually, the molecule has six vibrational modes, as shown in figure 1.2 [3]. Molecular vibrations can be excited when the molecules are

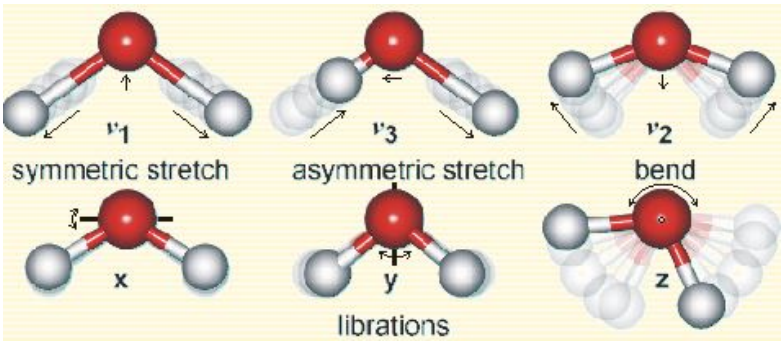

Figure 1.2: Six vibrational modes for water molecule [3].

excited at one of the resonant energies associated with the various atomic bonds (spring/masses) in the molecule. In such a situation, the molecule will absorb incident energy. Technically, there needs to be some dipole associated with the bond. Each molecule will have a unique absorption spectrum dependent on its composition and bonding. For many technologically vital molecules, the majority of these absorption lines fall in the mid-IR. Mid-IR spectroscopy is the technique used to study the infrared region, mostly based on absorption and transmission spectroscopy. The ability to produce mid-IR spectrum and identify molecules makes mid-IR spectroscopy a powerful tool for applications such as gas sensing, pollution control and chemical detection. Figure 1.3 shows the absorption spectra of seven molecules [4]. The instrument most frequently used for mid-IR spectroscopy is the Fourier transform infrared (FTIR) spectrometer. The traditional IR spectroscopy systems are dispersive type. Using a prism or grating, they can separate each frequency of light emission from the broadband IR source. The detector measures the light intensity of each frequency transmitted through the samples resulting in a spectrum of intensity versus wavelength. Because dispersive measurement

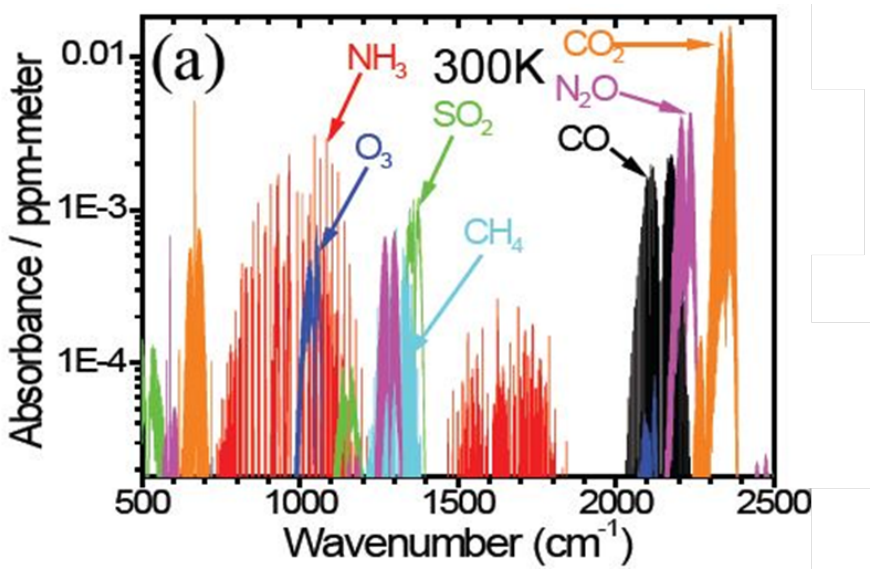

Figure 1.3: Absorption spectra of seven molecules [5].

requires scanning through all the frequencies of interest, it usually takes a long time for a single scan. Also, it is not efficient for time-resolved measurement of biopsies since one can only take scans one after another. Fourier transform infrared (FTIR) spectroscopy was then developed to overcome the disadvantages of dispersive tools. By adapting a powerful optical device, the interferometer, FTIR is able to measure all the frequencies simultaneously, and it only takes a couple of minutes to do a measurement. There are also several other advantages of the FTIR instrument. One advantage is that the optical throughput of FTIR is much higher (referred to as the Jacquinot advantage), leading to higher signal-to-noise ratio. The other is that the commercialized FTIR employs a HeNe reference laser in order to internally calibrate the wavelength (referred to as the Connes advantage), which makes it more convenient to use. By using a broadband mid-IR light source for wide range detection or a narrow line width mid-IR light source to probe an individual molecule, the absorption can be measured through the FTIR system and so the kind of molecule can be determined [6]. Since all living creatures and all room-temperature objects have radiation in the mid-IR wavelength range — for instance, the human body emits at about 10 μm — mid-IR detection can be used for applications such as environment monitoring (figure 1.4(a)), security and defense (figure 1.4(b)) and energy conservation (figure 1.4(c)). Given all the possible applications for mid-IR wavelength range, the

need for high-efficiency, low-cost and wavelength-flexible mid-IR light sources and detectors is growing dramatically. The following sections will introduce a few mature mid-IR light sources developed nowadays.

Figure 1.4: Several applications for mid-IR light: (a) Environmental monitoring, (b) homeland security [7], (c) home energy auditing [8].

1.3 State-of-the-Art Mid-IR Sources

1.3.1 Quantum Cascade Laser

In 1994, Federico Capasso's group at Bell Labs demonstrated the first quantum cascade laser (QCL) grown by molecular beam epitaxy (MBE), emitting at 4.2 μm [9]. The QCL has been intensively studied and developed in the past 20 years. Though the initial QCL only operated at low temperature (10 K) in pulsed operation, since that time, the QCL has been demonstrated across the mid-IR, operating CW, at room temperature (and above) with output powers as high as a few watts and efficiencies over 50% [10]. Today, the QCL is a commercially available light source (Daylight, Hamamatsu, etc.) which can be integrated into a range of mid-IR systems. The inherent wavelength flexibility of the QCL comes from the ability to use bandstructure engineering to design inter-sub-band (ISB) transitions across a wide range of the mid-IR. The most common material system (InGaAs/AlInAs lattice-matched to InP) offers QCLs with emission wavelengths from 5 μm to 9 μm [11]. Strain balanced QCLs offer larger band offsets and thus shorter wavelength operation (3 μm to 5μm) [12], and alternative material systems, such as GaAs/AlGaAs and AlAsSb/InGaAs, allow for the extension of QCL emission wavelengths to the long and short wavelength extremes of the mid-IR

[13]. This wavelength flexibility also makes the QCL an attractive mid-IR light source widely used in different fields, such as chemical sensing, drug development, open-path gas sensing and IR spectroscopy [14]. In the past few years, QCLs have been developed to emit at continuous wave, room-temperature with high output power [15],[16],[17]. The QCL has a number of advantages over bandgap diode lasers for mid-IR emission. Figure 1.5 shows the electron transition and photon emission in the active region of a traditional quantum well diode laser (a) and in the active region of a quantum cascade laser (b). The emitted photon energy for the QW diode laser is limited by the bandgap energy of the QW material, while for the QCL it does not have this limitation. The most popular narrow-band semiconductor material is InAs, having a band gap of 0.354 eV (3.5 μm in wavelength) at room temperature. InSb, with a band gap of 0.17 eV (7.3 μm), can potentially be used for mid-IR devices, but it is not lattice-matched to any of the substrate semiconductor materials, making the growth of coherent emitters with InSb very challenging, due to the lack of lattice-matched wave-guide cladding or electron confinement materials. Figure 1.6 shows a typical band structure of two periods in a GaAs/AlGaAs quantum well QCL. An electron transported through such a structure travels through multiple periods, each of which consists of an injector, an active region, and an extraction region. The electron has the potential to generate a photon in the active region of each period of the device. The energy states in the injector region are designed to match with the upper electron state in the following active region under bias so that the electron can be easily injected into the active region from the previous injector. Once the electron tunnels through the barrier between the injector and the active region and occupies the upper energy state in the active re-

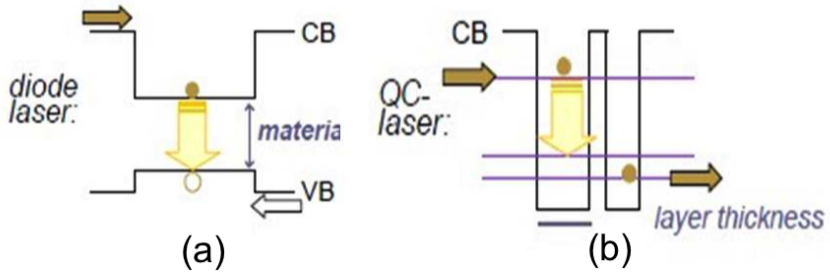

Figure 1.5: Electron transition and band structure for (a) traditional diode laser and (b) quantum cascade laser [18].

gion, it will transit to the lower energy state, emitting a photon with energy equal to the energy difference between the two energy states. Then, the electrons now in the lower energy state will be depopulated to the ground state very quickly and tunnel into the next injector. In order to have population inversion in the laser active region, which is one of the critical conditions for lasing, the energy difference between the lower state and the ground state is designed to be equal to the phonon energy in the material (34 meV for InGaAs/InAlAs). This dramatically decreases the electron lifetime in the lower state to sub-nanosecond (0.2-0.4 ps in GaAs/AlGaAs system), which is very short compared with the electron lifetime in the upper state (3-5 ps in GaAs/AlGaAs system), making population inversion possible under bias, as the population of the lower state depletes via phonon emission, while the upper state is filled by current injection, and depletes much more slowly. The

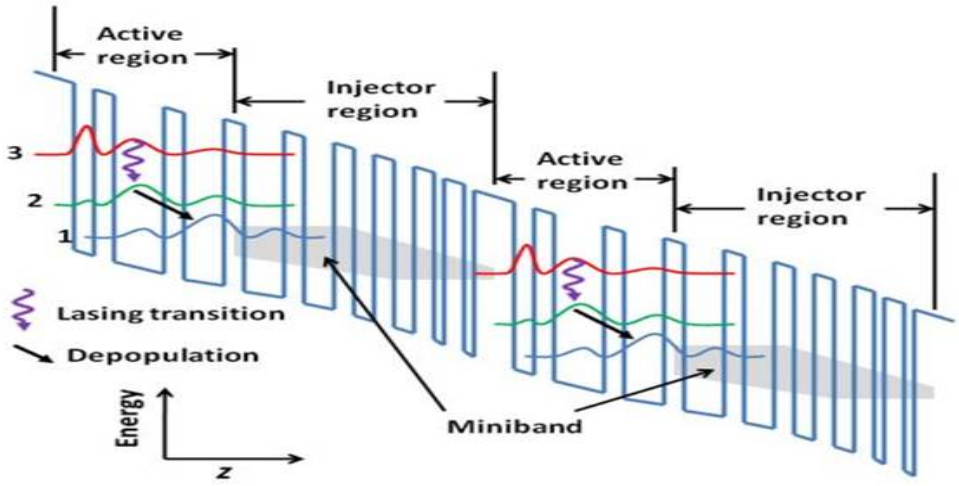

Figure 1.6: Typical band structure of a GaAs/AlGaAs quantum cascade laser active region [19].

most important advantages of QCL are, as mentioned before, the flexibility in controlling emission wavelength, as well as the high output power, since the output power increases as the number of periods increases. However, there are also some limitations for quantum cascade lasers. First, it is very hard to design a QCL with an emission wavelength shorter than 4 μm. In order to have shorter emission wavelength, the energy difference between the upper state and lower states shown in figure 1.6 needs to be larger, which pushes the upper state closer to the conduction energy band edge of the bar-

rier material. Once this upper state energy comes too close to the barrier conduction band, carriers will thermalize out of the laser upper state, diminishing laser performance and eventually preventing lasing altogether. One possible material for shorter wavelength QCL right now is a nitride-based system. Although the intersubband transitions in such a material system were observed by Gmachl in 2000 [20], it is very difficult to engineer ISB emission due to internal electrical fields in the III-nitrides material system. Also, the growth of complex GaN/AlGaN/InGaN semiconductor structures is not mature, so there is still a long way to go before the first quantum cascade structure can be demonstrated for a nitride-based material system. Secondly, without out-coupling structures, QW QCLs cannot be made into surface-emitting devices because of the optical selection rule. Optical transitions in QCLs, where the carriers are confined in the growth (z) direction, will have a dipole moment only in the z-direction. This means that the QCL can only emit light with an electric field polarized in the growth direction (what is typically referred to as TM-polarized light). In addition, the short non-radiative carrier lifetime caused by phonon scattering results in weak subthreshold emission and high threshold current density in the QCL, limiting the wall-plug efficiency of these devices. So far, the highest recorded QCL wall-plug efficiency is about 50%, by Gmachl [10], which is still low compared with the traditional diode laser, with an efficiency larger than 70% for GaAs based diode lasers [21]. The combination of the short carrier lifetime (weak sub-threshold emission) and the TM-polarized emission makes QCLs particularly poor light emitters below the lasing threshold. Thus, the QCL is not suitable for applications requiring the mid-IR equivalent of a light-emitting diode. This has important ramifications for a number of sensing applications which would benefit from efficient mid-IR light emission, but do not require the narrow-band, coherent emission of a laser.

1.3.2 Interband Cascade Laser

The interband cascade laser (ICL), as an alternative mid-IR light source to QCL for slightly shorter wavelengths, takes advantage of the type-II band alignment of the InAs/Ga(In)Sb material system. The ICL was proposed in 1994, the same year the QCL was first demonstrated [22]. The first ICL proposed had a single type-II interface (InAs/GaInSb) in the active region and was soon replaced by a W configuration (figure 1.7, active region) containing two InAs electron QWs on either side of a GaInSb hole QW. Since then, the W structure has become a standard design for the ICL active region. It is believed, but has yet to be proven, that the W structure can reduce the non-radiative recombination rate and increase gain, due to the electron-hole wavefunction overlap [23]. In 2008, the Naval Research Laboratory (NRL) reported the first ICL operating cw at room temperature [24], and that was also the first time lightly doped GaSb separate confinement layers (SCL) were introduced into the ICL laser structure to reduce waveguide loss. Recently, research groups have put significant effort into improving ICL threshold cur-

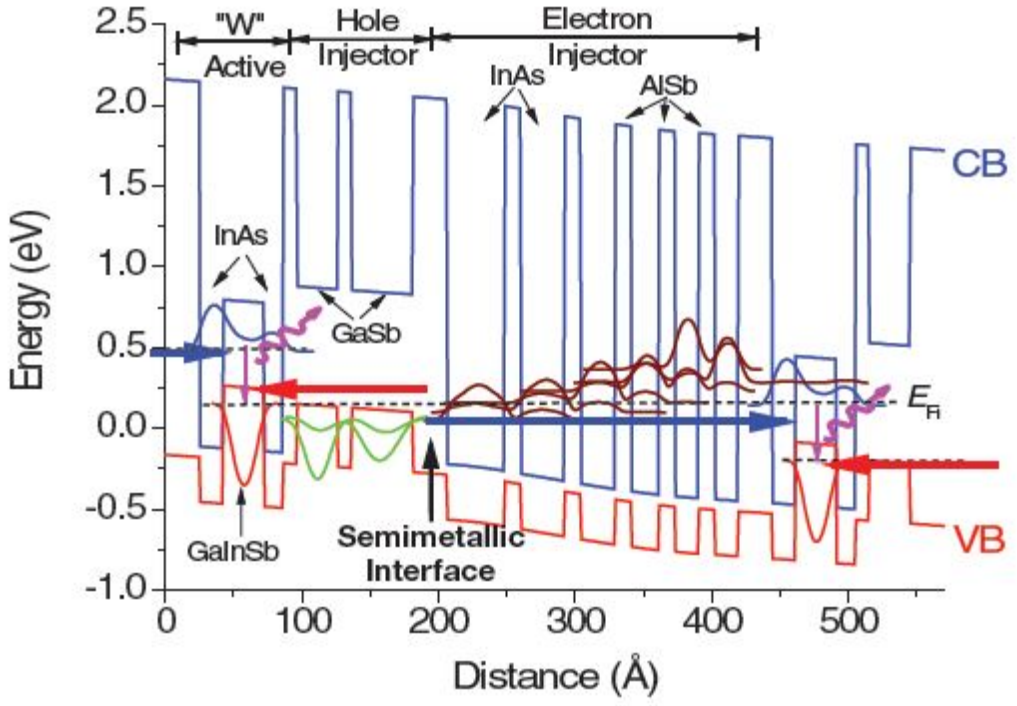

Figure 1.7: Typical band structure of a type-II interband cascade laser active region [23].

rent densities and wall-plug efficiencies, leading to the development of the carrier rebalancing concept. Figure 1.7 shows a standard ICL band structure. A single stage includes three regions: an electron injector, providing electrons into the InAn QW; a hole injector, providing holes into the GaInSb QW; and an active region where electrons and holes recombine and emit photons. The reason type-II band alignment is used in the active region is that the electron and hole recombine from two different materials, what is known as a diagonal transition. In such a diagonal, type-II, transition, the energy of the emitted photon is not limited by any bandgap, enabling the emission to be in mid-IR wavelength range.

One other important design to dramatically improve the performance of ICL is the introduction of a semimetallic interface (SMIF, shown in figure 1.7) between narrow-band type-II materials. The concept of SMIF is that, when applying an external field, the lowest conduction band edge (InAs in this case) is pushed farther down and becomes lower than the highest valence band edge (GaSb in this case). Carriers can be separated under this external field so that electrons can fill in the InAs QW state to the right and holes can fill in Ga(In)Sb QW to the left. The advantage of the SMIF structure is that the hole injector does not need to be highly doped. The presence of a heavily doped tunnel junction in each period of the laser can induce severe internal optical absorption. By removing this layer, the laser designer can minimize the free carrier losses [25].

The design of the hole injector is also very critical for ICL. It has been proven that two GaSb QWs are better than one QW in the hole injector region in terms of preventing electrons in the active region from tunneling into the electron injector, essentially leaking out of the active region. In addition, the AlSb barrier used has to be thin, usually 1 to 1.2 nm, to assure hole transport [25]. Unlike the traditional diode lasers, the optical waveguide design for ICL is tricky due to its unique active region structure. The goal is to minimize the internal loss as well as increase the threshold gain. Since all the hole carriers are provided internally within the laser core region, the laser cladding layers on each side of the active core can be n-doped, resulting in lower free carrier absorption loss. Figure 1.8 shows a simulated refractive index and mode intensity (for the fundamental transverse electric mode (TE_0)) profile of a typical ICL design. The introduction of n-doped GaSb SCL on

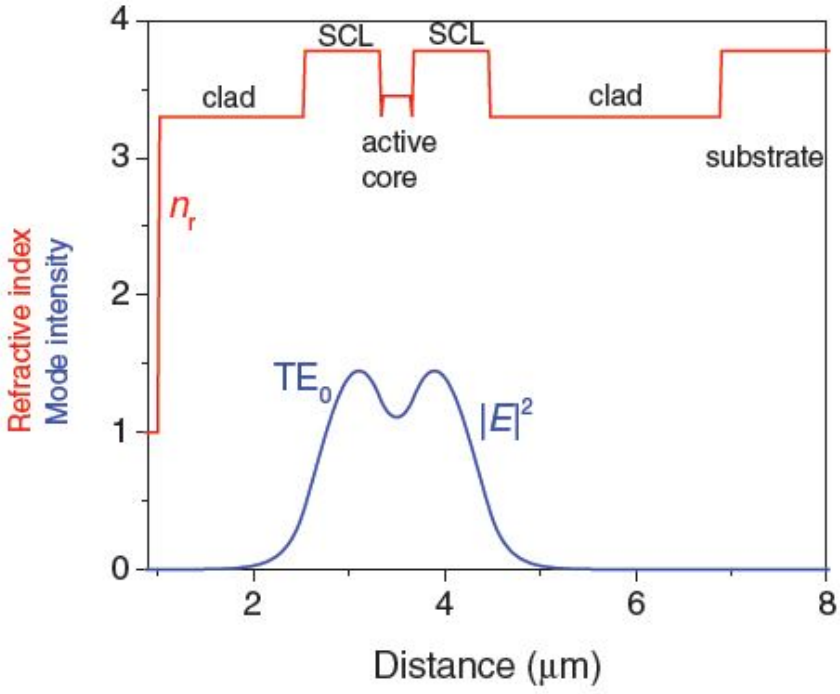

Figure 1.8: Simulated refractive index and mode intensity profile of a typical ICL design [25].

each side of the active core region dominates the mode, because of its higher refractive index, which prevents the mode from leaking into the cladding layers, providing improved confinement to the core, and greater overlap with the laser active region. Compared to ICL designs without the SCLs, the optical confinement factor (Γ) in the active core and the cladding decreases for the ICL with SCL. Although more study is still needed to better understand the internal loss in the active core region, it is believed that it dominates the total loss in modern ICL design [26]. So the reduction of optical confinement factor in the active core is beneficial for laser performance, and this is proved experimentally by NRL in 2008 [24]. One advantage of ICL over QCL is that it emits TE polarized photons, enabling this structure to be made into a surface-emitting device without out-coupled gratings. In the past ten years, researchers have put great effort into improving the ICL performance in the 3 to 4 μm wavelength range. There is still room for improving laser performance outside that region, by better cascade and waveguide design to lower the loss.

1.3.3 Type-I Quantum Well Lasers

One possible way to cover the short wavelength region of the mid-IR wavelength range is through the use of narrow-band-gap material with a type-I band alignment. Such a material system would be the mid-IR equivalent of the near-IR/visible diode lasers so essential for our modern communication and imaging infrastructure. Diode lasers, with quaternary material GaInAsSb QW in the AlGaAsSb matrix as active region, have been fabricated and characterized to cover wavelengths from 1.9 μm to 3.4 μm in the past few years [27]. Those lasers also can operate in CW mode at room temperature. A few factors limit the performance of these narrow-band type-I QW lasers. Free-carrier absorption and Auger recombination cause high temperature sensitivity of these devices. In addition, carrier leakage and thermal population in the active region result in undesirable high threshold current and low output power. It has been proven that a stronger carrier confinement in these structures can reduce the deficiency and improve the laser performance. Due to the nature of narrow-band material band alignment, one can easily design a QW structure providing effective electron confinement, since a large conduction band offset can be easily achieved ($>$ 300 meV). However, this is not the case for holes. The valence band offset in these material systems is too small to provide adequate hole confinement. If the holes are loosely bound, the heavy hole sub-band separation will be small ($<$ 15 meV) so that the higher order hole subbands as well as the states in the barrier can increase the density of states available for carrier population, which then leads to a shift of the quasi-Fermi levels and results in a higher threshold current density [32]. So the key point to decrease the threshold current for room temperature operation is to provide better hole confinement so that the number of states available in the valence band can be minimized. According to [33],[29], there are two popular ways to achieve this goal. First, decreasing the fraction of As in the InGaAsSb QW can introduce more compressive strain to further split the heavy and light hole states and at the same time push up the valence band edge to gain more valence band offset. Figure 1.9(a) shows two designs for the QW; the one with less As (9%) in the QW (GaInAsSb) has more strain (1.5%) than that with more As (17%). Figure 1.9(b) is the threshold current density of these two strained QW lasers as a function of temperature. It is obvious that at high temperatures, the device

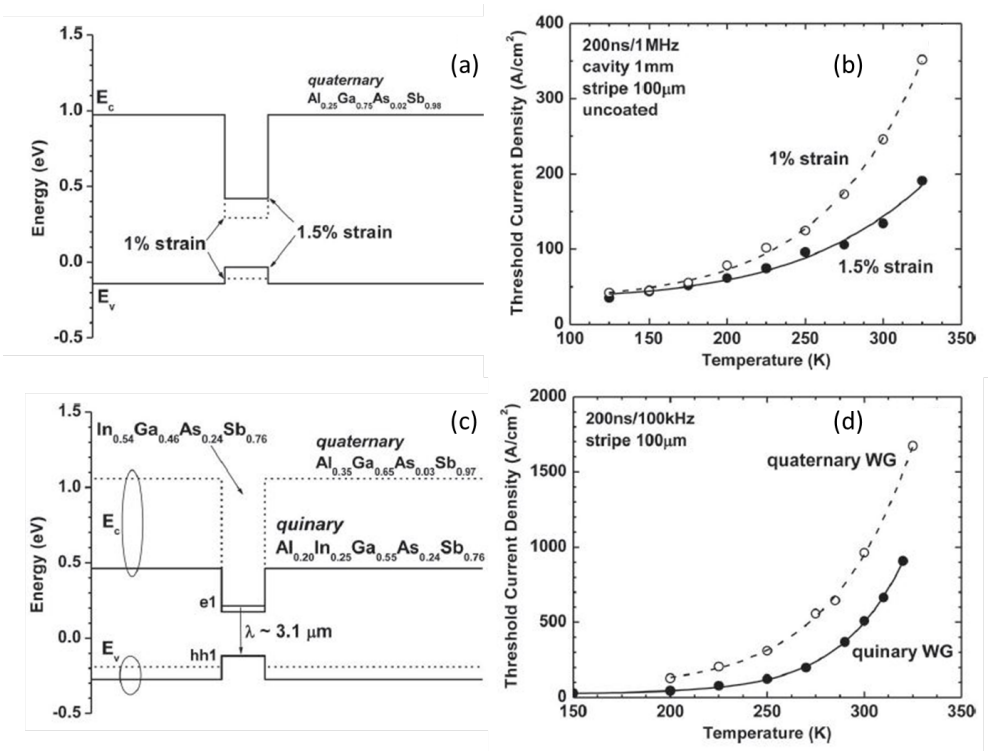

Figure 1.9: (a) Simulated band diagram of compressively strained QWs [28] [29]. (b) Threshold current density as a function of temperature for two strained QW laser design. (c) Simulated band diagram for quaternary and quinary QW lasers [30]. (d) Threshold current density as a function of temperature for two lasers with quaternary and quinary barriers [31].

with the 1.5% strained QW has only half of the threshold current density of the 1.0% strained device. It is also expected that at low temperatures, the threshold current difference is not very obvious because the barrier state population decreases exponentially as temperature drops. The second way to improve hole confinement is using quinternary material (AlInGaAsSb) instead of quaternary material (AlGaAsSb) as the barrier. As shown in figure 1.9(c), adding indium in the barrier material improves the hole confinement by 100 meV. Although the electron confinement has been weakened, it is still more than enough to keep the electron state deeply bound. Experimental results indicate that the threshold current drops to 900 A/cm^2 for the quinternary barrier device from 1700 A/cm^2 for the quaternary device [33],[29]. The side effect of using more complicated quinternary material is that the growth becomes even more difficult, making this device difficult to produce for low-cost commercialization.

Figure 1.10 shows a light current voltage (LIV) curve of a state-of-the-art type-I quantum well laser emitting at 3.2 μm. The output power of this laser is 165 mW at room temperature for CW mode and the threshold current density is 400 A/cm^2. It has three GaInAsSb QWs and has quinternary AlGaInAsSb material in the barrier and waveguide. For type-I diode lasers, it is almost impossible to go beyond 3.5 μm. The reason for this limitation is that in order to achieve shorter wavelength operation, the QW material needs to have smaller bandgap, which requires a greater In component in the QW material while at the same time maintaining low As percentage. This directly increases the lattice constant of the QW material and makes it very hard to grow high-quality material.[34]

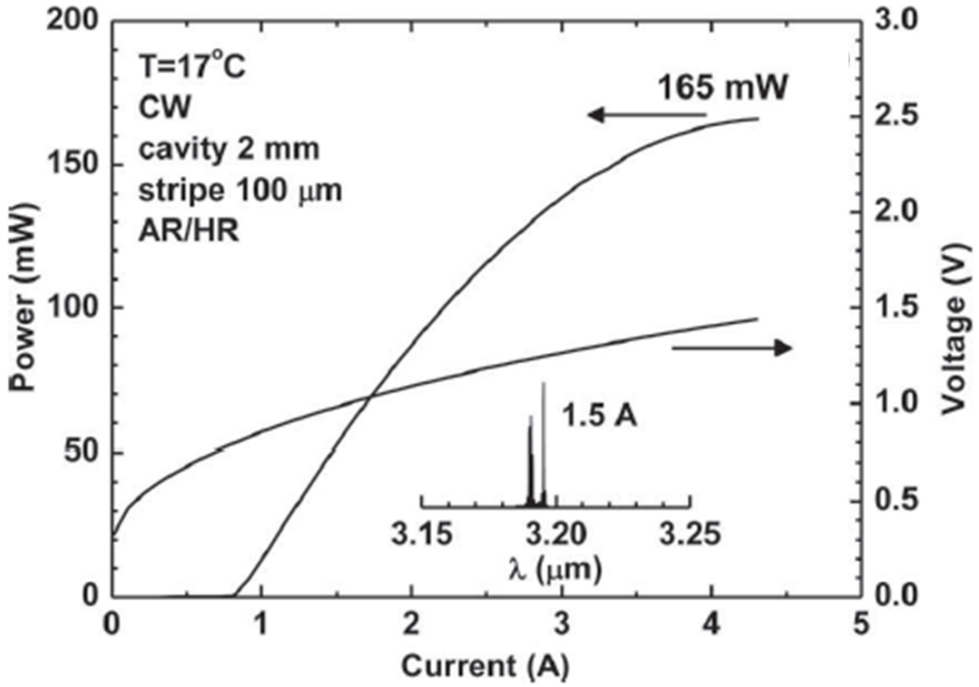

Figure 1.10: Light-IV curve measured of a type-I QW laser operating at room temperature, cw mode, emitting at 3.2 μm. Inserted is the lasing spectrum of a 2 mm long, 100 μm wide, AR/HR coated laser bar [34].

1.4 Quantum Dots

The ability to confine charge carriers in nanoscale structures results in a quantization of the energies associated with motion in the direction of the quantization. By nanostructuring material, we can effectively control the energy states of charges in the materials. This is perhaps the key characteristic of nanomaterials, namely the control of electronic and optical properties by control of length scales, not simply the bulk material properties. Quantum dots are nanostructured materials which confine electrons in all three dimensions, as opposed to quantum wells (1D) or quantum wires (2D confinement). The 3D confinement provided by quantum dots (QDs) has been shown to have the potential to improve the performance of electronic and optoelectronic devices such as lasers, detectors and biological sensors. The 3D confinement associated with QDs will result in a δ-function density of states (DOS). This means that charge carriers will only be allowed at discrete energy levels, as opposed to the continuum of states associated with the densities of state for QWs and Qwires. This δ-function DOS will result in unique transport and optical properties, which allow QDs to be used as an optical gain medium with a low threshold current density and narrow gain bandwidth. In addition, QDs with high uniformity and quality hold the potential for optical encoding and multiplexing applications because of their narrow linewidth emission spectrum. Quantum dots have been fabricated using a wide range of techniques and materials, such as colloidal QDs, top-down lithographically defined QDs, bottom-up grown QDs and self-assembled

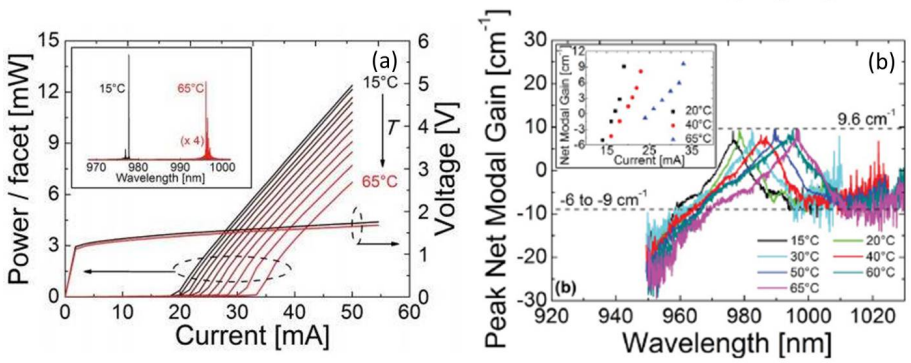

Figure 1.11: (a) Light-IV curve characteristics measured of a InAs/GaAs QD interband laser, emitting at 978 nm, cw mode. Inserted is the laser spectral. (b) Peak net modal gain calculated using Hakki-Paoli method [35].

QDs. Self-assembled quantum dots (SAQDs) grown by molecular beam epitaxy (MBE) or metal-organic chemical vapor deposition (MOCVD), formed in strongly lattice-mismatched systems where three-dimensional islands form to reduce the mismatch strain, have many favorable properties for device applications such as lasers and photodetectors. Since SAQDs have reasonably high uniformity even without lithography and can be integrated into semiconductor optoelectronics, significant effort has been made to research and develop SAQD-based optoelectronic devices for a variety of applications. Figure 1.11(a) shows the L-IV curve of an InAs/GaAs submonolayer (SML) QD laser, reported in 2012, emitting at 978 nm, CW mode, at room temperature, with a threshold current density of 900 A/cm^2, a characteristic temperature $T_0 = 101$ K and a peak output power of 12 mW [35]. Compared with a InGaAs QW laser device emitting at the same wavelength, the QD laser has slightly better T_0 value (97 K for QW laser), but higher threshold current density. Figure 1.11(b) is the peak net modal gain curve calculated by Hakki-Paoli (HP) method. The internal loss of this QD laser is remarkably low, only -6 to -9 cm^{-1}. The net modal gain is 9.6 cm^{-1} even at 65 ^{o}C without saturation. In addition, one can observe that the gain curve has a linewidth of about 15 meV, narrow compared with previously reported results. [35]

Recently, researchers have managed to fabricate InAs quantum dot lasers on silicon substrates, with the help of a germanium buffer layer. The L-IV

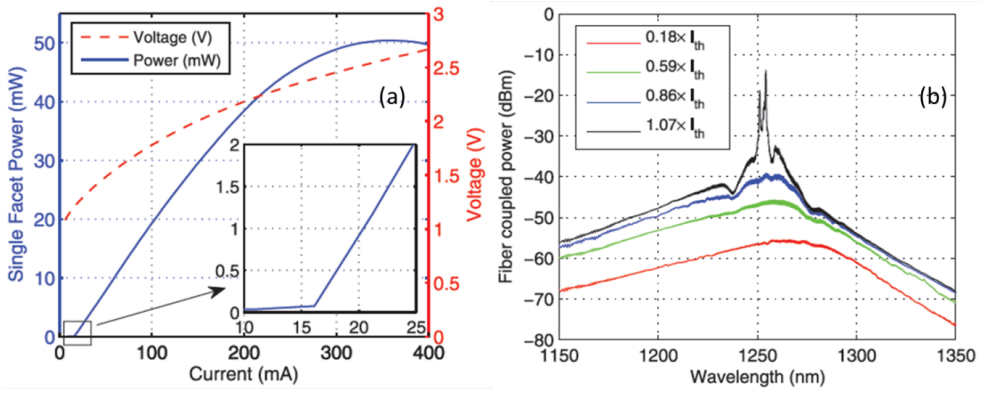

Figure 1.12: (a) Light-IV curve characteristics measured for an InAs QD laser grown on silicon substrate with Ge buffer, emitting at 1250 nm. Inserted is the L-I curve zoomed in at threshold. (b) Emission spectra at different currents [35].

curve and laser spectra are shown in figure 1.12 for a InAs QD laser grown on Si substrate, reported in 2014. This laser operates in CW mode, with a threshold current density of 430 A/cm^2, and a T_0 = 143 K from 20 ^{o}C to 40 ^{o}C. It can operate in CW mode from room temperature all the way up to 113 ^{o}C, which is the record for lasers grown on silicon substrate. Since this laser emits at 1.33 μm and has a high output power of 176 mW, it can, with further development, potentially be used for telecommunication applications in the future [36].

1.5 Quantum Dot Quantum Cascade Laser

As mentioned previously, the non-radiative recombination times between the energy states in the conduction band of a QW QCL can be very fast (a few ps), which limits the wall-plug efficiency of QCL. In addition, without any out-coupling structures, it is not possible to achieve surface emission due to the selection rules for optical transitions in the QCL active region. One way to enable both longer recombination times (and thus lower threshold current density) and surface emission is to replace the QWs in the QCL active region with QDs, as shown in figure 1.13. The 3D confinement of the QD allows for transitions between conduction band states in the QD to emit photons in the growth direction (as long as the quantization of the states' energies comes from the lateral confinement in the QD). Consider the intersubband

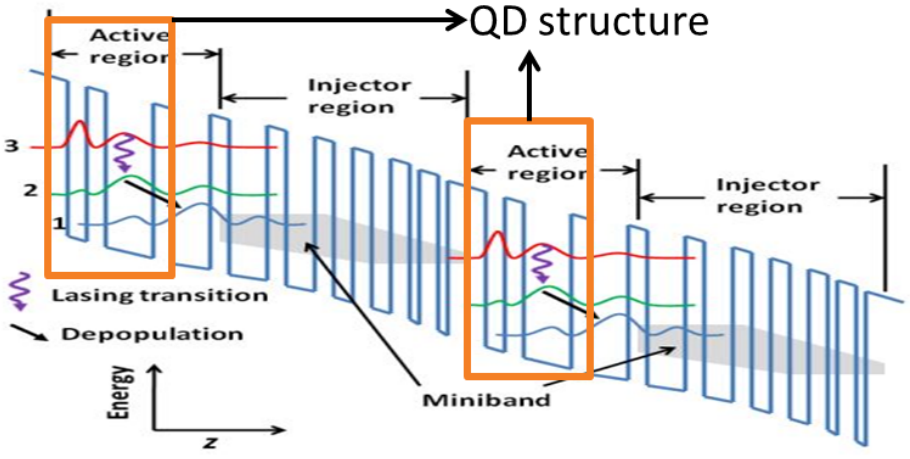

Figure 1.13: Quantum dots quantum cascade laser structure.

transition between energy state Ψ_a and state Ψ_b, of which the wavefunctions are:

$$\Psi_a = u_c(\vec{r})\phi_1(x, y, z) \tag{1.1}$$

$$\Psi_b = u_c(\vec{r})\phi_2(x, y, z) \tag{1.2}$$

Here u_c refers to the periodic parts of the Bloch functions, ϕ_1 and ϕ_2 are the envelope wave functions of electrons in two energy states. For QWs, the wavefunctions can be further simplified as:

$$\Psi_a = u_c(\vec{r})\frac{e^{i\vec{K}_t\cdot\rho}}{\sqrt{A}}\phi_1(z) \tag{1.3}$$

$$\Psi_a = u_c(\vec{r})\frac{e^{i\vec{K'}_t\cdot\rho}}{\sqrt{A}}\phi_2(z) \tag{1.4}$$

The optical dipole moment is then given by:

$$\mu_{ba} = \langle\psi_b \mid e\vec{r} \mid \psi_a\rangle = \delta_{vecK_t,vecK'_t}\langle\phi_2 \mid ez \mid \phi_1\rangle\hat{z} \tag{1.5}$$

The optical dipole moment of QD is given by:

$$\mu_{ba} = \langle\psi_b \mid e\vec{r} \mid \psi_a\rangle = \langle\phi_2 \mid ex \mid \phi_1\rangle\hat{x} + \langle\phi_2 \mid ey \mid \phi_1\rangle\hat{y} + \langle\phi_2 \mid ez \mid \phi_1\rangle\hat{z} \tag{1.6}$$

Due to equations 1.5 and 1.6, the dipole moment of QW has a component only in the z direction (growth direction) while that of the QD is non-zero in all three directions, so the absorption coefficient $\alpha(\hbar\omega)$ is not zero for both TE polarization (x, y direction) and TM polarization (z direction) for the QD. Therefore, using the QD in a cascade structure will benefit both the quantum dot cascade laser (QDCL) and the quantum dot infrared photodetector (QDIP). In addition, the atom-like delta function DOS of quantum dots in the active region can make the emission linewidth very narrow if the QDs are very uniform and can make the non-radiative recombination between electron energy states more difficult, which is also called the phonon bottleneck effect. The phonon bottleneck effect can be explained as follows: Relaxation lifetime of electrons in the higher energy state in a QD structure is much longer than that in a QW structure, when the energy difference between the two energy states is much larger than LO phonon energy. This is mostly caused by the atom-like delta-function DOS in the 3-dimensionally confined

QD structure. The phonon bottleneck effect (PBE) has been demonstrated experimentally by several research groups and most of the results show that the relaxation time can be more than 100 times as long as that in a QW structure. Although it has been shown that PBE can weaken the emission intensity of an intraband QD device if sufficient hole carriers are not provided, the increased carrier lifetime will improve the gain of a QDCL, which will also lower the threshold current density, reduce the heat in the active region and improve the performance of the laser device. In order to illustrate the improvement of QDCL compared with QCL, we can calculate the gain for intersubband transition system:

$$g_{Q(D)CL} \propto \tau_{2Q(D)CL}(1 - \frac{\tau_{1Q(D)CL}}{\tau_{21Q(D)CL}})\frac{d^2_{21Q(D)CL}}{\lambda_{Q(D)CL}\Delta E_{Q(D)CL}}\zeta_{Q(D)CL} \tag{1.7}$$

where τ_2 is the upper energy state lifetime, τ_1 is the lower energy state lifetime, τ_{21} is the transition time between upper and lower energy states, d_{21} is the dipole matrix element, λ is the wavefunction, ΔE is the linewidth and ζ is the filling factor for the quantum active region. If we use a very conservative estimate of the lifetimes for QCL from the literature, we will have:

$$\frac{g_{QDCL}}{g_{QCL}} \approx 21\frac{\zeta_{QDCL}\Delta E_{QCL}}{\zeta_{QCL}\Delta E_{QDCL}} \tag{1.8}$$

Therefore, if we can fabricate a QD with high uniformity and high density and use it in the quantum cascade structure, we will be able to improve the gain of the QCL by an order of magnitude, which will also lead to lower threshold current densities, as well as improved device temperature performance.

CHAPTER 2

EXPERIMENTAL SETUP

Over the course of my PhD work, I used a variety of measurement techniques to characterize the many samples and devices grown and fabricated. In this chapter I describe the experimental set-ups used in this work. Most generally, these can be categorized as i) optical and ii) material characterization systems. Typically the material characterization techniques (AFM, XRD, SEM) are used to understand the as-grown materials, usually in terms of the physical properties of the material (surface topography, material quality, etc.). The optical techniques also provide insight into material quality, with a focus on the optical characteristics of the materials. These can be broken into two separate sub-categories: first, the near-IR/visible techniques, which give information regarding the energy spacing between states in the valence and conduction band of larger bandgap materials, and are thus used to better understand samples designed for intersubband transitions; and second, techniques for investigating the mid-IR properties of our samples, emphasizing the optical properties associated with the transitions designed to give mid-IR emission.

2.1 Visible and Near IR PL Setup

Our visible and near-IR (NIR) PL system is used to characterize the optical properties of nanosphere lithographically defined QDs in chapter 3 and the submonolayer QDs of chapter 4. Figure 2.1 is a schematic of our visible/NIR PL setup. A 50 mW, 532 nm diode-pumped solid state laser is used to pump our sample. The laser light is first passed through a 532 nm band-pass filter and split by a beam-splitting cube, directing approximately half of the light toward the sample. The transmitted light is sent to a beam block. The light reflected towards the sample is focused by a 15x microscope objective into

the cryostat. The sample emission is collected by the same objective lens and passed through the beam splitter, and is then focused by a 2" diameter, 5" focal length lens into a Horiba Jobin-Yvon iHR320 spectrometer, through a series of long-pass filters (600 nm, 650 nm) designed to remove the 808 nm and 1064 nm light used by the laser to generate the 532 nm signal). The light is dispersed by a single grating (150, 300, 1200 lines/mm) onto a liquid nitrogen-cooled charge coupled device detector. This setup provides invaluable information as to the positions of the lowest energy states in the valence and conduction bands of our larger bandgap materials.

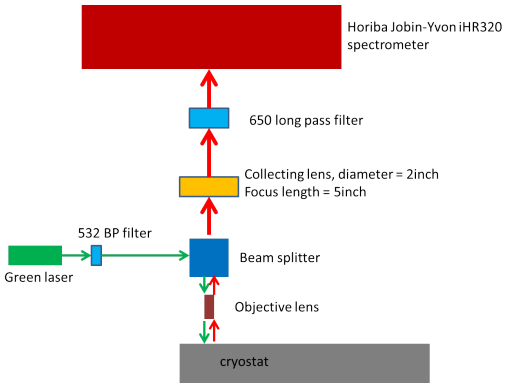

Figure 2.1: Configuration of our visible/NIR PL system.

2.2 Mid-IR PL Setup

The majority of our mid-IR spectral characterization is performed by Fourier transform infrared (FTIR) spectroscopy. There are four main components of a typical FTIR: the source, the Michelson interferometer, the detector and the computer. Usually, a commercial FTIR will use a blackbody source, often referred to as a globar, which provides broadband emission across much of the mid-IR spectrum. The globar is typically used as the mid-IR source for transmission and reflection measurements. However, I primarily used the FTIR to study emitter devices. In this case, the IR light comes from the emitter, not the globar, and is sent from the external sample to the interferometer of the FTIR, and the globar is turned off so as to not interfere with the measurements. The broadband light emitted by the light source will go into the heart of the FTIR, which is the Michelson interferometer, as shown

in figure 2.2. The incoming light is split by a beam splitter (BS), after which half of the light goes to a stationary mirror and the other half goes to a moving mirror. The beams reflected by the two mirrors go through the beam splitter and then focus on the sample, when used in a reflection or transmission measurement. Once this light either reflects from or passes through the sample, it is collected by a mid-IR detector (most often a HgCdTe (MCT) photodetector. If the light under investigation is the cource itself, then the recombined light passing through the beamsplitter is focused directly on the mid-IR detector. The moving mirror creates a difference in optical length between the two beams (known as the retardation) split by BS. An interferogram is obtained by moving the mirror, thereby changing the retardation and at the same time recording the signal from the detector. This interferogram gives a record of light intensity as a function of path length difference. The Fourier transform of this signal then becomes the spectrum of the light source incident upon the interferometer.

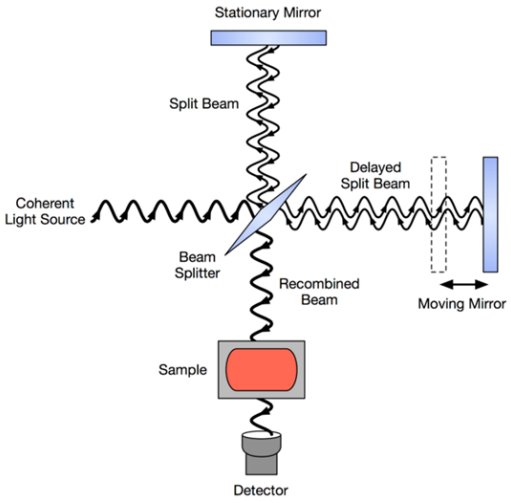

Figure 2.2: Configuration of a typical Michelson interferometer used in FTIR.

There are two scanning modes for a typical FTIR: rapid-scan mode and step-scan mode. For the rapid-scan measurement, the FTIR sweeps the moving mirror very quickly and averages many interferograms. The rapid scan technique is ideal for measurements with large light signals, able to provide high resolution spectral data from strongly emitting samples, or alternatively, when the internal source is used in a reflection or transmission measurement. For weak signals, however, rapid scan is not particularly useful because the

background thermal signal (from the optics or the FTIR itself, for example) can easily overwhelm the weak signal from the sample of interest. In such a situation, we typically utilize a step-scan measurement technique, which allows for a significant improvement in signal-to-noise ratio. In step scan, the moving mirror of the interferometer is scanned in discrete steps, and held at a given position for a fixed amount of time. In amplitude-modulation step scan, the technique employed in this thesis, the amplitude of the source to be measured is modulated either by modulating the electrical or optical excitation, or alternatively, by chopping the emitted light with a beam chopper. The signal detected at a fixed mirror position by the internal FTIR detector is then taken from the FTIR to a lock-in amplifier, which is synched to the modulation of the sample under test. The LIA then returns a DC signal to the FTIR, and it is this DC signal that is recorded for the fixed mirror position. The mirror then steps to the next position and slowly builds the interferogram with each step. Because an MSS only records signals modulated at the frequency of the source, the broadband thermal background that can overwhelm small signals is removed, giving an order of magnitude improvement in S/N. This significant improvement, however, does come at the cost of speed and spectral resolution, which are limited by the long times required for each data point collected in the interferogram.

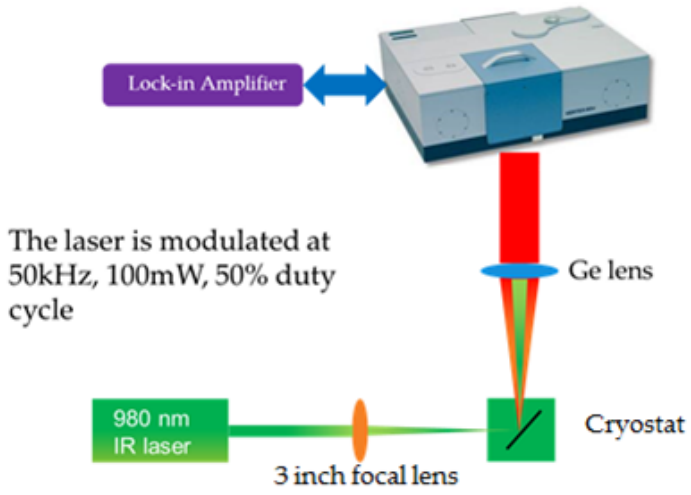

Figure 2.3: Mid-IR PL setup.

Mid-IR photoluminescence (PL) is collected with a Bruker V80v FTIR system. The schematic of the PL setup is shown in figure 2.3. The FTIR

for these experiments is operated in amplitude modulation step scan mode. The 980 nm laser is modulated at 50 kHz with 50% duty cycle. The sample is mounted in a liquid nitrogen cooled cryostat, allowing the measurement temperature to be as low as 77 K. The laser light is focused by a 3 inch focal lens into the cryostat on the sample and the sample emission is collected by a 3 inch Ge lens, which can filter out the laser light at the same time. Then the sample emission is fed into the FTIR and detected by a MCT detector, as described above.

2.3 TRPL Setup

The second mid-IR characterization technique used in this thesis is time-resolved photoluminescence (TRPL), the dominant technique for measuring carrier lifetimes in optoelectronic materials. In a typical TRPL setup, a short time duration laser pulse excites electron hole pairs in the material under test, and the ensuing material's luminescence is measured as a function of time. The slope of the PL vs. time curve gives an instantaneous lifetime and, with appropriate fitting and modeling, can be used to extract valuable information about carrier dynamics in light-emitting materials. More recently, a microwave reflection technique, measuring changes in RF frequency reflection from laser-pulse-excited free carriers, has also been shown to be effective for determining carrier lifetimes, though it does not offer the spectral selectivity of TRPL.

As part of this thesis work, a TRPL system is developed and set up for measuring carrier lifetimes in type-II emitter materials. Figure 2.4 is a schematic drawing of the setup. As shown in figure 2.4, samples were mounted in a cryostat, pumped with a 1064 nm pulsed laser with 1 ns pulse width, 14 μJ peak power and 10 kHz reputation rate. By adding and combining neutral density filters in front of the laser, pumping power can be changed from 14 μJ to 14 nJ. The TRPL emissions from the samples were collected by a parabolic lens, then focused with a Ge lens onto a high-speed liquid nitrogen cooled Kolmar HgCdTe (MCT) detector (KV104-0.25 cut-off, 250 μm x 250 μm) with a 4.375 ns time constant. A 3.6 μm long pass filter was placed in front of the detector in order to block the emission from InAs bandedge (3 μm at 77 K). The signal from the MCT pre-amp is then fed into a LeCroy

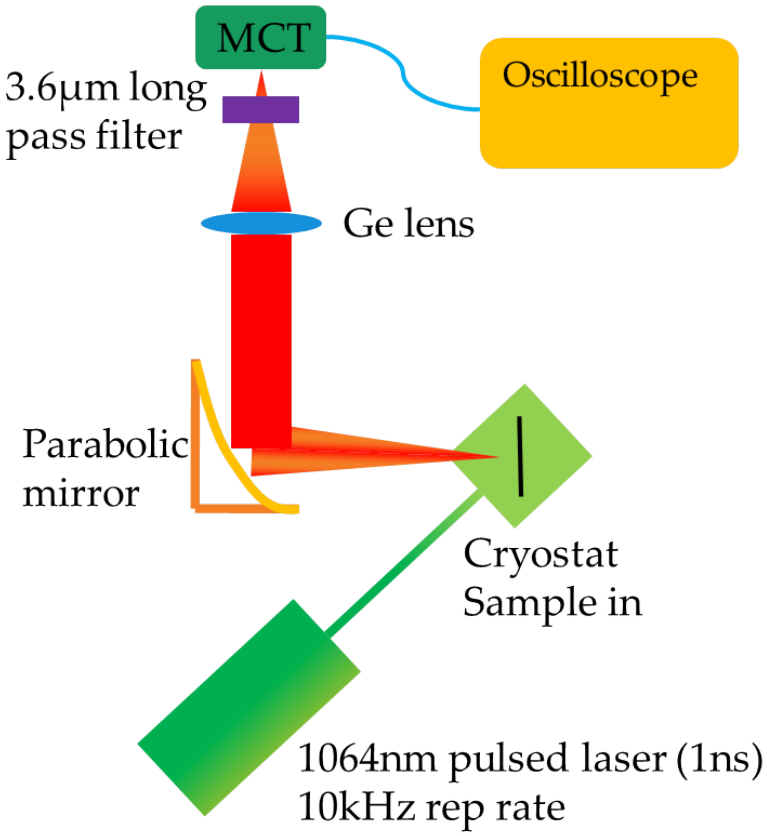

Figure 2.4: TRPL setup in the Wasserman lab.

64Xi-A-N oscilloscope to collect the time-dependence of the emission.

The most general definition of a carrier lifetime is:

$$\tau^{-1} = -\frac{1}{\Delta n}\frac{\delta \Delta n}{\delta t} \tag{2.1}$$

In a semiconductor, we can describe the carrier lifetime as being composed of three different components:

$$\tau^{-1} = \tau_{SRH}^{-1} + \tau_{rad}^{-1} + \tau_{Auger}^{-1} \tag{2.2}$$

where the three terms on the right-hand side of the equation are Shockley-Read-Hall (SRH) lifetime, radiative recombination lifetime and Auger recombination lifetime. Often, we model the above expression using the so-called A, B and C coefficients. This equation can be further expanded as:

$$\tau^{-1} = \frac{n_0 + \Delta n}{\tau_{p0}(n_0 + \Delta n) + \tau_{n0}\Delta n} + B(n_0 + \Delta n) + C(n_0 + \Delta n)^2 \tag{2.3}$$

where the first term in equation 2.3 comes from Shockley-Read-Hall (SRH) recombination, with SRH majority carrier lifetime τ_{n0} and τ_{p0}, the second term represents the radiative recombination (with radiative recombination coefficient B), and the third term is the contribution from Auger recombination (with Auger recombination coefficient C). Here, Δn is the excess carrier concentration, generated via optical pumping, and n_0 is the equilibrium electron concentration (InAs is lightly n-type unintentionally doped by nature). The above expression for carrier decay takes into account the concentration-dependent recombination rate, meaning that the carrier lifetime is a dynamic value and changes with the excess carrier concentration.

Figure 2.5 shows the power-dependent TRPL raw data from a sample with 3 layers of 1 ML InSb grown in InAs matrix separated by 10 nm InAs spacer. According to equation 2.3, the τ^{-1} is proportional to C multiplied by δn^2, B multiplied by δn and SRH recombination rate (A). So at very high injection level (Δn is much larger than n_0), Auger and radiative recombination dominate (to the left of the kink shown in the figure). At low excess carrier density, where the excess carrier density is less than the intrinsic carrier density (to the right of the kink line in the figure), SRH recombination dominates. Since the SRH recombination rate (equation 5.1) is a constant when excess carrier Δn becomes smaller than the intrinsic carrier density n_0, the slope is constant after the kink for the same sample at different initial pumping powers.

Once we get the raw TRPL data with different pumping powers, we start the curve fitting in order to extract the A, B and C values. Since we control the pumping power by adding different neutral density (ND) filters, at each pumping power, the initial excitation carrier number is scaled down from the excitation carrier number when adding the weakest ND filter (ND 1.0). The estimation equation of the initial excess carrier density is shown in equation 2.4.

$$\Delta n_{initial} = F * L(1-\alpha)\frac{E_{laserPeak}}{E_{photon}A_{beam}} \tag{2.4}$$

where L is the distance the laser light, must travel in the semiconductor before it reaches the active region, and α is the absorption coefficient of the cap material the laser beam must penetrate (InAs in our case). $E_{laserPeak}$ is the laser peak energy and E_{photon} is the energy of a single photon from the laser light. A_{beam} is the size of the laser beam area. F is a control factor used to estimate the fraction of the laser light that gets into the material (part

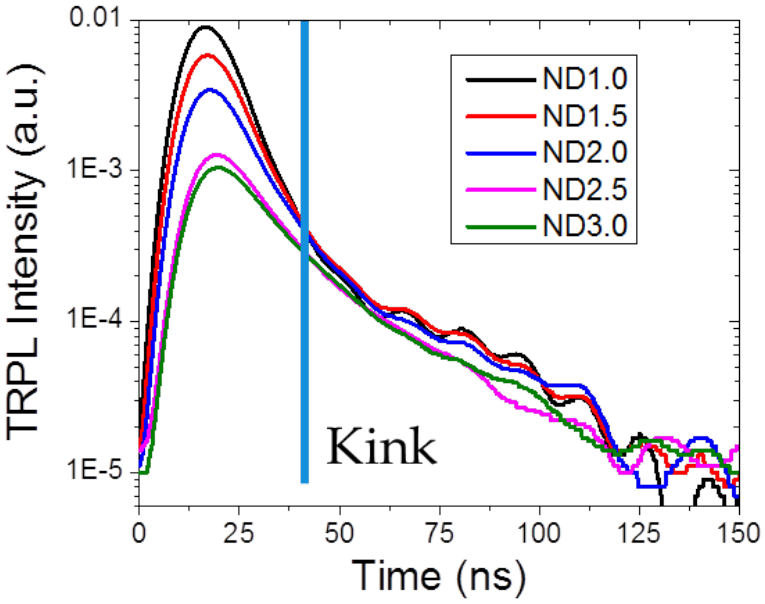

Figure 2.5: Power-dependent TRPL of a sample with 3 layers of 1 ML InSb grown in InAs matrix separated by 10 nm InAs spacer.

of the light will be reflected away) and the fraction of the photon absorbed that can actually excite an electron-hole pair.

We write a program to sweep τ_{n0}, tau_{p0}, n_0, B and C values at the same time and we can plot a carrier density decay as a function of time.

The measurement system has some RC time constant (for example, the RC time constant for our fast MCT detector is about 4.25 ns), which needs to be considered in our lifetime fitting process. Thus, after fitting the TRPL data using the above equations, we dump the result into a differential equation with an RC time constant as a system delay, which is:

$$\frac{dI_{output}}{dt} = -\frac{1}{RC} I_{output} + I_{input} \tag{2.5}$$

where the I_{input} is the data generated by sweeping the five parameters described above. We compare the normalized output with the normalized raw TRPL data, calculate the error value and record all of the parameters used in the process in a six-dimensional matrix (five parameters and the error of that certain combination). Then we find the one set of parameters used in the fitting process with the smallest error value and assume this set of parameters

is the closest to those in the material system. Figure 2.6 demonstrates the results of this process, showing the experimental and fitted TRPL data for a sample consisting of 1.25 ML InSb separated by 10 nm InAs, for varying pump laser power. From the figure we can say that the fitting process can match with the raw data within reasonable error tolerance.

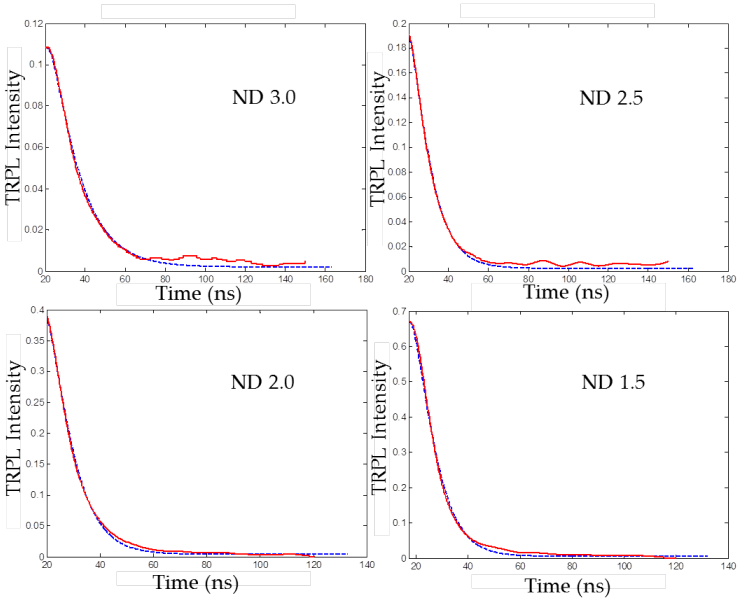

Figure 2.6: A demonstration of fitted TRPL data using the procedure explained previously, compared with raw data under four different laser input power (by adding different ND filters).

Once we find the parameters giving us the best fitting, we can get the A, B and C values of the material.

2.4 AFM

In addition to the optical characterization techniques described above, we use a number of material characterization techniques. Principal among these is atomic force microscope (AFM), used to study the surface structure of our samples in chapters 5 and 6. AFM is one type of scanning probe microscope. It gathers information by tapping the surface of the material using a tip. By tracking the movement of the tip when scanning a sample surface, it can map out the features on the surface. The resolution of the AFM system we used is 0.5 nm.

Figure 2.7 gives an example of an AFM image taken from our AFM system with 2 μm by 2 μm square mesas on the surface.

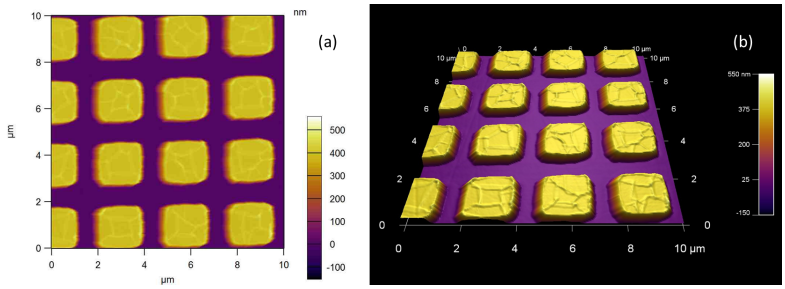

Figure 2.7: A demonstration of AFM taken from a sample with 2 μm by 2 μm square features: (a) plane view and (b) 3D view.

CHAPTER 3

NANOSPHERE LITHOGRAPHICALLY DEFINED QUANTUM DOTS

Quantum dots have been fabricated using a wide range of materials, such as InAs [37], silicon [38], germanium [39] and CdS [40] to name only a few. In addition, numerous techniques have been demonstrated for the formation, fabrication, or growth of QDs, including colloidal chemistry [41], top-down lithographically defined QDs [42] and bottom-up grown QDs [43]. Of those, self-assembled quantum dots [44] (SAQDs) grown by molecular beam epitaxy (MBE) or metal-organic chemical vapor deposition (MOCVD), formed in strongly lattice-mismatched systems where 3D islands form to reduce the mismatch strain, have many favorable properties for device applications such as lasers and photodetectors [45], [46]. Since SAQDs have reasonably high uniformity and can be integrated into semiconductor optoelectronics, significant effort has been made to research and develop SAQDs-based optoelectronic devices for a variety of applications. However, it is difficult to attain accurate control of the uniformity, as well as the size and shape, of SAQDs, which results in inhomogeneous broadening of the electron and hole energies, and thus the optical properties of the QD ensemble. This difficulty has motivated research endeavors in the comparatively accessible alternative dot-fabrication method, nanolithographically defined (NLD) QDs [47]. Nanolithography techniques, such as electron-beam, x-ray, ion-beam and nano-imprint lithography, allow QDs to be grown on selected nucleation sites (bottom up) [48] or fabricated by patterning of quantum wells (top down) [49]. Figure 3.1 shows a schematic of QD formed by bottom-up and top-down methods, using a patterning process. However, the leading-edge lithographic techniques essential for nanoscale confinement in NLD QDs suffer some particular disadvantages, especially in terms of the equipment cost and patterning time to achieve high-resolution, large-area NL. The cost and time associated with large-area QD lithography have motivated the development of nanosphere lithography (NSL) as a prospective substitute for the

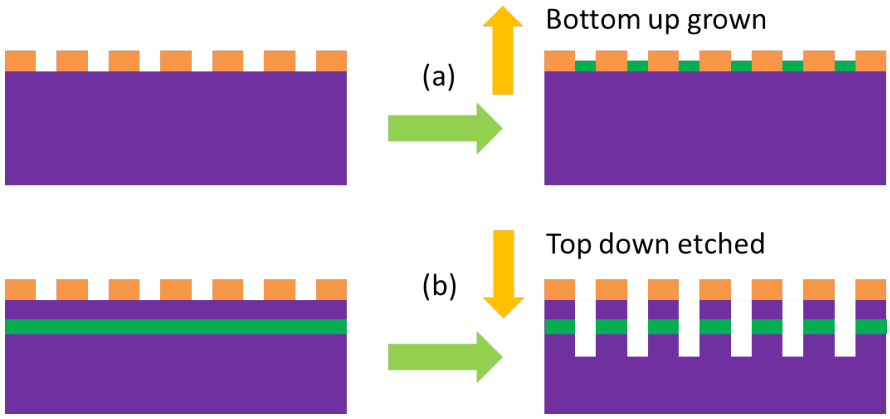

Figure 3.1: QD formed by a patterning process: (a) QD grown on selected sites and (b) QD fabricated by patterning of QWs.

above NL techniques [50]. In NSL, highly uniform polystyrene nanospheres are self-assembled in a tightly-packed poly-crystalline array upon a planar surface. This poly-crystalline array can then serve as an etching (or deposition) mask for patterning of the underlying surface. The primary advantages of the NSL process are its comparative cost- and time-efficiency for achieving large-area nano-patterning of semiconductor surfaces. Past literature has documented top-down NSL for QD fabrication using first-growth InGaAs QWs, with photoluminescence (PL) studies illustrating both a lateral quantization of states in the patterned QW and a narrowing of the PL linewidth, corresponding with the transfer of the nanosphere (NS) array uniformity to the fabricated QDs. The ability to control the energy states in semiconductor QDs gives us the opportunity to design high-quality lasers with photon energies above the semiconductor bandgap. This chapter describes our approach to fabricate QDs using nanosphere lithography and the characterization of the QDs. By controlling the size of the NS, we are able to control the size of the QDs as well as the ground state energy in the QDs. In the end, an emitter device with fabricated QD layers embedded in a p-n junction diode through overgrowth in MBE is fabricated and studied.

3.1 Nanosphere Deposition

For spin-coating, the NS deposition is limited by the size of NS. Usually only large NS can be deposited as the monolayer on semiconductor samples. For small NS, for example, 200 nm and 100 nm NS, nanosphere deposition requires a more complicated spin process, which is not efficient. Efforts have been made to develop techniques for the deposition of small NS on different sample surfaces, and a new method, called dip-coating, has been developed by Weiss' group [51]. The dip-coating method is shown in figure 3.2. First, a certain amount (0.1 mmol/l) of sodium dodecyl sulfate (SDS) is added into DI water to increase surface tension, which enables the NS to form a monolayer on the water surface. Then, polystyrene (PS) NSs (Bang Laboratories, Inc.) are slowly dropped along the surface of a glass slide, such that the ML slides onto the water surface, forming a single layer. Once the monolayer is formed, one can gently slide the substrate into the water and then pull it out of the water, and the substrate becomes coated with the NS. It is important to note that following removal from the water, the sample must be allowed to dry naturally. One cannot blow the sample dry with a nitrogen gun, lest the water and NS are blown off of the sample surface.

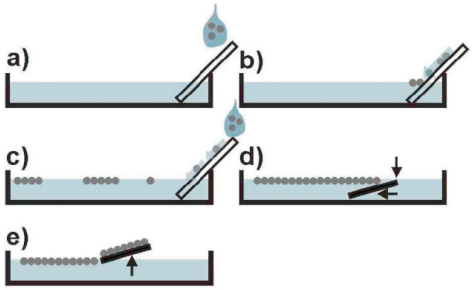

Figure 3.2: Dip-coating method process: (a) Dropping NS solution into water through a glass slide. (b) Wait until all the NS solution slide into water. (c) Adding more NS solution into water until a large area of single-layer NS forms on the water surface. (d) Carefully slide the sample into water and under the already formed monolayer of NS. (e) Slowly pull the sample out of water with the NS on top and then leave the sample at an angle until it is dry [51].

There are some important parameters which have significant effects on the NS dip-coating deposition process, such as the surface property of the semiconductor material, the concentration of NS solution, and the surface

tension of the water solution. In order to form uniform monolayer NSs, the sample surface needs to be flat and smooth. However, as mentioned earlier, the big advantage of the dip-coating method is that the surface does not need to be hydrophilic, unlike the spin-coating method. Also, the concentration of NS solution is important because if it is too low, it can be hard to form a large area of uniformly well-ordered monolayer; yet, if it is too high, one can get multilayer NS formation on the sample surface. The NS solution used here is 8% by weight, which is perfect for NS deposition. In addition, the surface tension of the water is another critical factor. According to the literature, pure DI water does not have high enough surface tension to pack polystyrene NS closely together (as shown in figure 3.3 (a)), so SDS is used to increase the surface tension. According to Vogel's result [51], 0.1 mmol/l is the best SDS concentration for single NS layer deposition (as shown in figure 3.3 (b)). Further increasing the SDS concentration can cause multilayer NS deposition to occur; as shown in figure 3.3 (c), the second layer starts to form at 0.5 mmol/l. Once the SDS concentration goes too high (figure 3.3 (d)), the surface tension is too high, which prevents the formation of a completed layer of NS, so small patches of either multilayer or NSs form randomly on the water surface.

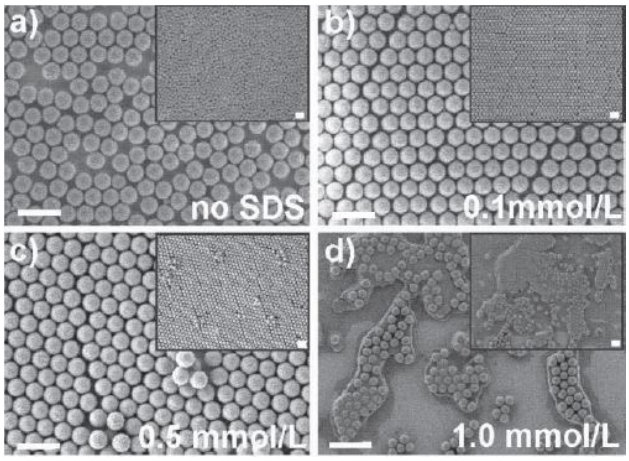

Figure 3.3: The effect of SDS concentration on the quality of NS single layer. (a) No SDS, not closely packed single layer. (b) 0.1 mmol/l SDS, uniformly formed monolayer. (c) 0.5 mmol/l SDS, starting to form a second layer. (d) 1.0 mmol/l SDS, small patches of both multilayer and monolayer occurs [51].

In order to use nanosphere (NS) as an etching mask, a single monolayer

of uniformly distributed NS needs to be deposited on top of the semiconductor substrate. Usually, the NS monolayer is deposited by the spin-coating method, for which the deposition quality is mainly affected by sample surface (hydrophilic or not), the spin speed and the size of the NS. The sample surface needs to be highly hydrophilic, otherwise the NS will not coat the surface in a uniform manner. Figure 3.4 shows a hydrophilic GaAs sample with 500 nm diameter NS spin-coated onto the surface. Figure 3.5 shows the NS coating following spin deposition for a hydrophobic surface. As can be seen, the surface in figure 3.5 only has NS on a small portion of the surface while the sample with a hydrophilic surface has a well-ordered monolayer of NS on top. In order to make the surface hydrophilic, the samples need to be treated in oxygen plasma for 1-2 min.

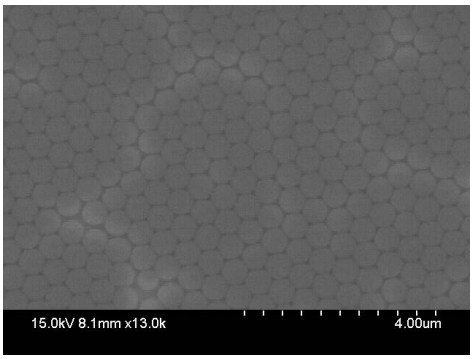

Figure 3.4: 500 nm diameter NS spin-coated on the hydrophilic GaAs sample surface.

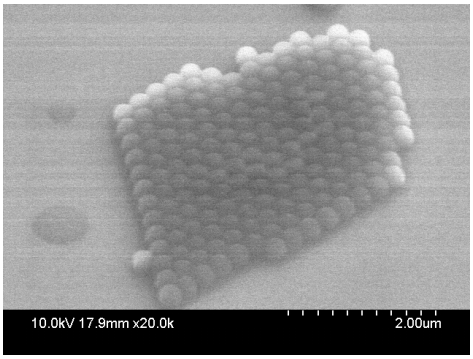

Figure 3.5: 300 nm diameter NS spin-coated on the GaAs substrate.

3.2 Fabrication

3.2.1 Overview

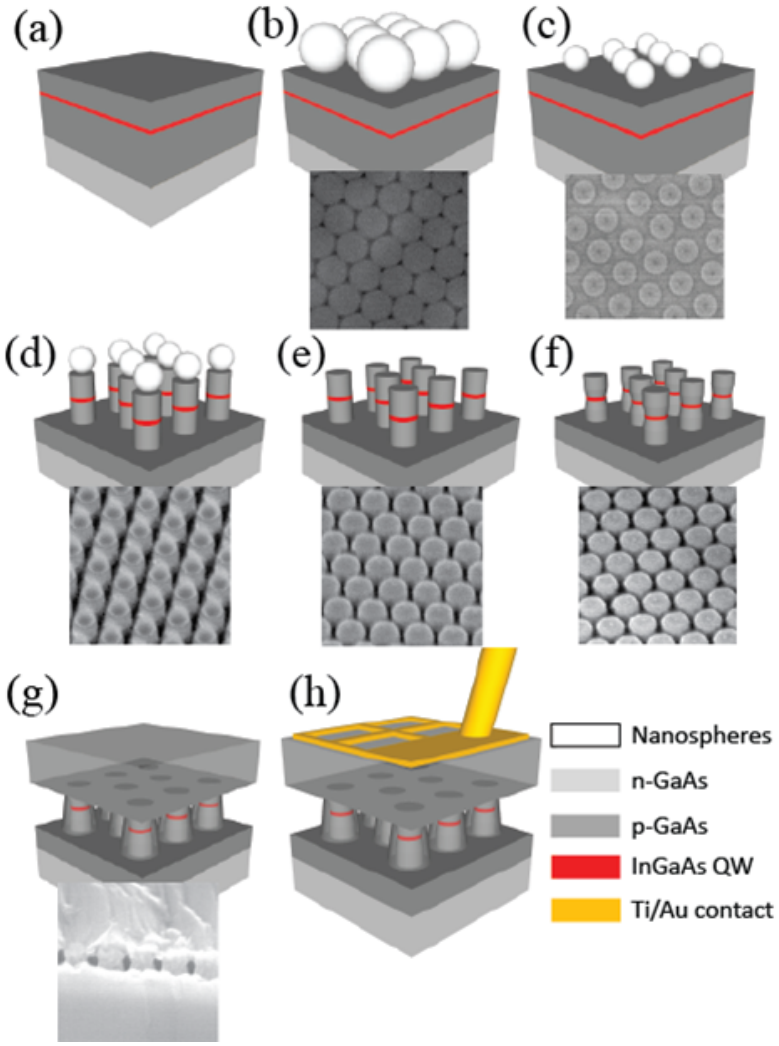

Figure 3.6: Schematics and scanning electron micrographs of the process flow for fabrication of nanolithographically patterned quantum dot emitters. (a) First growth sample, nanosphere (b) deposition and (c) resizing, (d) RIE through the quantum well structure, (e) nanosphere removal, (f) selective wet etch of the InGaAs quantum well, (g) mass reflow (anneal) and p-GaAs overgrowth of the patterned pillars, and finally, (h) contact deposition and wire bonding. All SEM images are 1 μm across in scale.

Figure 3.6 is a pictorial representation of the fabrication process along with SEM images associated with each step of the process to make an emitter

with buried NSL defined QDs. Our devices begin with the MBE growth of InGaAs QWs in a GaAs matrix. Using NSL, the as-grown QW sample was then fabricated into nanopillars. First, five QW samples (figure 3.6(a)) were coated with an ordered and close-packed monolayer of 200 nm diameter PS nanospheres (figure 3.6(b)). Then the NSs were resized to diameters of 90, 140, 150, 160, and 180 nm using an O_2 plasma reactive ion etching (RIE) process (figure 3.6(c)). Using the resized NSs as an etch mask, samples were then vertically etched into nano-pillars with a height of 110 nm (figure 3.6(d)) by inductively coupled plasma reactive ion etching (ICP-RIE). Then the NSs were entirely removed by O_2 plasma RIE (figure3.6(e)). After the NSL process, the samples were annealed at 640 ^{o}C for 20 minutes in MBE under an arsenic overpressure and overgrown with 500 nm of Be-doped GaAs, which was then capped with 50 nm of highly Be-doped GaAs for the top contact. Instead of filling in the space between the nano-pillars, the overgrown GaAs formed a cap on top, which left air-gaps within the patterned region. More detailed information including all the parameters used in each fabrication step, will be discussed in the following subsections.

3.2.2 Nanosphere Resizing

Once an ordered, closely packed NS monolayer is deposited upon the surface, the NS diameter must be decreased for two primary reasons. First, with touching nanospheres, there is little space to etch down through the semiconductor to form individual QDs. Second, the large NS diameters will not provide substantial lateral quantization; thus, resizing the nanospheres will allow us to observe size quantization effects. A master-slave reactive ion etch (RIE) is used to resize the nanosphere. The recipe used here is:

- O_2 = 10 sccm
- Power = 100 W
- Chamber Pressure = 150 mTor

By controlling the time used to etch the NS, the size can be controlled accurately. Taking 200 nm diameter NS as an example, figure 3.7 shows the resized nanosphere diameter as a function of dry etching time, from which it

can be seen that the etching rate is slightly nonlinear because as the diameter gets smaller, less material needs to be etched to further shrink the size.

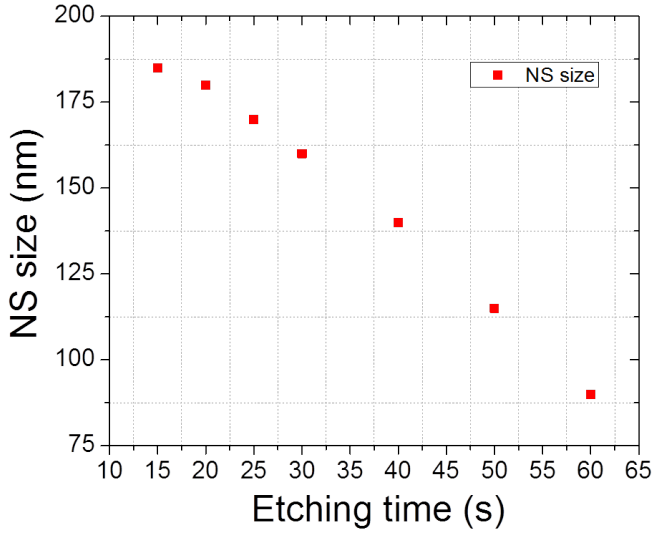

Figure 3.7: Resized NS diameter as a function of dry etching time.

Figure 3.8 shows the NS diameter resized from 200 nm to about 145 nm diameter (the etching time is 40 s). The figure shows that the reduced NS size has good uniformity with variation in QD size less than 5%.

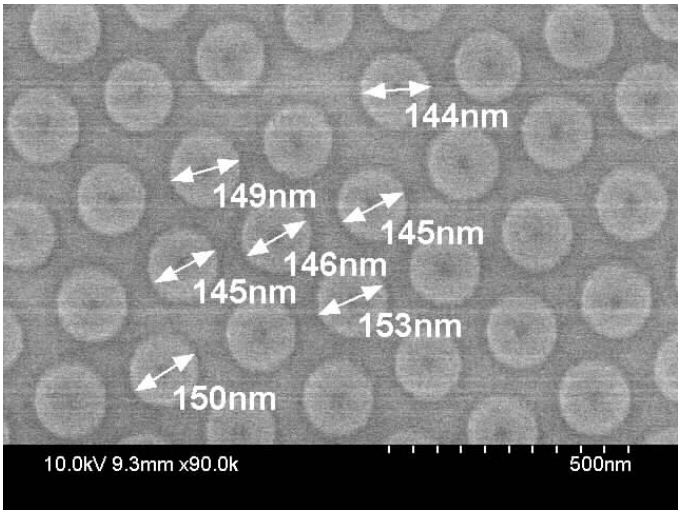

Figure 3.8: Resized NS from 200 nm to 145 nm diameter with a variation less than 5%.

3.2.3 Nanopillar Etching

After resizing the NS to an appropriate diameter, the resized NS are used as a dry etching mask for the nanopillar etch. In order to have high-quality nanopillars, inductively coupled plasma (ICP) RIE is used for nanopillar fabrication. Dry etching is a physical and chemical process, meaning that a relatively nonreactive atom (usually Ar) is needed to physically bombard the atoms out of the semiconductor material and then a reactive molecule or atom is needed to react with the bombarded atom from the material to form a molecule with high volatility which can be easily pumped away from the reaction chamber. The most popular etchant for GaAs/AlGaAs material is a chloride-based molecule such as BCl_3 or $SiCl_4$ since both the $GaCl_3$ and $AlCl_3$ formed in the process have a relatively low boiling point (201 °C for $GaCl_3$ and 120 °C for $AlCl_3$), meaning that they can be easily pumped away from the high vacuum chamber. But for indium, a chloride-based etchant is no longer suitable, given that the boiling point of $InCl_3$ is 800 °C, making it exceedingly difficult to achieve gas phase, which prevents pumping and removal of the $InCl_3$. So $InCl_3$ will just redeposit on the surface of the sample and prevent further etching. In order to etch through the InGaAs quantum well layer, a bromide-based etchant must be used. The boiling point of $InBr_3$ is 420 °C, which is almost half of that of $InCl_3$. The etchant used here is a combination of Ar and HBr:

- Ar = 2 sccm
- HBr = 10 sccm
- RF1 = 65 W
- RF2 = 90 W

The Ar to HBr ratio is very important; if it is too high, then the physical bombardment is faster than the chemical reaction so that the extra In atoms which cannot be turned into $InBr_3$ can redeposit on the sample surface to prevent further etching. If it is too low, the HBr molecule can also physically attack the sample surface and make the sample surface very rough. So a balance between the physical and chemical reactions is necessary for reasonable etching quality. The RF1 power determines the power of the inductor, which

is the key factor determining the plasma density. The higher the plasma density, the faster the resulting etching rate. This is the advantage of ICP-RIE over traditional RIE. The plasma density can be tuned separately by controlling RF1 power. The RF2 power controls the voltage added between the capacitor plates, which also determines the etching rate. RF2 = 90 W gives a voltage added on the capacitor of about 250 V. Figure 3.9 shows the SEM of a nanopillar etched by HBr and Ar; as can be seen from the SEM, well-ordered nanopillars have been formed on the surface of the sample.

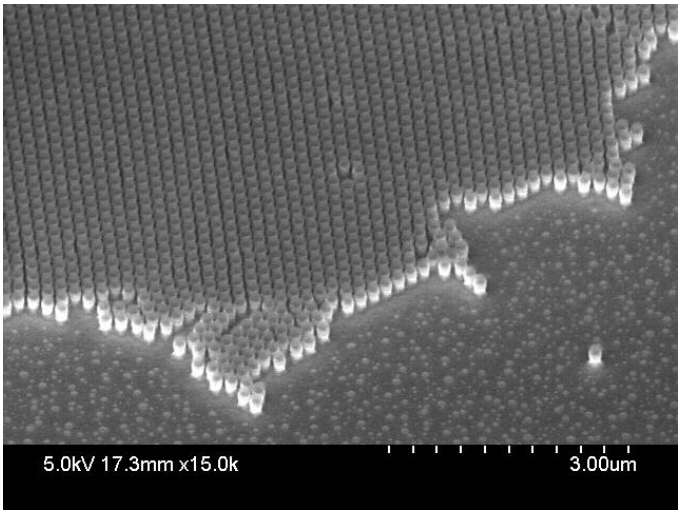

Figure 3.9: The edge of the large-area etched nanopillar array (160 nm diameter).

After the pillars are etched, one has essentially formed quantum dots in the nanopillars. In these structures, the lateral confinement is provided by the nanopillar walls, and the vertical confinement comes from the original quantum well. The next step is to remove the NS left on top of the nanopillars. The same O_2 RIE was used to remove the NS as to resize the NS. At least 2 min are necessary to completely remove the polystyrene residue on top of the nanopillar. This step is critical because if the polystyrene is not completely removed, the subsequent overgrowth can suffer. An SEM of the nanopillar array after the NS removal is shown in Figure 3.10. Now an array of well-ordered nanopillars, each containing an InGaAs quantum well, is left on the sample surface. Following the NS removal, an InGaAs selective etch is used to further resize the quantum dot diameter. The selective etching recipe is citric acid: H_2O_2 = 2:1. An SEM of nanopillars after selective etching is shown in figure 3.11.

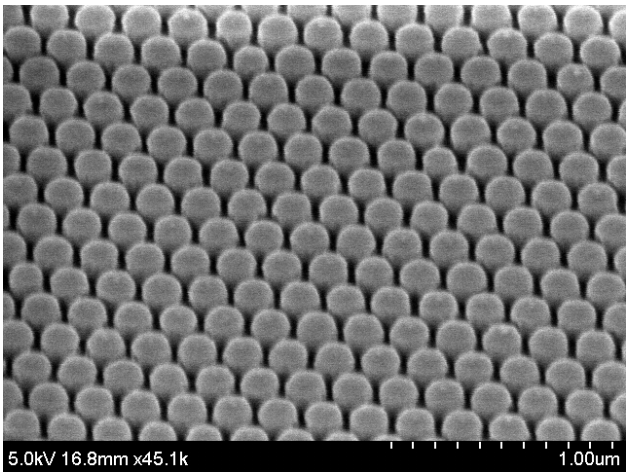

Figure 3.10: SEM of the nanopillar after removal of the polystyrene etching mask.

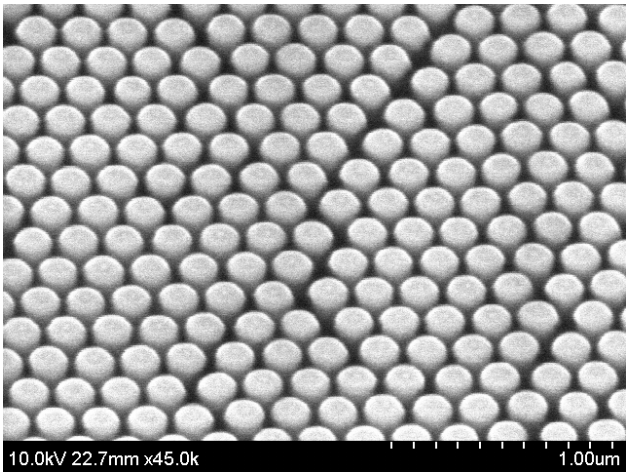

Figure 3.11: SEM of the nanopillar after selective etching to further resize the quantum dots.

3.2.4 Emitter Fabrication

At this point, QDs have already formed, and ideally, quantization should be visible in the PL test. However, the dry etching induced damage makes the PL signal very weak to observe. Further, in order to make devices, contact must be made so that current can be run through the QDs. Thus, the etched quantum dot samples are sent back to overgrow after the removal of the residual nanosphere material. The samples are returned to the MBE chamber and annealed for 20 min at 640 °C. The samples experience a mass reflow process during which GaAs can encapsulate the InGaAs quantum dots, resulting in an improvement of optical properties [52]. Following the annealing process,

a layer of 500 nm beryllium-doped (Be-doped) GaAs ($N_A = 5 \times 10^{17}$ cm^{-3}) is overgrown and a 50 nm of highly Be-doped GaAs ($N_A = 1 \times 10^{19}$ cm^{-3}) is capped on the very top of the samples to allow for an ohmic p-type contact. The overgrown material does not fill the gap between nanopillars, (as shown in figure 3.12), which can be explained by the fast overgrowth rate. The overgrown material deposits on both the top of nanopillars and the sample surface, but it starts to connect and form a complete layer before the gaps are filled. After overgrowth, samples are tested by PL and then fabricated into emitters. Figure 3.13 shows the process flow chart (top) and the final device (bottom). Standard photo-lithography is used to pattern mesas (1350 um $\times$ 2050 um) and wet etching is used to define the mesas which are etched through the two epilayers to the GaAs below the InGaAs QW/QD layer. After the mesa etch, another photo-lithography is applied to define the top contact pattern. Then a Cooke e-beam evaporator is used to deposit Ti/Au (20 nm/200 nm) contact on the sample surface. Following lift-off, the samples' current-voltage (IV) curve is measured and the devices with the best IVs (those which look the most like diodes) are wire-bonded to gold pads. A metal grid with 70 μm $\times$ 70 μm openings is designed so that the surface emission is allowed from the underlying diode.

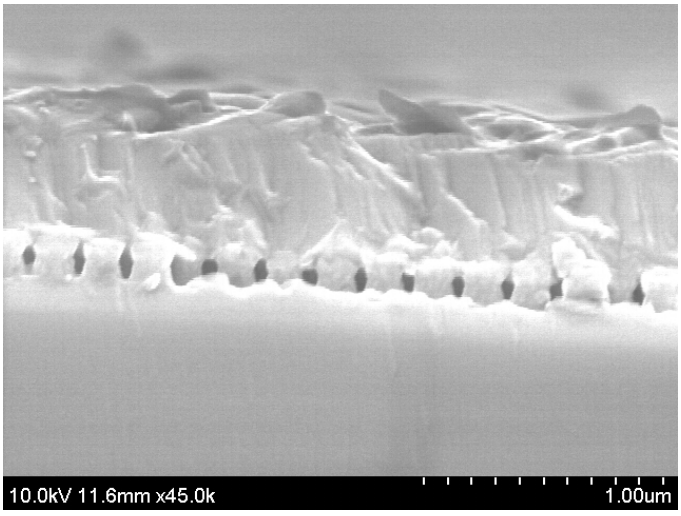

Figure 3.12: Cross-section SEM of 150 nm QDs sample. The overgrown material is on top of the nanopillars.

Once the device is fabricated, EL emission is tested at both 77 K and 300 K, which will be discussed in next section.

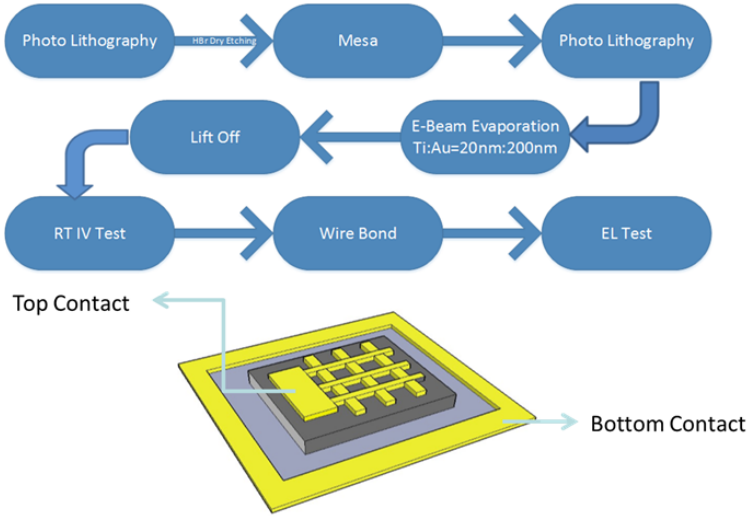

Figure 3.13: Process flow chart of the emitter fabrication.

3.3 Photoluminescence

PL from the five fabricated samples with different pillar size after annealing and overgrowth is shown in figure 3.14. The figure shows clear PL blue-shifts, with the blue shift energy increasing with decreasing pillar size. The observed size dependence of the PL peak can be explained by the increase in lateral confinement of the nanopillars with a smaller diameter. For the smallest diameter pillars fabricated (90 nm), a peak blue-shift of 37 meV is observed, indicating a significant lateral confinement in the QDs. The PL data for both before and after annealing of the 160 nm diameter pillars (at 77 K) is shown in figure 3.15. Due to extensive damage induced by dry etching, no PL signal from the nanopillars is seen before the annealing and overgrowth. However, following annealing and overgrowth, the optical properties of the QD array are significantly improved, and a clear PL peak is observed from the nanopillar array.

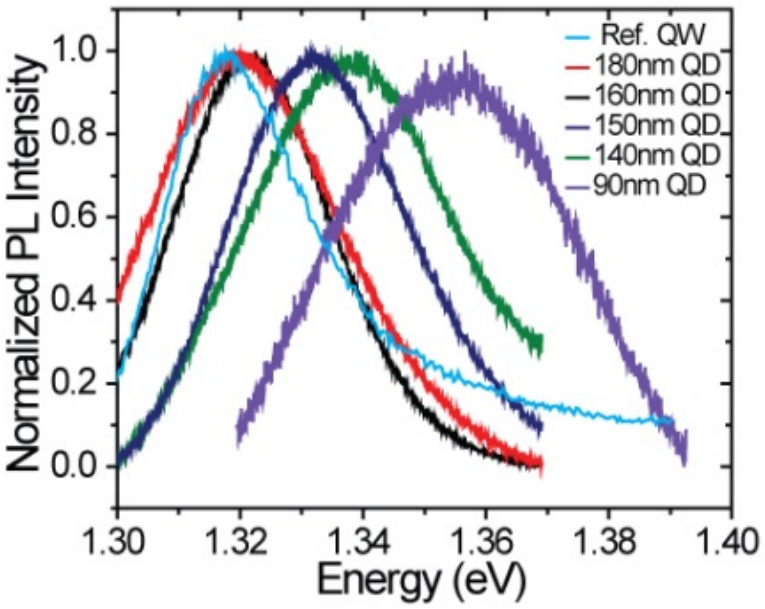

Figure 3.14: PL from etched nanopillar structures of varying diameter taken following anneal and overgrowth process. All spectra are taken at 77 K.

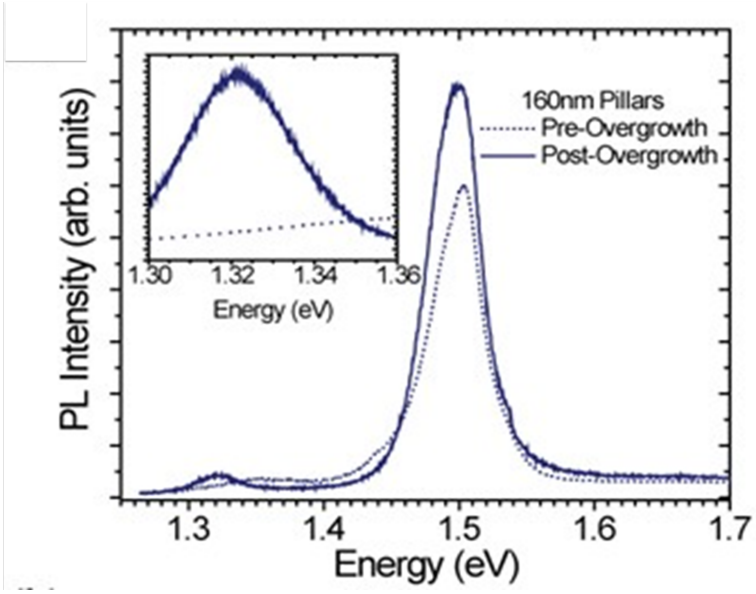

Figure 3.15: PL emission from 160 nm diameter nanopillars before (dot) and after overgrowth (line). The inset shows a higher resolution of QDs emission (1.32 eV at 77 K).

3.4 IV-Test

After overgrowth, the samples are made into emitters, and then the electrical properties of each diode are tested. Current density-voltage (JV) data taken

from the diode emitter fabricated from 90 nm diameter QDs are shown in figure 3.16. As can be seen from the J-V test, the pn junction quality is reasonably good at both 77 K and 300 K. At 77 K, the turn-on voltage is about 1.8 V and at 300 K, the turn-on voltage is about 1.5 V.

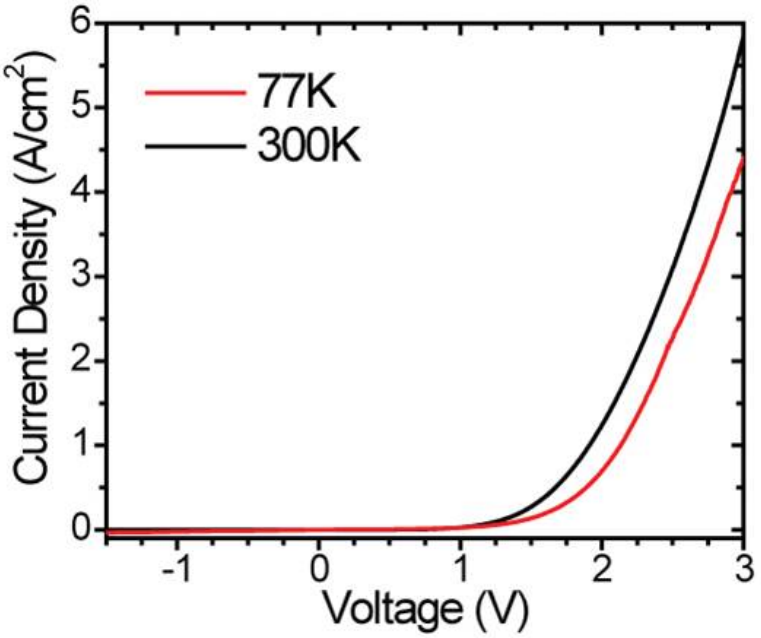

Figure 3.16: Current density-voltage (J-V) test at both 77 K and 300 K for an emitter device fabricated from 90 nm diameter quantum dots.

3.5 Electroluminescence

Temperature-dependent EL data taken of the 90 nm diameter nanopillar diode is shown in figure 3.17 for a current of 12 mA. The EL spectrum at 77 K shows a remarkably narrow QD peak with a full-width-half-maximum (FWHM) of 18 meV, which suggests a better uniformity of dots than standard self-assembled InAs quantum dots [53]. As expected, the emission energy red-shifts and the peak intensity decreases as the temperature increases. In order to further increase the emission intensity, a sample containing three GaAs/InGaAs quantum wells is grown and fabricated into an emitter with the same process. Figure 3.18 shows the temperature-dependent EL of a diode emitter made from a 150 nm diameter nanopillar, from which an enhancement of EL intensity can be observed. However, the FWHM of this

three-dot emitter is greater than that of the single quantum dot sample. This is probably caused by the thickness variation of these three quantum wells during the growth.

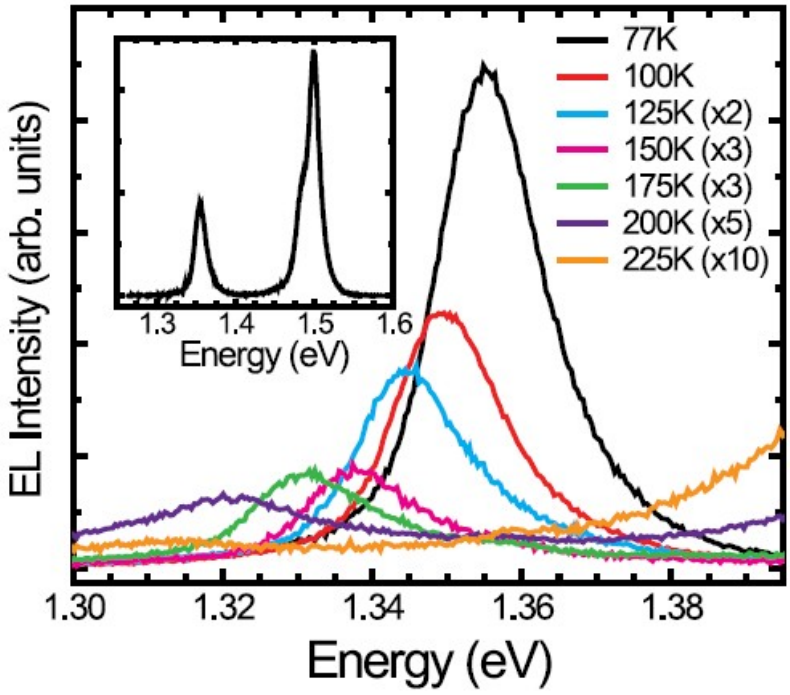

Figure 3.17: EL spectra from the 90 nm QD diode (I = 12 mA) as a function of temperature, showing narrow linewidth quantum dot electroluminescence up to 200 K. The inset shows an expanded view of the EL spectra for the device at 77 K.

3.6 Limitation of NSL-Defined QD

From the narrow linewidth of the NSL-defined QDs presented in the previous sections, we can see that the NSL defined QDs have high uniformity, there is one limitation of the NSL defined QD that makes it hard to use as the active region in a laser structure. This primary challenge is the density of the QD array. As shown in figure 3.19, since the nanospheres are forming a closely packed monolayer on the surface of the sample, the size of the nanosphere directly determines the density of the QD array. Taking a 200 nm diameter nanosphere as an example, the density of the fabricated QD can only be $2.5 * 10^9$ cm^{-2}. In order to have enough gain material in the active region of a QD

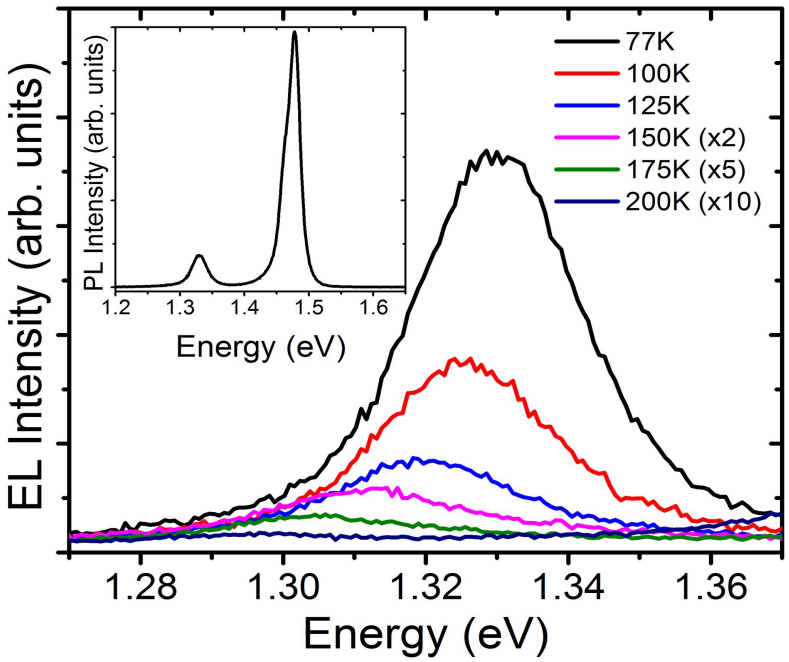

Figure 3.18: EL spectra from a 150 nm QD diode as a function of temperature. This sample is made starting with a 3-QW sample, which shows an enhanced emission intensity.

laser structure, QD densities on the order of 10^{10} cm^{-2} are usually required, according to the literature on SAQD laser emitters [54],[55],[56]. With this in mind, we tried using 100 nm diameter nanospheres, which can give us a QD density of $1 * 10^{10}$ cm^{-2}, but the uniformity of the commercially available 100 nm diameter nanospheres is much worse than that of the larger ones. The density of the NSL-fabricated QDs provides the primary challenge to the further development of these nanostructures for optoelectronic applications. Nonetheless, with the development of improved uniformity in small diameter NSs, it is conceivable that the approaches demonstrated here may provide a path towards further emitter and laser development.

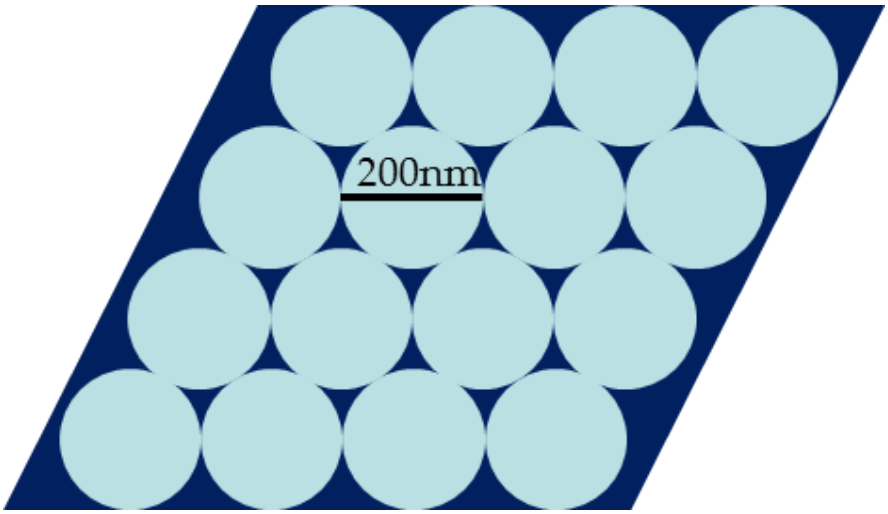

Figure 3.19: Closely formed monolayer of NSL defined QD. The density of the QD is determined by the size of the nano-sphere used.

CHAPTER 4

SUBMONOLAYER QUANTUM DOTS

In this chapter, we demonstrate control of energy states in epitaxially-grown quantum dot structures formed by stacked submonolayer InAs depositions via engineering of the internal bandstructure of the dots. Transmission electron microscopy of the stacked sub-monolayer regions shows compositional inhomogeneity, indicative of the presence of quantum dots. The quantum dot ground state is manipulated not only by the number of deposited InAs layers, but also by control of the thickness and material composition of the spacing layers between submonolayer InAs depositions. In this manner, we demonstrate the ability to shift the quantum dot ground state energy at 77 K from 1.38 eV to 1.88 eV. The results presented offer a potential avenue towards enhanced control of dot energies for a variety of optoelectronic applications.

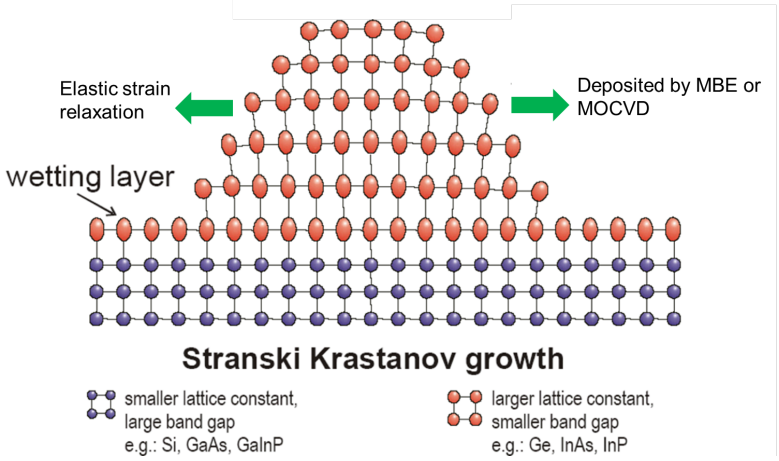

Figure 4.1: Growth mechanics of SK grown quantum dots [57].

4.1 Growth Method of InAs SML QD

As mentioned previously, the NSL method offers the ability to control QD size with good uniformity, though at the expense of QD density, which is not ideal for laser active region material. Self-assembled quantum dots (SAQDs) can offer high density QD layers of high optical quality, but with limited control over dot size and geometry, compared with NSL defined QDs. Typically, SAQDs are grown by molecular beam epitaxy (MBE) or metal-organic chemical vapor deposition (MOCVD). Such SAQDs are most often grown using the Stranski-Krastanow (SK) growth method, where strongly lattice-mismatched semiconductor layers are grown compressively strained on a higher energy bandgap substrate, forming three-dimensional (3D) islands (as shown in figure 4.1). In the SK growth mode, the initial deposition of the compressively strained material forms a wetting layer, a thin (1ML) layer of compressively strained, lower band-gap material [58]. As growth continues, the increasing strain resulting from the continued deposition of the smaller lattice constant material is relieved by the formation of pyramidal, or lens-like, clusters of the deposited material. These quantum dots for pseudomorphically (namely without defect formation), giving them excellent electronic and optical properties. These SAQDs have relatively high surface density, strong optical transitions, and can be integrated into many semiconductor optoelectronic device architectures, such as lasers and photodetectors. Many research groups have put significant effort into developing SK grown SAQD based optoelectronic devices [59],[60],[61]. Figure 4.2 is an example of a mid-IR photodetector with a QD in a well (QWELL) structure in the active region made by Krishna's group. The layered structure of the active region is shown in figure 4.2 (a) and the responsivity of the detector is shown in figure 4.2 (b).

However, there are still a few drawbacks to the conventionally grown SAQDs. First, it can be challenging to achieve both high-density and high-uniformity QD layers. According to [62], the majority of SAQD densities are on the order of 10^{10} cm^{-2} and usually have a broad range of ground state energies caused by the inhomogeneous broadening of QD size; for example, the typical FWHM value for SK dots is about 30 meV. QD lasers and detectors with better gain and sensitivity will require higher QD density and uniformity. In addition, SAQDs grown by the SK method require the formation of a thin wetting layer before the 3D QD structure formation (shown in figure

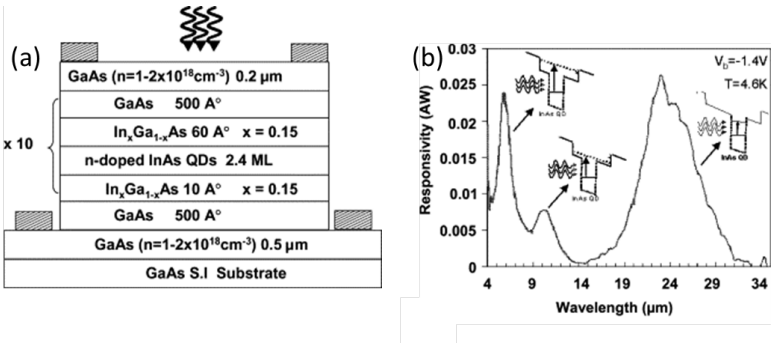

Figure 4.2: (a) The active of the photodetector made of Sk QD. (b)The responsivity of the detector in the mid-IR region.

4.1). This wetting layer acts like a quantum well, which can affect carrier dynamics within the QDs and add complexity to the engineering of QD energy states (already a challenge for SAQDs) [63]. One potential alternative to SK SAQDs is the growth of so-called submonolayer (SML) QD structures [64]. The SML QDs are grown by Volmer-Weber (VW) mode, meaning that the atoms build 3D islands in all directions due to their strong atom-atom interaction [65]. As illustrated in figure 4.3, when depositing less than one layer of material, uniform QDs form (figure 4.3 (a)), and as more material is deposited, non-uniform islands start to grow (figure 4.3(b) for one and two layers and figure 4.3(c) for more than two layers).

Figure 4.3: Schematic of Volker-Weber QD growth. (a) Monolayer islands of material formed with less than a ML of equivalent deposition thickness. (b) Variation in island height for 1-2 ML of equivalent deposition thickness. (c) Continued QD formation with more than 2 ML of equivalent deposition thickness.

These SML QDs traditionally are formed by alternating depositions of SML InAs layers and monolayer (ML) (or thicker) GaAs spacer layers (in our work we refer to an individual InAs layer as SML InAs and the sum of the SML InAs layers and spacers as the SML QD) [66], [58]. Though we describe SML QD growth using InAs as our representative SML layer and GaAs as our representative spacer layer, the use of ternary or quaternary alloys for both SML and spacer layers is also possible. The initial SML

InAs deposition forms puddles of ML thickness InAs, which are then covered by the subsequent overgrowth of a GaAs spacer. Additional depositions of SML InAs, for GaAs spacers below a certain critical thickness, will vertically align the InAs puddles via propagation of strain fields through the spacer layer. SML QDs have been extensively studied and are often cited as a promising QD material system for high-power, high-gain and high-speed semiconductor lasers due to their high density and the absence of the wetting layer [67],[68]. Hybrid structures combining SML QDs with either SK QDs or traditional QWs also offer a means of controlling the polarization and wavelength of the QD gain spectrum [69], or alternatively, the energy of intersubband transitions, by growing increasing numbers of InAs/GaAs layer pairs [70]. However, QD device performance is not solely determined by the position of the QD ground state, and the control of SML QD emission by increasing the number of layer pairs does not allow for decoupled engineering of multiple energy states within the SML QD. Previous work has attempted modification of energy states in QDs via post growth annealing [71], but this approach still couples changes in ground state energies to those of higher energy states in the QD. Ideally, engineering of QD energy states could be achieved in a similar fashion to the complex band-structure engineering utilized in structures such as the quantum cascade laser [72], allowing somewhat independent control of ground and excited states. Modifying the QD growth substrate and cladding material, or the amount of QD material, has long been the primary mechanism of controlling SAQD energies. However, SML QDs offer a new avenue towards control of energy states, which we refer to as internal bandstructure engineering, where the local internal bandstructure of the SML QDs is controlled by choice of the spacer layer composition and thickness on an ML length-scale. In such an approach, the SML QD energy spectrum is primarily determined by engineering the local bandstructure within the SML QD volume, creating the potential to engineer the energies, and ultimately the wavefunctions, of states in the SML QD. Here we present a first step toward this new approach to QD design and growth, demonstrating the control of energy states in SML QDs with identical surrounding material matrices and SML InAs coverage, but with varying internal composition profiles. The work presented here focuses on the interband evidence for our internal bandstructure engineering approach, but conceivably could be extended to intersublevel studies for long wavelength

IR applications.

4.2 Calibration of InAs SML QD

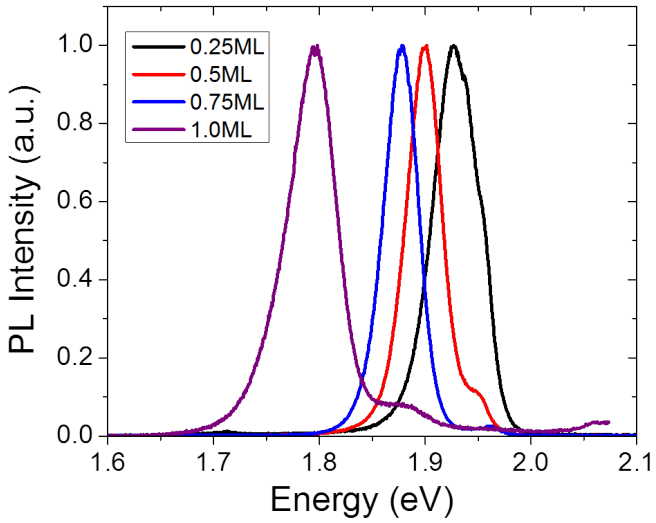

Figure 4.4: 77K PL of four samples with different InAs SML coverage (from left to right: 0.25 ML, 0.5 ML, 0.75 ML and 1.0 ML)

The SML QD samples investigated were grown by MBE in a SVT Associates reactor on semi-insulating (SI) GaAs substrates. Numerous samples were grown to investigate potential mechanisms for energy state engineering in SML QDs. First of all, an undoped GaAs (200 nm) and $Al_{0.35}Ga_{0.65}As$ (50 nm) buffer was grown on top of the substrate. Then, three stacks of the SML QD structures were grown, each sandwiched by 50 nm Si-doped $Al_{0.35}Ga_{0.65}As$ (n-type, ND = $5*10^{16}$ cm^{-3}). In our structure, adjacent SML QD/spacer stack were spaced by 100 nm of n-doped AlGaAs. All samples studied in this work were capped with a 50 nm Si-doped GaAs (n-type, ND = $5*10^{18}cm^{-3}$) to reduce the effect of surface band bending. In all samples, the growth substrate temperature used is 485 ^oC for InAs SML and 545 ^oC for AlGaAs. The As pressure is $4.5*10^{-6}$ Torr for InAs SML and $3.0*10^{-6}$ Torr for AlGaAs in our growth chamber. The growth rate is about 0.056 ML/s for InAs SML deposition and 0.26 nm/s for AlGaAs. After each SML InAs deposition, a 10 s growth interrupt is introduced under an arsenic overpressure.

Samples were prepared for cross-sectional transmission electron microscopy (XTEM) by mechanically polishing to electron transparency followed by low energy ion milling. A combination of conventional bright field (BF) TEM and high-angle annular dark field (HAADF) scanning TEM (STEM) imaging was performed in a Tecnai Osiris operated at 200 kV; energy dispersive x-ray spectroscopy (EDS) maps were also collected in STEM mode. The PL system used to study the sample is the same as that used in chapter 2. In order to do a systematic study on the InAs submonolayer structure, we start with a surface coverage study (0.25, 0.5, 0.75 and 1 ML) in both GaAs and $Al_{0.35}Ga_{0.65}As$ material matrices. Figure 4.4 shows the PL taken on four samples with different SML coverage. For each sample, one layer of the SML InAs is deposited in $Al_{0.35}Ga_{0.65}As$ matrices. The PL peak position red-shifts from 1.926 eV to 1.795 eV as the deposition thickness increases from 0.25 ML to 1.0 ML. This shift is caused by the increasing size of the quantum dots and agrees well with what has been demonstrated in the literature.

Since we are trying to use SML QD in the quantum cascade structure, controlling the energy state becomes the most important thing. In order to study the capability of controlling ground state energy, a second series of growths was then performed to demonstrate SML QD energy tuning by increasing numbers of SML InAs/spacer pairs. This is a well-established technique for controlling ground state energies in SML QDs in the literature [72]. In this study, four samples were grown: SML QD structures with 1, 2, 3 and 8 repetitions of 0.5 ML InAs depositions with 1.5 ML $Al_{0.35}Ga_{0.65}As$ spacer layers. Figure 4.5 shows the normalized PL spectra from these four samples with different InAs/spacer repetitions. The inset is a schematic drawing of the basic sample structure for this growth series.

The results agree with previously published work [72]. As the number of SML InAs depositions increases, the ground state energy of the SML QD structure decreases. However, the capability of controlling ground state energy is limited if the only parameter we can control is the number of InAs/spacer repetitions. As can be seen from the PL, adding a single InAs SML to the two-layer system results in a 50 meV shift of the QD ground state energy, yet adding 5 additional InAs SMLs to the 3-layer QD only shifts the ground state PL an additional 50 meV. By controlling the number of SML InAs layers a shift of 200 meV was achieved, with PL at 1.87 eV for the single InAs SML and 1.66 eV for the 8-layer InAs SML sample. Thus, in order to

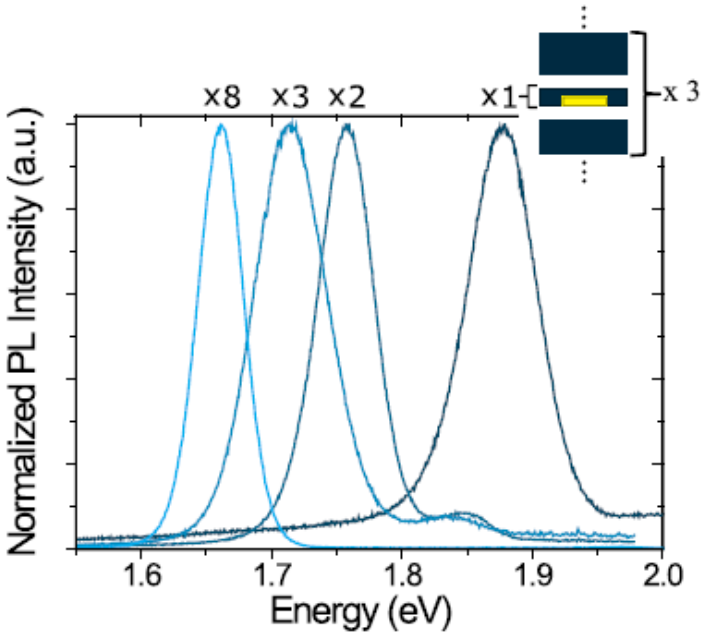

Figure 4.5: Low-temperature PL from SML QD samples with 1, 2, 3 and 8 depositions of InAs SML in the active region.

achieve greater control over energy states in our QDs, SML QD designs with internal band structure engineering were explored.

4.3 Controlling of Ground State Energy by Band Engineering

Five samples, each with three periods of 8 InAs SMLs separated by 100 nm of AlGaAs (as described above, and as shown in figure 4.6) were grown. Instead of changing the number of InAs SMLs, in these samples we control the thickness and material composition of the spacer layers between the InAs SMLs. Figure 3.6 shows schematics of the structures of each of the 5 samples. Sample B (figure 4.6(b)) consists of SML InAs layers with constant thickness 1.5 ML GaAs spacer layers, sample C (figure 4.6(c)) uses constant thickness 1.5 ML $Al_{0.35}Ga_{0.65}As$ spacer layers (this is the same sample as the 8-layer SML QD in figure 4.4), samples D and E (figure 4.6(d,e)) have constant thickness spacers (1.5 ML) with graded Al-content AlGaAs spacers, and sample F (figure 4.6(f)) uses GaAs spacers with decreasing layer thickness. For samples D and E, Al content in the spacer was varied by growing $Al_{0.35}Ga_{0.65}As$/GaAs

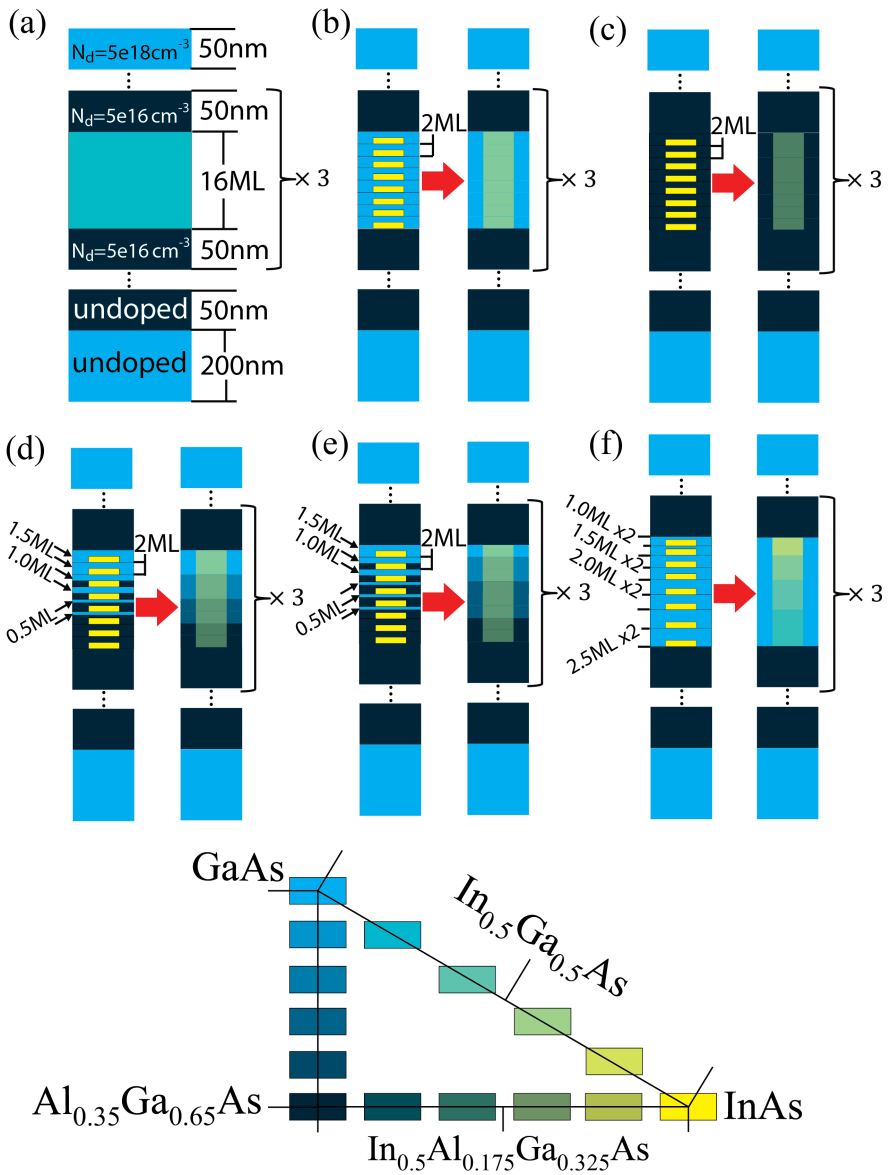

Figure 4.6: Schematic of the sample structures investigated in this work. For each of (b-f), the left schematic shows the idealized structure, while the right schematic assumes some vertical alloying of the SML QD. (a) 16 ML $In_{0.25}Ga_{0.75}As$ QW control sample, (b) 8-layer 0.5 ML InAs/1.5ML GaAs spacer, (c) 8-layer 0.5 ML InAs/1.5 ML $Al_{0.35}Ga_{0.65}As$ spacer, (d, e) 8-layer 0.5 ML InAs/graded Al AlGaAs spacers, and (f) 8-layer 0.5 ML InAs/graded thickness GaAs spacers. All samples (B-F) have 8 x 0.5 ML InAs depositions per SML QD. Thickness indicators in (d-f) indicate GaAs deposition (in ML) for each of the spacer layers. Chart below shows the color coding of the schematics in (a)-(f).

bilayer spacers, such that the spacer layer composition is determined by the relative thickness of the GaAs and AlGaAs layers, given in ML with AlGaAs thickness in bold, as [1.5/0.0, 1.5/0.0, 1.0/0.5, 1.0/0.5, 0.5/1, 0.5/1, 0.0/1.5, 0.0/1.5] for sample D and [1.5/0, 1.5/0, 1.0/0.5, 1.0/0.5, 1.0/0.5, 0.5/1.0, 0.5/1.0, 0.0/1.5] for sample E. For sample F, decreasing GaAs spacer thicknesses, in ML, of [2.5, 2.5, 2.0, 2.0, 1.5, 1.5, 1.0, 1.0] were used. While the schematics in figure 4.6 show the layered growth of the QD active regions, it is expected that significant alloying will occur in the QD active region, especially in the growth direction, such that it would be difficult to assign either thicknesses or material compositions to individual dot layers. More likely, vertical alloying of the QD would result in some mixing of the InAs SML and spacer regions, resulting in spatially varying ternary or quaternary alloys within the QD. Thus, we also show in figure 4.6, for each SML QD structure investigated, an approximate color-scale layer structure assuming some vertical alloying of the QD layers.

The use of the term "quantum dot" to classify these layered SML QD structures is traditional, and suggests quantum confinement in all 3 dimensions. While discussions of SML QD structures in the literature generally assume three-dimensional confinement, the high-resolution, near atomic-scale characterization techniques used to study these structures have been somewhat inconclusive on this front. From previous work, it would appear that lateral segregation of In is achieved in SML QDs, though this segregation is not nearly as defined as what can be achieved with SK QDs [67],[73],[74]. Extensive lateral and vertical alloying of our SML QD structures would obviate these current efforts to control dot energies via band structure engineering, giving only quantum well (QWs) with varying alloy compositions. To this end, we grew a QW control sample (sample A) to compare with our 8-layer InAs/GaAs SML QD sample (sample B). The QW sample consists of 3 periods of a 16-ML $In_{0.25}Ga_{0.75}As$ QW with the same cladding and buffer layers as all of our SML QD samples, as well as the same growth temperatures. The thickness and composition of the QW sample were designed to match those of the SML QD sample (A), were the entire QD active region to be uniformly alloyed (laterally and vertically).

The resulting PL from these two samples (A and B) is shown in figure 4.7. The PL peak of sample A is seen at 1.39 eV with a full-width at half-maximum (FWHM) of 40 meV, while sample Bs peak PL is observed at 1.38

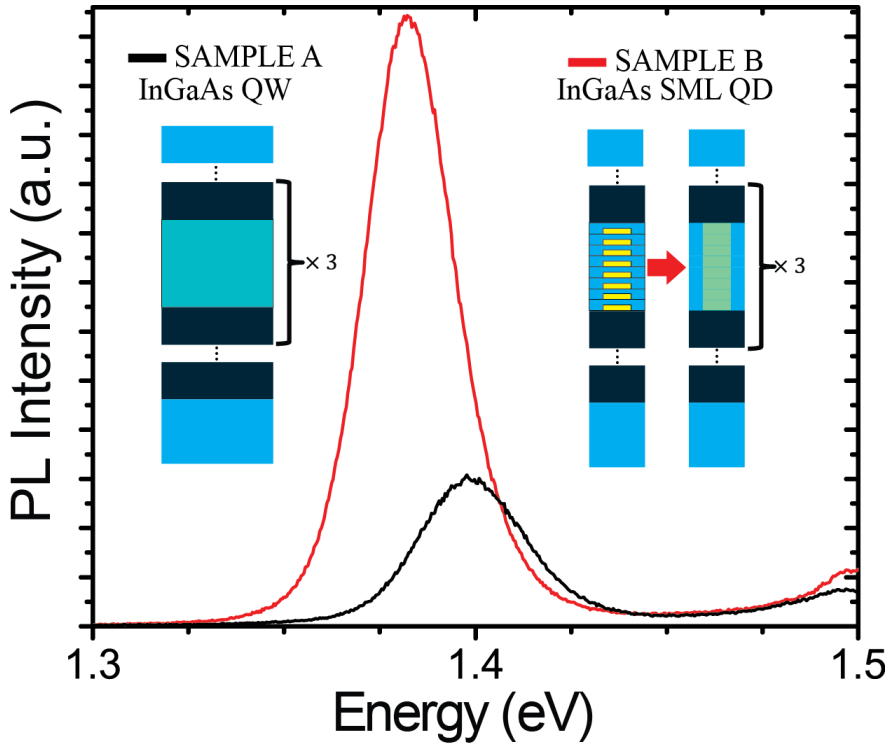

Figure 4.7: Comparison of low-temperature photoluminescence from SML QD sample [8 layers of 0.5 ML InAs and 1.5 ML GaAs spacers](red), with corresponding 16 ML $In_{0.25}Ga_{0.75}As$ QW sample with the same thickness and averaged indium fraction.

eV, with FWHM = 28 meV. The difference in the spectral peak of the PL emission from the two samples, while small (10 meV), is not insignificant, and combined with the rather significant difference in FWHM, suggests, at the very least, some difference between the SML QD and the QW sample. More noticeable is the significant difference in PL intensity, using the same experimental parameters, for the two samples, where a factor of 4.5 greater emission from the SML QD sample is observed, suggesting a fundamental difference in the light emission process for the two samples. However, while these results certainly suggest that the SML QD sample is not uniformly alloyed, neither the PL peak position nor the relative PL intensity can give extensive information regarding the extent and length scale of lateral In segregation, or the vertical and lateral alloying of the In-rich regions in our material. So far, one may want to ask: Why is the difference in the emission energy between sample A (QW) and sample B (SML QDs) so small? One should expect remarkably higher PL energy in sample B due to the enhanced

confinement of photoexcited carriers in QDs in comparison to the QW case. This can be explained as follows. Developing an accurate model of the grown SML QD structures would be remarkably complicated, due to the lack of information regarding the QD size, composition, density, and strain in the QD/QW active region. However, we can use a simple quantum box model, with separable wavefunctions, to gain some insight into the general behavior of our system. It is not the case that significant lateral quantization would necessarily result in remarkably higher PL energies. The energy position of the SML QD ground state depends on the interplay among a wide range of parameters (lateral size, In-concentration, QD areal density). With the only bound on our modeled system being the average In concentration across our QD/QW region, the variety of QD sizes, areal densities, alloy compositions, and geometries allowed is overwhelming. Thus, the model used is admittedly a vast simplification of the system we are investigating, utilized only to prove the larger point that the ground state PL for the SML QD is not required to be remarkably higher than that of a perfectly alloyed QW.

As an example, we studied the ground state energy of a dot modeled as a simple quantum box, assuming separable wavefunctions in x, y, and z, with AlGaAs (x = 0.35) barriers in the growth direction, and an average InGaAs alloy (x = 0.25) between the AlGaAs (x=0.35) barriers. Choosing a box size of 5 nm in both the x and y dimension to model our SML QD, we can vary the In content of the InxGa1-xAs SML QD from x=0.25 to x=0.5, by maintaining the SML QD size and changing the composition of the lateral barriers to maintain the total In concentration in the QD/QW region between the AlGaAs barriers.

Figure 4.8 plots the ground state energy difference between a 5 nm x 5 nm quantum box with lateral InGaAs confinement and an alloyed $In_{0.25}Ga_{0.75}As$ QW, as a function of the quantum box In fraction. For such a situation, the SML QD ground state energy peaked at an energy about 22 meV higher than the $In_{0.25}Ga_{0.75}As$ QW.

Even more In segregation is possible, though not without changing the dimensions or areal densities of the quantum boxes. Figure 4.9 illustrates the ground state energies of $In_xGa_{1-x}As$ quantum boxes with $x > 0.5$, and lateral barriers of GaAs. It should be noted that in this model, the areal density of the quantum boxes decreases, in order to maintain the correct average In content across the QD/QW region. For this case, a clear and con-

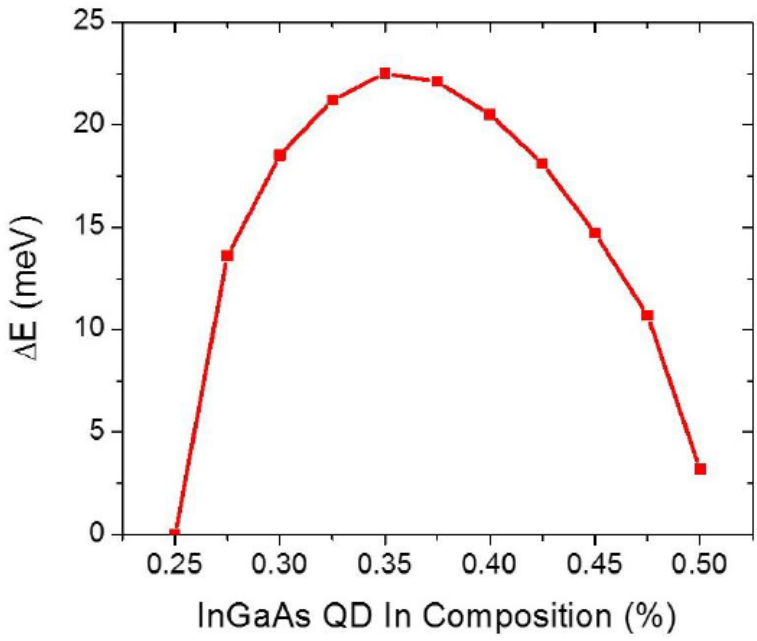

Figure 4.8: Ground state energy difference between a 5 nm x 5 nm quantum box with lateral InGaAs confinement and an alloyed $In_{0.25}Ga_{0.75}As$ QW, as a function the quantum box In fraction

sistent decrease in the ground state energy of the quantum boxes is observed. Thus, looking at the range of In concentration in the simple model of our InGaAs SML QDs, it can be seen that both positive and negative shifts in ground state energy can be achieved (when compared to the perfectly alloyed QW), and that the shift is only large (and negative!) with significant InAs segregation.

BFTEM and STEM imaging of SML QD samples are also studied. These samples consisted of the SML QD structures used in samples B and C (8 layers of SML InAs with 1.5 ML GaAs and AlGaAs spacers, respectively), separated by 2 nm of AlGaAs. The BFTEM images in figure 4.10 show nonuniform contrast in both (a) g=(220) and (b) g=(002) two-beam conditions, indicating inhomogeneous strain and variations in In content, respectively. The nanoscale strain and composition variations may lend a QD-like character to the SML QDs and can help to account for the PL shift from the QW case that was noted above. We also performed HAADF STEM and EDS mapping to gain a more precise picture of lateral and vertical In segregation during SML growth (see S1 and S2 in supplemental). However, we were unable to clearly resolve SML QDs, potentially due to redeposition

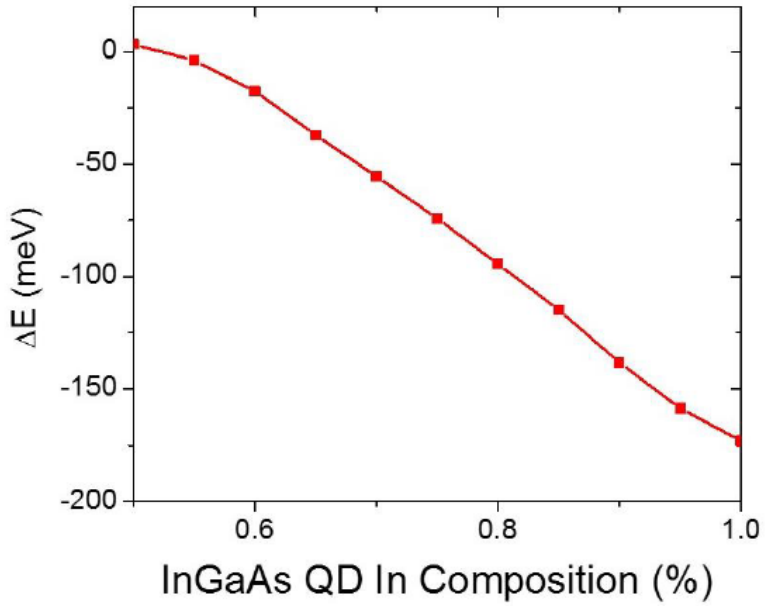

Figure 4.9: Ground state energies of $In_xGa_{1-x}As$ quantum boxes with x > 0.5, and lateral barriers of GaAs.

effects during ion milling. The low-temperature PL data for the five 8-layer

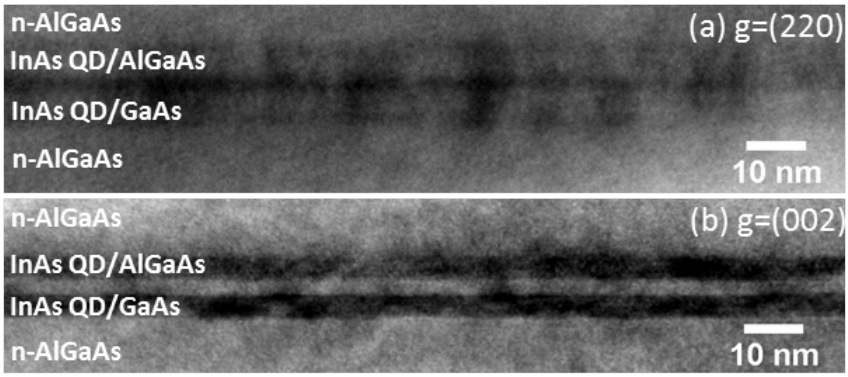

Figure 4.10: BFTEM of SML InAs deposition regions under (a) g = (220) and (b) g = (002) two-beam conditions showing inhomogeneities in strain and In content, respectively; images were taken from different regions of the sample. In the lower (upper) layer of both (a) and (b) the SML InAs deposits are surrounded by GaAs (AlGaAs).

SML QD samples (BF) are shown in figure 4.11. The sample with constant thickness GaAs spacers in the SML QD region, sample B, shows the lowest PL peak energy (1.38 eV) of all five samples. By decreasing the GaAs spacer thickness (from 3 to 1.5 ML) over the course of the SML QD growth (Sample

F), a small blue-shift of the PL emission (20 meV) can be observed, which would be expected for increasing Ga-concentration into an alloyed InGaAs SML QD. The sample containing only $Al_{0.35}Ga_{0.65}As$ in the spacer layers of the SML QD (C) shows the highest ground state PL energy among all four samples (1.66 eV), also as expected. It is important to note that in addition to the increased Al-content in the alloyed SML QD, an increase in lateral confinement is expected, as the surrounding QW material is now AlGaAs, as opposed to the GaAs QW for samples B and C. Furthermore, it is possible that the puddle size and density could be different for InAs SMLs grown on AlGaAs and GaAs due to the very different behavior of In adatoms on each of the growth surfaces [75]. Finally, the samples with the graded $Al_{0.35}Ga_{0.65}As$/GaAs barriers (D, E) show ground state PL energies (1.5, 1.57 eV respectively) between those of Samples B and C. The relative PL peak energies of D and E also track with averaged Al fraction across the graded barrier layers. In addition to the QD ground state and the GaAs bandedge PL peak (1.52 eV), a weak, broad peak at 1.56 eV is also observed for samples with lower ground state energies. We believe this emission to be related to impurity states in the low temperature growth AlGaAs in our sample, and not to the quantum structure of our SML QDs. This was verified by additional growths which began with an AlAs/GaAs superlattice (a well-known technique for confining/isolating impurities)[76], followed by the growth of low ground state energy QDs, and which did not show any PL at these energies.

The above results indicate the potential for control of SML QD energies via engineering of the internal bandstructure of the QD itself. Samples have been investigated by low-temperature PL spectroscopy, and a wide range of QD ground state energies, from 1.38 eV to 1.88 eV, has been observed. A clear difference in the PL intensity and FWHM (as well as a smaller difference in PL peak position) has been demonstrated between the 8-layer SML QD sample and its equivalent QW control sample, suggesting control of localized states, as opposed to simply a variation in QW emission via changing alloy composition. Though unintentional alloying of the QDs likely prevents the sort of exact bandstructure engineering achievable in other semiconductor heterostructures such as quantum cascade lasers, these results do indicate that significant control of the SML QD ground state is possible, and that the potential exists for possible control of SML QD excited states. The re-

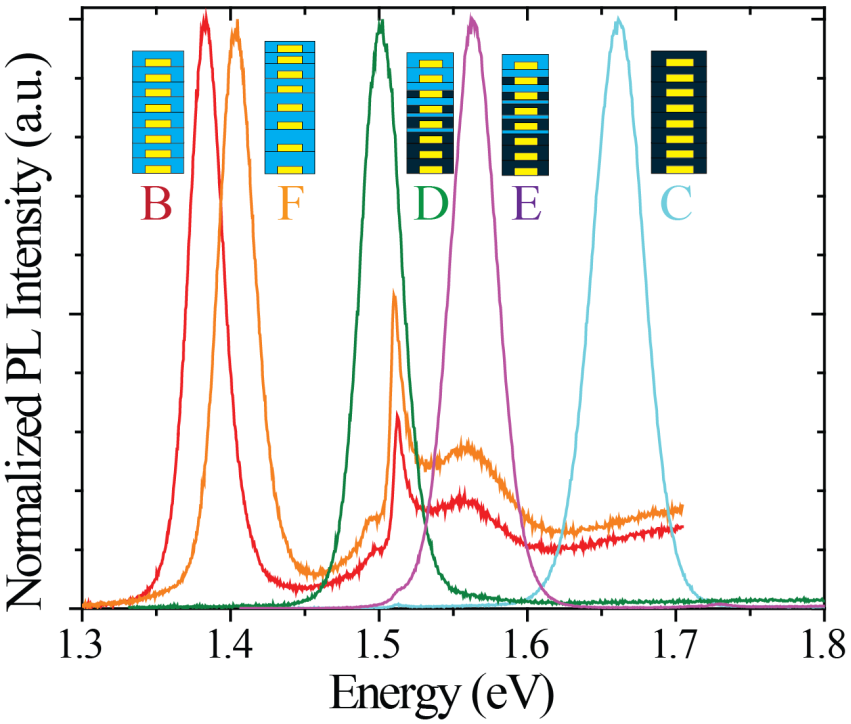

Figure 4.11: PL comparison of five samples with 8-layer InAs SMLs and 1.5 ML GaAs spacers (red), graded GaAs spacers (orange), graded AlGaAs/GaAs spacers (green and purple) and AlGaAs spacers (blue).

sults from this work suggest the potential for engineering of energy states in nanostructures using internal submonolayer bandstructure engineering with the potential for increased control of QD energies in a variety of optoelectronic devices.

4.4 Integration of Engineered SML QDs with Quantum Cascade Structure

After we studied the capability to control ground state energy of InAs SML depositions, we designed a quantum cascade structure using the stack of SML InAs/spacer in the active region. Figure 4.12 shows the biased band structure and the energy states simulated of the active region, using a 1-D program written by Professor Wasserman. We grew the structure and fabricated the samples into edge-emitting laser structures, but we had little luck with the

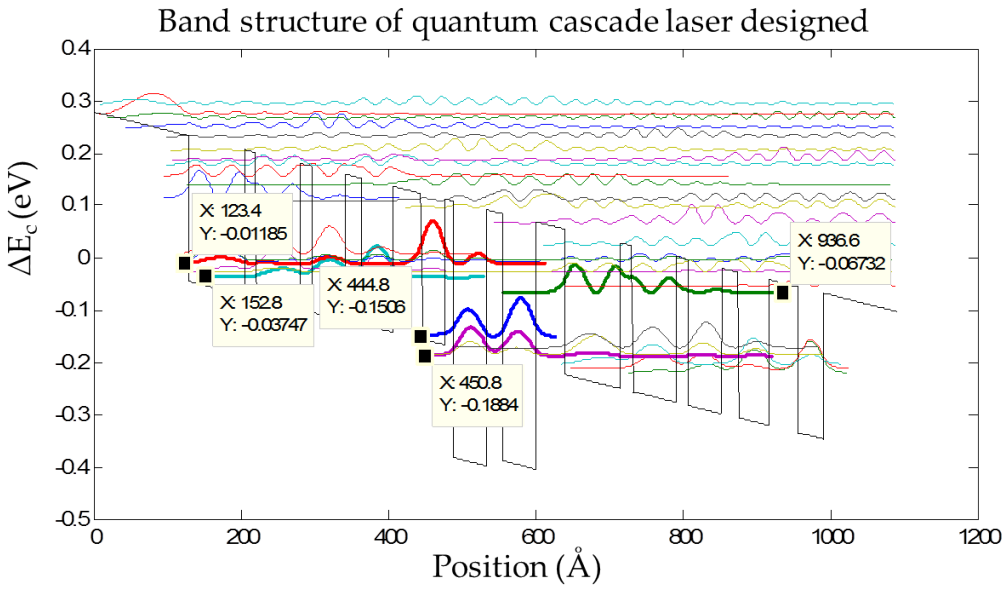

Figure 4.12: Designed quantum cascade structure using InAs SML quantum dots

intersubband emission of such structures, we think mainly because the SML InAs deposition does not form high-density and high-uniformity QD. This can also be seen from the TEM taken in figure 4.10. In the future, in order to fabricate QDCL, further study of high-density and high-uniformity QD formation needs to be done.

CHAPTER 5

MID-INFRARED EMISSION FROM IN(GA)SB THIN LAYERS IN INAS MATRICES

5.1 Type-II Material

In this chapter we discuss efforts to grow and fabricate room temperature, high efficiency mid-IR light sources (LEDs and lasers). In particular, we are looking to develop a straightforward quantum structure capable of emulating the interband diode emitters ubiquitous at shorter wavelengths. The quantum well structure is a good candidate; however, as mentioned in the first chapter, for type-I material, the emission wavelength is limited by the material bandgap. For instance, InAs has a bandgap of 354 meV (3.5 μm) at 300 K. The only III-V binary material with a lower bandgap is InSb, which is 170 meV (7.3 μm) at room temperature. However, InSb is not lattice matched to any commonly used substrate, or any other III-V binary, ternary, or quaternary compound, making it difficult to integrate into any semiconductor optoelectronic device architecture. Although the QCL and ICL already serve as powerful (and commercially available) light sources for the mid-IR, the fact that both of them require complicated bandstructure engineering and sophisticated epitaxial growth has led to interest in developing mid-IR emitters with simpler structures able to cover 3 μm to 8 μm wavelength range [77],[78],[79],[80]. Type-II material, with its special band alignment, where the conduction band edge of InAs lies below the valence band edge of the adjacent (In)GaSb, leading to spatial separation of electrons and holes, has carrier recombination between two different materials, thus eliminating the limitation of material bandgap [81],[82],[83]. Thus, we are looking to achieve mid-IR LED devices, with emission wavelengths between 3 μm and 8 μm, using straightforward type-II quantum structures. To do so, we utilize MBE grown type-II In(Ga)Sb quantum wells grown in an InAs(Sb) matrix. This chapter details the growth of such structures, as well

as the optical and electrical characterization of the resulting devices.

5.2 Type II In(Ga)Sb Insertion Layers in InAs(Sb) Matrices

Thin InSb layers, when grown in InAs matrices, may have potential applications as a mid-IR optoelectronic material system. InSb has a type-II broken band alignment with InAs, as shown in figure 5.1(a) and 5.1(b). However, InSb and InAs are not lattice-matched. The lattice mismatch between InSb and InAs (6.5%) is close to that between InAs and GaAs (6.7%), a system known for facilitating the growth of self-assembled quantum dots (SAQDs). Thus, at first blush, it would appear as though InSb QDs [84],[85],[86],[87], when formed on InAs surfaces, would allow for optical transitions between three-dimensionally confined holes in the InSb QD layer and the electrons in the surrounding InAs matrix, leading to emission wavelengths in the 3-8 μm range. In order to systematically study this type-II material system, instead of trying to grow QDs directly, we start with thin deposited QW emitter structures. The unstrained band alignment of type-II material is shown in figure 5.1. For radiative recombination, electrons from the InAs conduction band need to recombine with quantum confined holes from the In(Ga)Sb valence band. The structures of the first series of type-II emitters grown in this

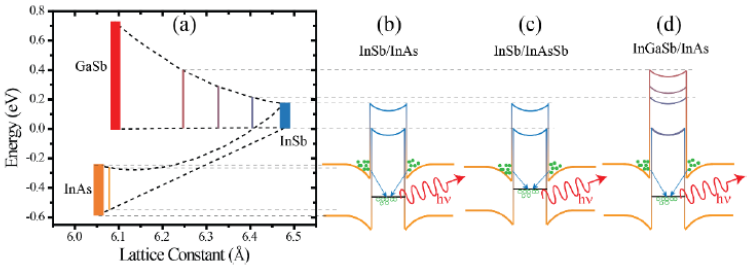

Figure 5.1: (a) InAs (orange), GaSb (red) and InSb (blue) band gaps and unstrained band alignment, as well as the bandgaps, lattice constants, and band alignments for InAsSb and InGaSb (dashed lines). Schematics of band structure and interband optical transitions for (b) InSb on InAs, (c) InSb on InAsSb and (d) $In_xGa_{1-x}Sb$ (for x = 0.4, 0.6, and 0.8) on InAs.

effort are shown in figure 5.2. For each sample, the light emitting, or active region, consists of three layers of In(Ga)Sb grown with thicknesses varying

from 1 to 1.75 ML, separated by intrinsic InAs having thicknesses varying from 5 nm to 30 nm. The growth process and parameters used for each layer are as follows:
1) i-GaAs buffer: Tsub = 610 ^{o}C, GR = 1.67 A, As pressure = $3.0 * 10^{-6}$ Torr
2) Lower the substrate temperature to 510 ^{o}C and annealing for 10 sec
3) i-GaSb buffer: Tsub = 510 ^{o}C at the beginning, then slowly increase to Tsub = 545 ^{o}C, Sb pressure in our chamber: $3.5 * 10^{-7}$ Torr, GR = 1.1 A/s
4) Lower the substrate temperature to 460 ^{o}C
5) i-InAs: Tsub = 460 ^{o}C, GR = 5 A/s As pressure = $4.5 * 10^{-6}$ Torr in our chamber
In the active region:
6) In(Ga)Sb thin layers: Tsub = 470 ^{o}C, group III element flux = 0.43 ML/s, Sb pressure = $1.0 * 10^{-7}$ Torr in our chamber
7) i-InAs spacer: Tsub = 460 ^{o}C, GR = 3 A/s As pressure = $4.5 * 10^{-6}$ Torr
8) the In(Ga)Sb thin layer & InAs spacer is repeated three times for each sample
9) i-InAs cap layer: Tsub = 460 ^{o}C, GR = 3 A/s, As pressure = $4.5*10^{-6}$ Torr

For all of the samples grown, we add an additional surface layer, grown under the same conditions as the buried layer. This surface layer is used for surface topography studies using AFM. Whereas Tsub stands for substrate temperature, GR stands for growth rate. Please note that the pressure used for our growth may only be valid for our own system; calibration may still be needed for another MBE system.

Figure 5.3 shows the PL taken from the above samples. As the thickness of the thin InSb insertion increases from 1 ML to 1.75 ML, the emission wavelength red-shifts from 3.65 μm to 5.75 μm. Figure 5.3(b) shows the low T PL from the thin InSb layers in an InAsSb matrix, for increasing thicknesses of InSb. This data also shows a red shift from 6.2 μm to almost 8 μm. From the PL spectral, we can see that both 1.5 ML and 1.75 ML InSb in InAs samples show a low energy shoulder beside the primary peak, which is not observed for the samples grown in InAsSb matrix. This will be discussed in more detail later.

In addition, we investigated the Ga content of the In(Ga)Sb layer. Adding Ga changes the lattice constant (reducing the lattice mismatch) of the thin

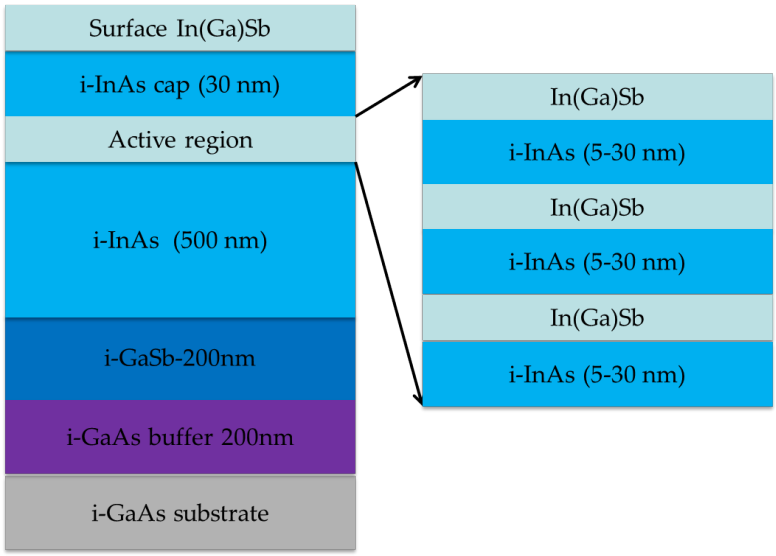

Figure 5.2: Sample structure of thin epitaxially grown In(Ga)Sb layers in InAs matrices.

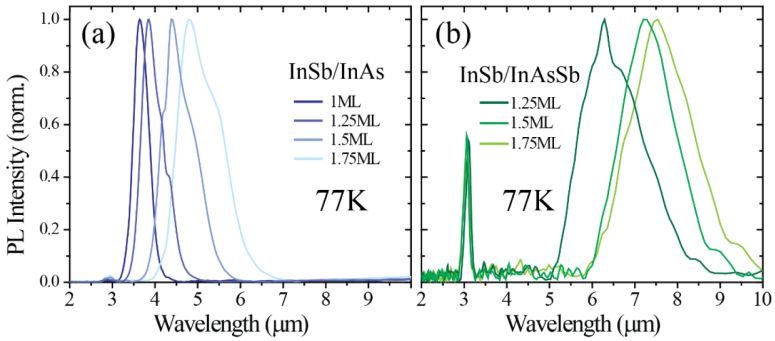

Figure 5.3: Normalized 77 K photoluminescence spectra from (a) InSb layers of increasing thickness grown on InAs and (b) InSb layers of increasing thickness grown on InAsSb.

layer, but does not affect the hole confinement. This is because, as shown in figure 5.1, for $In_xGa_{1-x}Sb$, changing Ga-content causes significant change in the conduction band offset with InAs, but only negligible change in the valence band offset with InAs. A second sample is grown to study emission of the InGaSb thin layer. The sample structure is shown in figure 5.4(b), which contains three layers of 1.75 ML $In_xGa_{1-x}Sb$ with changing Ga fraction from x=0.6, x=0.4 to x=0.2, separated by 150 nm InAs layer. With each layer etched off, the PL from the layer closest to the surface is collected (figure 5.4(a)). The emission wavelength of those three layers is 4.5 μm with only minimal change in the spectral position or shape because changing

Ga fraction only changes the conduction band offset of $In_xGa_{1-x}Sb/InAs$, resulting in negligible change of confined hole state energy in the $In_xGa_{1-x}Sb$.

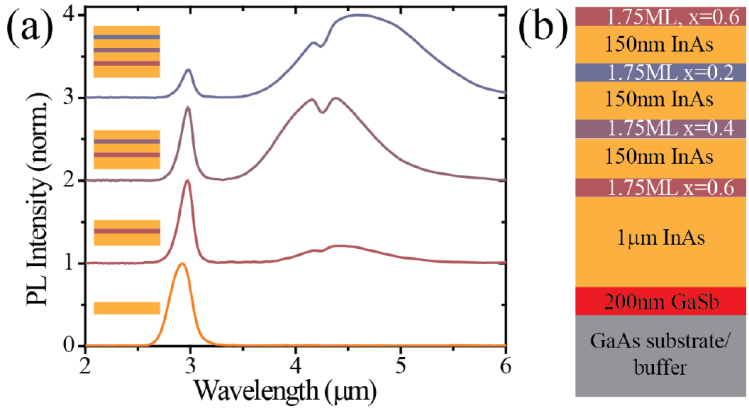

Figure 5.4: (a) Photoluminescence spectra from sample shown schematically in (b) with 1.75 ML $In_xGa_{1-x}Sb$ layers with increasing Ga alloy concentration. The four PL spectra shown in (a) correspond to, from top to bottom, samples with zero, one, two, and finally, all three InGaSb insertions etched off.

Notably, for the narrow bandgap material, Auger recombination can be a limiting factor of the emitter device performance, especially for high temperature operation, where Auger recombination dominates the recombination mechanism. In order to better understand the temperature performance of our emitters, we collected temperature-dependent PL from all of the samples mentioned above. Figure 5.5(a)-(d) show temperature-dependent PL for four samples: the 1.0 ML InSb/InAs, the 1.75 ML InSb/InAs, the 1.75 ML $InSb/InAs_{0.97}Sb_{0.03}$, and the 1.75 ML $In_{0.4}Ga_{0.6}Sb/InAs$. The integrated intensity of the insertion layer PL for each of the above samples is shown in figure 5.5(e) as a function of temperature, with all data points normalized to the 77 K peak PL value to better understand the relative change in PL intensity. Since the 1.75 ML InSb/InAs sample has two peaks at low temperature, each PL spectrum at each temperature was fit with a multi-peak Gaussian and the integrated intensity of each of the two peaks is plotted in figure 5.5(e). The four samples shown here have significantly different temperature performance. The 1 ML InSb/InAs sample (figure 5.5(a)) shows the most rapid decay of PL intensity as a function of temperature. A result of the fact that this structure will have the weakest hole confinement in the

InSb layer. The 1.75 ML InSb/$InAs_{0.97}Sb_{0.03}$ sample (figure 5.5(b)) shows a slightly slower decay in intensity with temperature due to its better hole confinement in the thicker InSb layer. The temperature behavior of the 1.75 ML InSb/InAs sample (figure 5.5(c)) is remarkably different because of its two peaks. For this sample, a fast initial decay in the lower energy emission peak but a much slower decay in the high energy peak with temperature is observed. Above 150 K, PL from the lower energy transition can no longer be observed, and the higher energy peak begins to decay with temperature much faster. We believe that this behavior can be explained by assuming two hole states in the InSb valence band. As temperature increases, holes are thermally excited from the lower energy state, and emission shifts to the higher energy state. Overall, the 1.75 ML InGaSb/InAs sample (figure 5.5(d)) shows the best temperature performance among all samples.

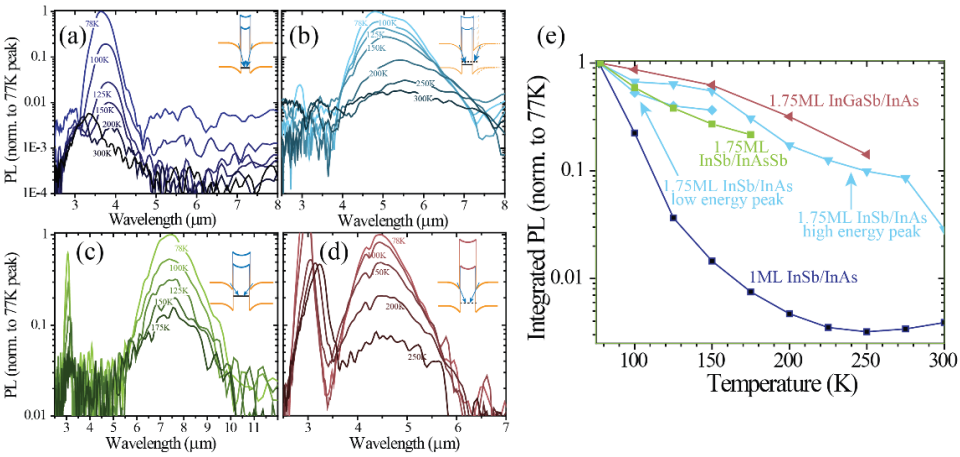

Figure 5.5: Temperature-dependent PL spectra for (a) 1.0 ML InSb/InAs, (b) 1.75 ML InSb/InAs, (c) 1.75 ML InSb/InAsSb and (d) 1.75 ML InGaSb/InAs samples, with insets showing the respective bandstructure. Each spectrum was normalized to the amplitude of the In(Ga)Sb insertion PL peak at 77 K. (e) Integrated PL intensity for In(Ga)Sb insertion layers as a function of temperature.

AFM is then performed of the surface layers of each of the samples. Figure 5.6 shows surface AFM scans of three samples: 1.75 ML InSb on InAs, 1.75 ML InSb on $InAs_{0.97}Sb_{0.03}$, and 1.75 ML $In_{0.4}Ga_{0.6}Sb$ on InAs. As can be seen from the images, there is no indication of QD formation on either the InSb/InAs or the InSb/$InAs_{0.97}Sb_{0.03}$ growths. However, for the $In_{0.4}Ga_{0.6}Sb$/InAs sample, the AFM shows nano-structure (QD) formation

with a bimodal size distribution. The smaller dots have an average diameter of 28 nm and a height of 3.4 nm, while the larger dots have diameters near 40 nm and heights of 8.3 nm. The surface layer of the InSb insertion on InAs(Sb) surfaces is very smooth, showing no evidence of significant dislocations or defects at the growth surface. However, the lack of QD formation in our InSb/Inas samples agrees with previous InSb/InAs publications demonstrating dot formation only for depositions greater than 1.8 ML of InSb.

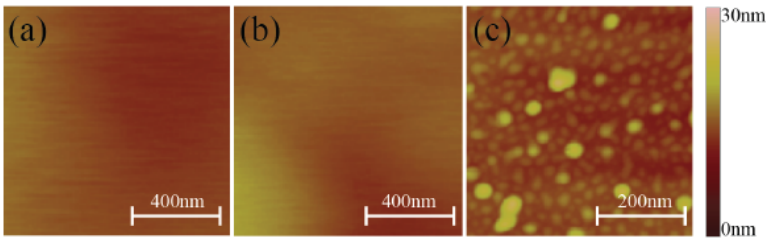

Figure 5.6: Atomic force micrographs (AFM) of In(Ga)Sb layers deposited on InAs(Sb) surfaces. (a) 1.75 ML InSb on InAs, (b) 1.75 ML InSb on $InAs_{0.97}Sb_{0.03}$, and (c) 1.75 ML $In_{0.4}Ga_{0.6}Sb$ on InAs. No evidence of QD formation was observed on either of the InSb samples, while clear nanoscale features were observed for the InGaSb layer grown on InAs.

In order to better understand the nature of the InSb insertions, we grew another two samples for TEM study. The first consisted of three InSb layers of thicknesses 0.5, 1.0, and 1.5 ML grown in an InAs matrix, while the second consisted of three 1.5 ML InSb layers grown on $InAs_{0.97}Sb_{0.03}$. The results from the TEM studies are shown in figure 5.7(a) and 5.7(b) (provided by Professor Jianmin Zuo's group in UIUC). For the InSb/InAs sample, a discontinuous InSb layer can be seen in the 0.5 ML insertion TEM image, which is expected for a submonolayer insertion. For the 1 ML InSb insertion layer, a uniform quantum well is observed. However, for the 1.5 ML insertion, a thickness variation is observed from the TEM image, which is the early stage of QD formation. For the $InSb/InAs_{0.97}Sb_{0.03}$ sample, no thickness variation is observed, unlike the 1.5 ML InSb/InAs sample.

With the AFM and TEM, we can better understand the optical properties of this material system. For the low temperature PL data (figure 5.3), we see a low energy shoulder in the samples 1.5 ML InSb/InAs and 1.75 ML InSb/InAs, but not the samples grown in the InAsSb matrix. The low

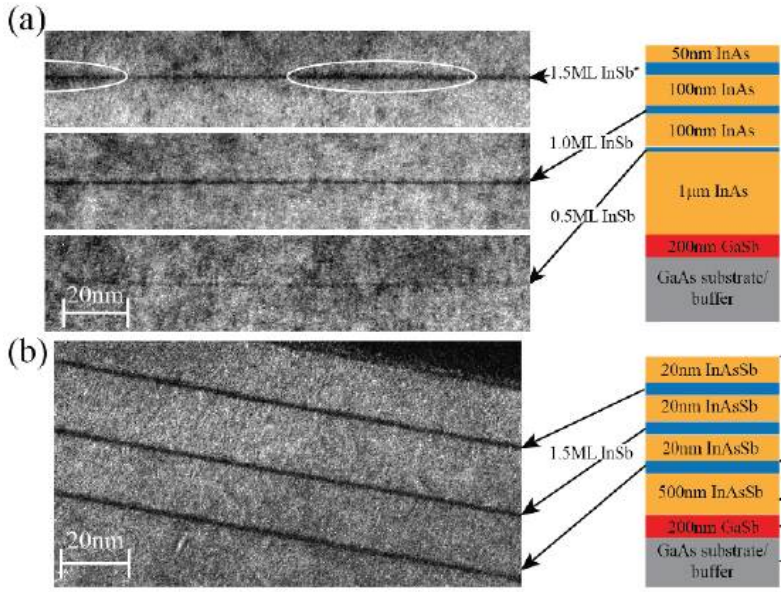

Figure 5.7: DF-TEM images and schematics of three layer samples with (a) 0.5, 1.0, and 1.5 ML of InSb grown on InAs and (b) three 1.5 ML InSb insertions grown on $InAs_{0.97}Sb_{0.03}$.

energy shoulder comes from the laterally confined carriers, where we see the thickness variation from TEM, and the high energy peak comes from the quantum well like structure. No low energy shoulder is seen from the InSb/InAsSb samples because of the uniform quantum well structure.

5.3 Time-Resolved PL

The previous results already show the potential of fabricating type-II material into mid-IR emitters covering the wavelength range from 3 μm to 8 μm. However, it is important to recognize that as narrow band materials are incorporated into optoelectronic device structures, the carrier dynamics in these systems can change dramatically. Most notably, for these narrow band materials, Auger recombination can very quickly become a limiting factor in device performance. For photodetectors, long carrier lifetimes are required in order to electrically extract photoexcited carriers, improving the efficiency and sensitivity of the detector. For these devices, which typically operate at low carrier injection levels, Auger recombination is less of a problem, and efforts to improve carrier lifetimes focus primarily on the defects and traps

which can dominate carrier dynamics at low carrier concentrations. Lifetimes for excited carriers in mid-IR detectors with narrow band gap materials can be as high as 1 μs (measured at low injection levels). For sources, however, the requirements on carrier lifetimes are slightly more complicated, and it becomes necessary to differentiate between radiative and non-radiative recombination. In general, long non-radiative recombination times are always desired, as any excited carriers lost to non-radiative effects only serve to decrease the emitter efficiency. Radiative lifetimes, however, should generally be relatively short, in order to ensure efficient light emission in LEDs, low threshold currents and high slope efficiencies in lasers, and potentially high-speed modulation of both LEDs and lasers. In order to develop more efficient mid-IR sources based on electron-hole recombination in semiconductor diode structures, methods must be developed to both measure and manipulate carrier lifetimes in these materials. In my project, we set up our own TRPL system in our lab (as mentioned earlier in Chapter 2).

5.4 Carrier Lifetime Study of the InAs/In(Ga)Sb Emitters

We tried to take the TRPL data from the samples with different InSb insertion in the InAs matrix. However, the TRPL intensity decays faster than the detector response time (4.25 ns), in which case no conclusive information can be extracted. Thus, our initial InSb/InAs samples, which showing strong low temperature (77 K) emission, are unlikely to make for efficient LEDs. This was already indicated by the poor temperature performance of these emitters. One way to reduce Auger recombination is to introduce quantization into the system. Thus, in order to better understand the carrier dynamics in our material system, four more samples have been grown and studied. The sample structures are very similar to previous samples except that in the active region, we grow three layers of 3 ML InSb separated by InAs with different thickness (5 nm, 10 nm and 30 nm). For another sample, which has 10 nm InAs separation, an addition barrier containing three layers of 3 nm $In_{0.8}Ga_{0.2}As$ separated by 2 nm InAs is grown on either side of the active region (figure 5.8). The low-T PL is tested for those samples, as well as the sample with nano structure formation from AFM in the last section (figure

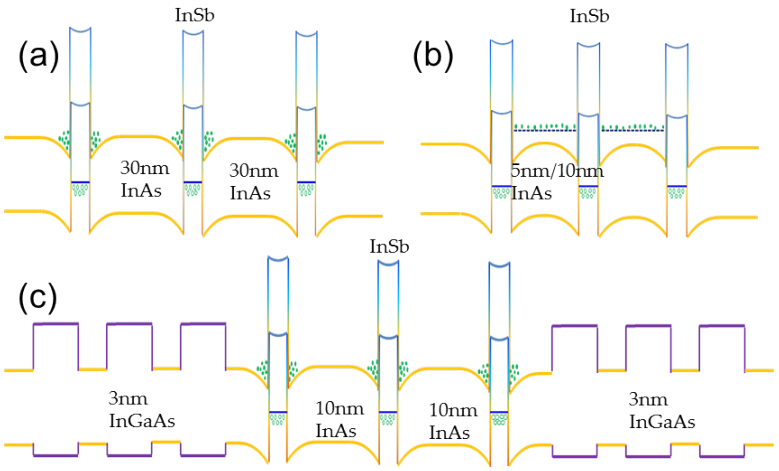

Figure 5.8: Band structure for four samples grown for TRPL study: (a) 1 ML InSb separated by 30 nm InAs, (b) 1 ML InSb separated by 5 nm/ 10 nm InAs, (c) 1 ML InSb separated by 10 nm InAs but with three layers of $In_{0.8}Ga_{0.2}As$ (3 nm each) on each side of the active region.

5.9). The PL peak blue-shifted from 4.65 μm (from the sample with 30 nm InAs spacer) to 4.2 μm (from the sample with 5 nm InAs spacer). This is caused by the increased electron quantization introduced by the narrower separation InAs layer, which forms a quantum well.

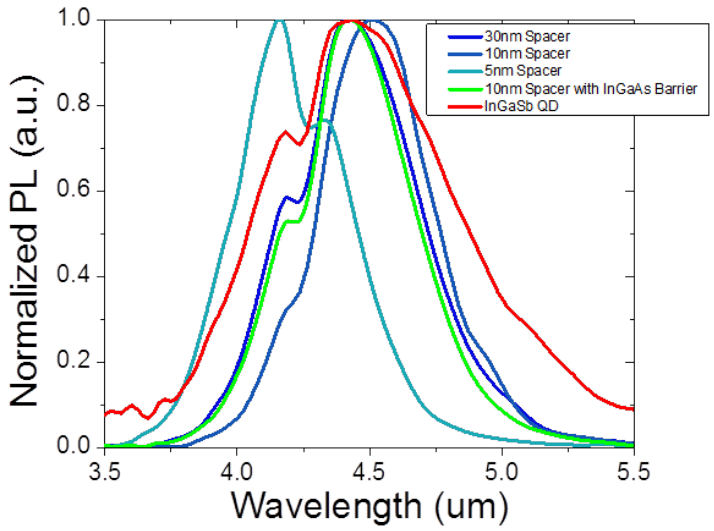

Figure 5.9: PL taken from the four samples newly grown and the sample with nano structure formation from the last section for TRPL study.

The TRPL of the four samples with different pumping power were collected

and are shown in figure 5.10, where a slope kink can be seen in (a), (b) and (d). According to [88], at high excess carrier density, where the excess carrier density is greater than the intrinsic carrier density (to the left of the kink line in the figure), Auger recombination and radiative recombination dominate, while at low excess carrier density, where the excess carrier density is smaller than the intrinsic carrier density (to the right of the kink line in the figure), SRH recombination dominates. Since the SRH recombination rate (equation (5.1)) is a constant when excess carrier Δn becomes smaller than the intrinsic carrier density n_0, the slope is constant after the kink for the same sample at different initial pumping power (more details about the TRPL data meaning are given in section 2.3.). However, for the sample with 1 ML InSb, InAs spacer layer and InGaAs barrier, no obvious kink is observed; this is because adding InGaAs barrier introduces more strain, as well as additional interfaces, to our structures, which then likely increases the number of defects in the emitter, resulting in a large SRH recombination rate and a very steep slope at low excess carrier density.

$$\tau_{SRH}^{-1} = \frac{n_0 + \Delta n}{\tau_{p0}(n_0 + \Delta n) + \tau_{n0}\Delta n} \tag{5.1}$$

Using the fitting method mentioned in section 2.3, we fitted the TRPL data above and extracted the SRH recombination rate (A), radiative recombination rate (B) and Auger recombination rate values from those samples (shown in table 5.1). As expected, the sample with InGaAs barrier has the largest A value, indicating that adding lattice-mismatched barrier introduces more defects in our material system. The samples with 5 nm InAs spacer and 10 nm InAs spacer have similar A values, meaning that these two samples have nearly equal numbers of defects. The sample with InGaSb nano-structure formation has the smallest A, which can be explained by the strain-relaxed structure of the 3D nano-structure. Thus, the sample with nano-structure formation should have the fewest dislocations.

As expected, the sample with obvious nano-structure has the largest radiative B value, followed by the sample with smallest InAs spacer. The one with InGaAs barrier has the smallest radiative recombination rate, which, again, is caused by the poor material quality. However, due to the RC time delay from the MCT detector (4.375 ns), the extracted Auger recombination from our samples should not be trusted because the carrier lifetime from Auger

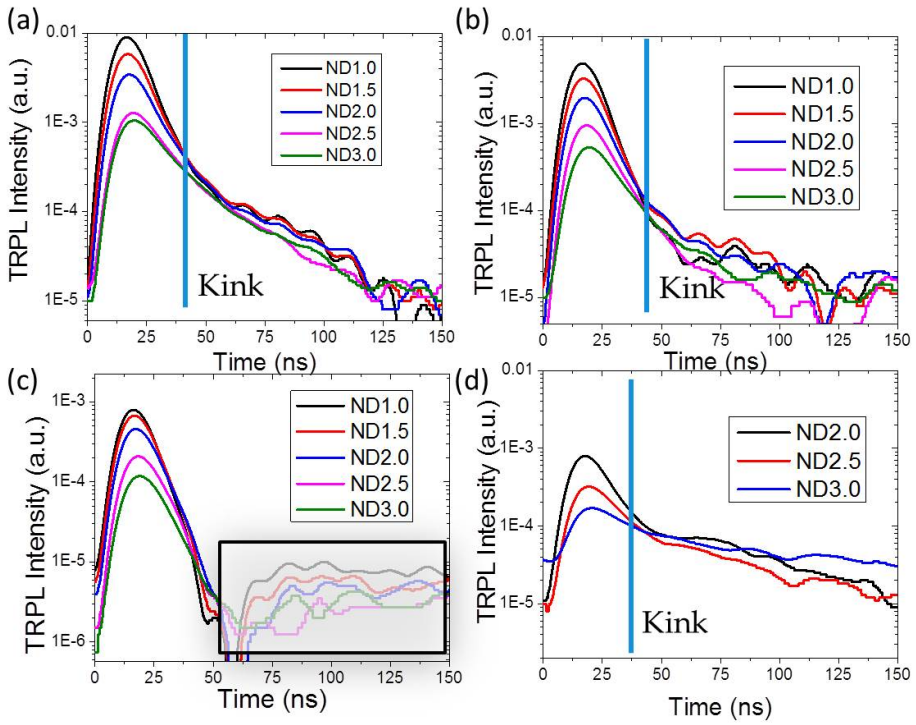

Figure 5.10: Power dependent TRPL from (a) 1 ML InSb with 10 nm InAs spacer, (b) 1 ML InSb with 5 nm InAs spacer, (c) 1 ML InSb with 10 nm InAs spacer and InGaAs barrier (the shaded area is noise from the measurement system), (d) 1.75 ML InGaSb/InAs with nanostructure formation.

recombination is much shorter than the time delay from the detector.

From the results we get in this chapter, we can draw the following conclusions:

- In(Ga)Sb/InAs Type-II material system has the potential for future mid-IR applications since it is very easy to control the emission wavelength (in 3 μm to 8 μm range) and the emitter structure itself is much simpler than the previously mentioned QCL, ICL and type-I QW mid-IR emitter structures.

- From all the samples studied and tested, the one sample with obvious 3D nano-structure formation has the fewest defects, largest radiative recombination rate.

This indicates that the type-II QD structure in this material system will be

Table 5.1: Comparison of A and B values between QD sample and samples with different InAs spacers

Sample	A ($*10^7/s$)	B ($*10^{-9}cm^3/s$)
InGaSb nanostructure	3.5	6.2
5 nm InAs spaced	6.6	4.7
10 nm InAs spaced	6.8	4.5
10 nm InAs spaced with InGaAs barriers	32	2.3

the best candidate for future mid-IR emitter, laser and detector development. So for now, the first step is to develop a robust procedure to grow In(Ga)Sb QD in our MBE system. In the next chapter, we will discuss the growth of In(Ga)Sb QD.

CHAPTER 6

INGASB QUANTUM DOTS ON INAS: GROWTH AND CHARACTERIZATION

6.1 Proposed Growth Approach for InGaSb QDs

As described in the previous chapter, the sample in which clear QD formation was observed showed improved temperature performance, as measured by T-dependent PL and low-temperature TRPL. For this reason, we decided to focus on better understanding the growth of quantum nanostructures in the In(Ga)Sb/InAs type-II material system. As mentioned in chapter 4, for all emitter samples grown in this chapter, a 100 nm GaSb buffer layer is grown using the two-step method to capture the dislocations caused by the lattice mismatch between GaAs and GaSb. A 400 nm thick undoped InAs layer is then grown above the GaSb layer, followed by the active region growth. The biggest challenge for high-density In(Ga)Sb QD growth is that the In atom has a very high surface diffusion length on Sb-terminated surfaces because of the weak In-Sb binding energy. A few things can be done to possibly solve this problem. First, lowering the growth temperature can be a direct method to lower the surface mobility of In atoms in the growth front, which will then theoretically give a better chance to have In atoms conglomerate as small size QDs instead of forming a layer of In(Ga)Sb. Adding Ga atoms into the thin layer deposition also helps, since Ga atoms have a much smaller surface mobility which can limit the In atom surface diffusion length on the Sb terminated surface. In addition, controlling the III to V element ratio can also help because if we can manage to form QD on As-terminated surface, which will eliminate the effects of weak In-Sb binding energy, then we will have a much better chance to form high-density QDs. Figure 6.1 is a summary of the methods mentioned above and the reasoning behind each method. The primary characterization methods used in this chapter are mid-IR PL, AFM and TRPL, using the setups described in previous chapters. In our project,

Parameter/method planned to change	Reason
Ga/In ratio: 0.5/0.5, 0.4/0.6, 0.3/0.7, 0/1.0	Ga atom has a much smaller surface mobility, which will limit the In atom surface diffusion length.
Lower substrate temperature: 360 °C to 430 °C	Lower temperature will limit In atom surface mobility
Two step growth method: deposit In(Ga)Sb at low T(~300°C), then bring up to relative high T for short anneal	At really low T, Sb-solid cluster forms preventing In migration, then high T annealing allows excess Sb evaporation.
III-V ratio: 2:1, 1:1, 1:2	If nucleating QD on As-terminated surface, then In surface diffusion length will be limited.

Figure 6.1: Ways to approach high density and high quality QDs. In our work, we tried varying Ga/In ratio, controlling the growth substrate temperature, and the III-V ratio.

we tried varying the Ga/In ratio, lower growth substrate temperature.

6.2 Zoo Sample Study

A wide range of parameters can affect QD formation in our material system, such as substrate temperature, III-to-V ratio (including both III element flux and V element flux), growth rate, In(Ga)Sb layer thickness, In/Ga ratio and pre- or post-growth annealing time. In order to sweep a large parameter space efficiently, we came up with an idea of growth method, which we call a "Zoo" sample. Figure 6.2 is an example of one zoo sample we grew with three substrate temperatures combined with three Ga/In ratios. In the active region, we grew three stacks of dot layers each separated by a 300 nm InAs layer. In each stack, we grew three layers of In(Ga)Sb with different growth parameters, each separated by 100 nm InAs. So, for each zoo sample, we have nine different combinations of growth parameters studied. On the sample surface, we pick one set of parameters used in the nine layers and grow a surface dot layer for AFM study.

After growth, we etch the sample layer by layer and take the PL of each layer. The etching process is as follows: 1) Use wax to cover half of the sample. 2) Put sample into wet etching solution for a few minutes. 3) Use Alpha step profilometer to test the etch depth and decide which layer we etched to on this sample. The wet etching solution used for our material is citric acid : hydrogen peroxide = 2 : 1. Note that since the wet etching for this material is not very stable, a calibration is necessary before etching the real sample each day. Usually we use the first sample etched as a calibration

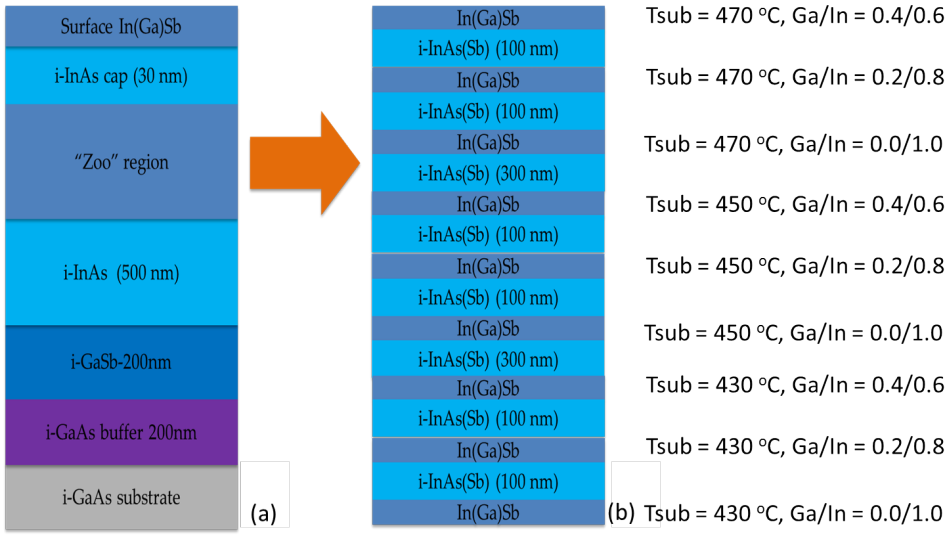

Figure 6.2: (a) Sample structure and (b) nine layers of thinly deposited In(Ga)Sb with different growth parameters.

sample. Though the etch rate can vary across samples, and from day to day, the average etch rate we obtain is 0.8 nm/s $\pm$ 0.2 nm/s.

Initial efforts focused on growing numerous samples containing InSb/InAs layers following the parameters used in the literature; however, none of these gave us obvious quantum dot formation. Figure 6.3 shows the AFM (figure 6.3(a)) and temperature-dependent PL (figure 6.3(b)) from one of the InSb emitter samples. The growth parameters used for the thin deposited layer in this sample are: Tsub = 470 ^{o}C, growth rate (GR) = 0.1 ML/s, Sb pressure = $2.5 * 10^{-7}$ Torr, thickness = 1.5 ML, annealing under Sb for 30 s after thin layer deposition.

In our system, the AFM of most of our InSb emitter samples gives results similar to the AFM micrograph shown in figure 6.3(a). Although this sample emits from 77 K all the way to room temperature, the emission intensity drops dramatically as temperature increases, which is not ideal for a room-temperature emitter device and, as described in the previous chapter, is a trend we generally associate with thin, planar layers (and the absence of QD formation). It should be noted that a few research groups have demonstrated growth of InSb QDs on InAs surfaces [89],[90]. The QD density in these samples has generally been rather low (in the order of $10^9/\text{cm}^2$). Despite the few demonstrations in the literature [89],[90], there has been little in the way of broad parameter space searches for InSb QD formation on InAs surfaces.

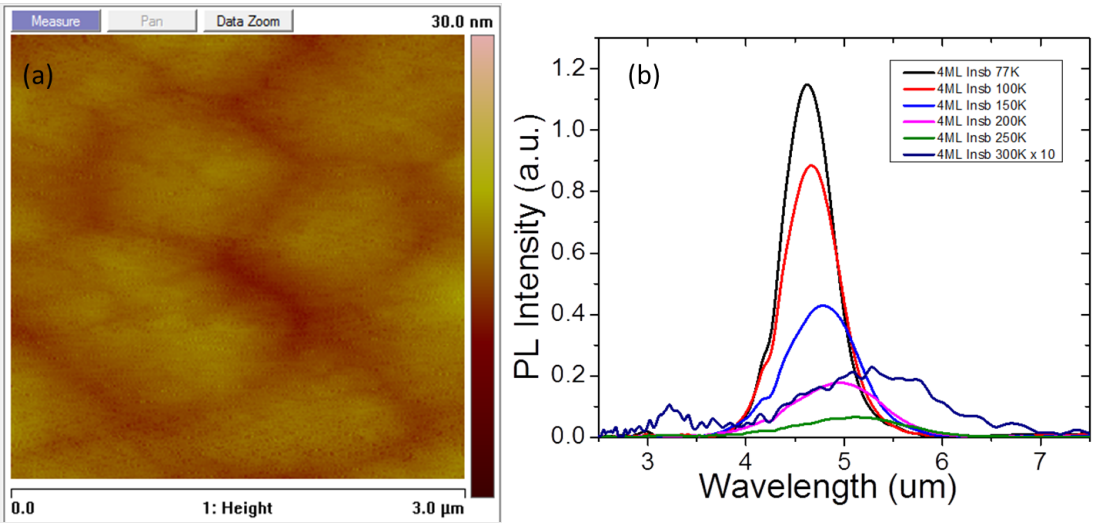

Figure 6.3: (a) AFM scanned from the surface layer of a InSb emitter. (b) T-dependent PL taken from the InSb sample.

Those that do exist suggest that the parameter space for QD formation appears to be rather narrow. This may be because indium atoms have a large surface mobility on Sb-rich surfaces, which makes it hard to grow high-density InSb quantum dots. However, adding Ga atoms into the thin film will limit the In atom surface diffusion length, making it possible to grow high-density quantum structures. The work discussed in the previous chapter certainly lends credence to this hypothesis. For this reason, we switch to $In_xGa_{1-x}Sb$ structures instead of InSb thin insertions. So from now on, all the samples discussed in the rest of this chapter are InGaSb thin-layer samples.

6.3 Growth Temperature Study

Table 6.1 lists six samples we grew in order to study the effects of the substrate temperature on QD formation. For each sample, a 15 s anneal under Sb over-pressure was performed after each deposition. In the literature, temperatures used for the formation of In(Ga)Sb QD structures vary from 380^{o}C to 480^{o}C, while the best QD forms at relatively low temperatures. At low growth temperature, we see formation of huge clusters on our sample (figure 6.4(a)), with 150 nm diameter and 15 nm height. This sample does not have any PL emission, which we think is because the structures formed are highly

Table 6.1: Growth parameters used for substrate temperature study

Sample	Tsub (^{o}C)	P(Sb) (10^{-7} Torr)	GR (ML/s)	Ga/In ratio	Thickness (ML)
1	380	3.0	0.1	0.4/0.6	2.25
2	400	3.0	0.1	0.4/0.6	2.25
3	430	3.0	0.1	0.4/0.6	2.25
4	450	3.0	0.1	0.4/0.6	2.25
5	470	3.0	0.1	0.4/0.6	2.25
6	490	3.0	0.1	0.4/0.6	2.25

defective. As the growth temperature increases to 450 ^{o}C, smaller features start to form with an average diameter of 30 nm and height of 1.5 nm. At the highest growth temperature (490 ^{o}C), it forms uniform quantum wells as shown in figure 6.4.

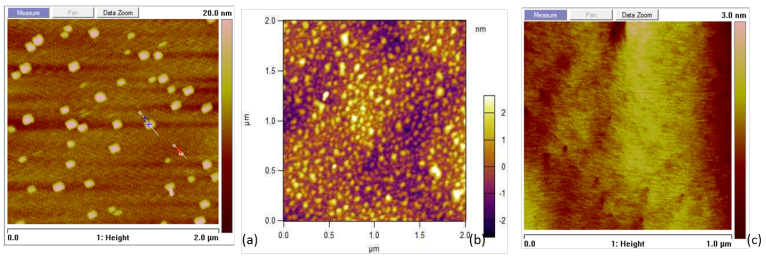

Figure 6.4: AFM scanned from the surface layer of thin InGaSb insertion grown at different substrate temperatures: (a) 380 ^{o}C, (b) 450 ^{o}C and (c) 490 ^{o}C.

The samples grown at a substrate temperature below 450^{o}C do not emit at all. Figure 6.5 shows the PL from sample 3, 4 and 5 listed in the table. From the figure, the peak intensity of the sample grown at 490 ^{o}C is 7 times the peak intensity of the sample grown at 450 ^{o}C.

Since the goal of this work is to make mid-IR emitters, the substrate temperature for thin layer deposition needs to be higher than 450^{o}C, where we start to see PL emission. In addition, the PL emission becomes stronger as the temperature increases. This gives us a low substrate temperature limit of our QD growth. On the other hand, the AFM (figure 6.3) indicates that uniform QW forms at very high growth temperature, which gives us an upper limit of the growth temperature. From the results shown above, we choose our substrate temperature window to be from 450 ^{o}C to 470 ^{o}C.

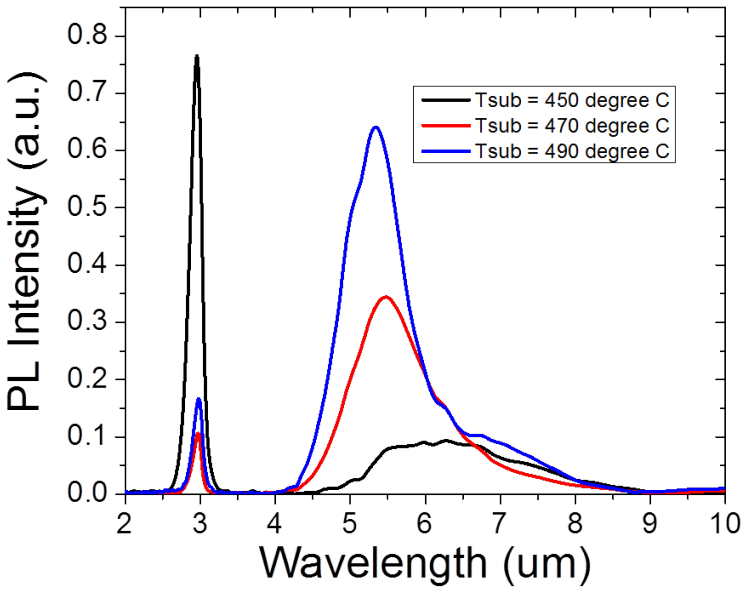

Figure 6.5: PL from three samples grown at different substrate temperatures.

6.4 Layer Thickness Study

Table 6.2 lists three samples we grew for this section. The traditional SK InAs QDs grown on GaAs begin to form after depositing 1.7 ML layer of InAs. In this study, we made an effort to understand the effect of In(Ga)Sb deposition thickness on QD formation. First, we need to know the growth

Table 6.2: Growth parameters used for layer thickness study

Sample	Tsub (^{o}C)	P(Sb) (10^{-7} Torr)	GR (ML/s)	Ga/In ratio	Thickness (ML)
1	470	2.5	0.12	0.4/0.6	1.25
2	470	2.5	0.12	0.4/0.6	1.75
3	470	2.5	0.12	0.4/0.6	2.25

rate of our material, or at least have a relative idea of how much material is deposited. The indium flux is determined by growing InAs and performing RHEED oscillation measurements during growth. The Ga flux is determined by growing GaSb at low temperature (460 ^{o}C) in an Sb-rich ambient pressure. The GaSb RHEED oscillation only shows at low temperature, while the

growth temperature of good-quality GaSb we used is 545 ^{o}C. This is because above 460 ^{o}C, GaSb is grown at step-flow mode, which is explained in Bennett and Shanabrook [91].

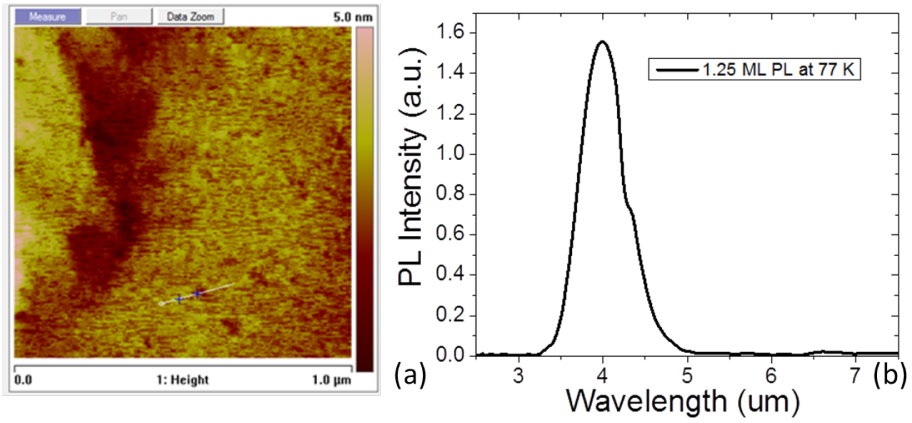

Figure 6.6: (a) AFM scanned from the surface layer of a 1.25 ML InGaSb thin layers sample (b) Low-T PL of this sample.

Figure 6.6 shows the AFM and low-T PL from the sample grown with only 1.25 ML of InGaSb. From the AFM image, this sample has a very smooth surface (surface variation is $\pm$ 2 nm). The PL peak is at 4.1 μm, which matches well with literature [92].

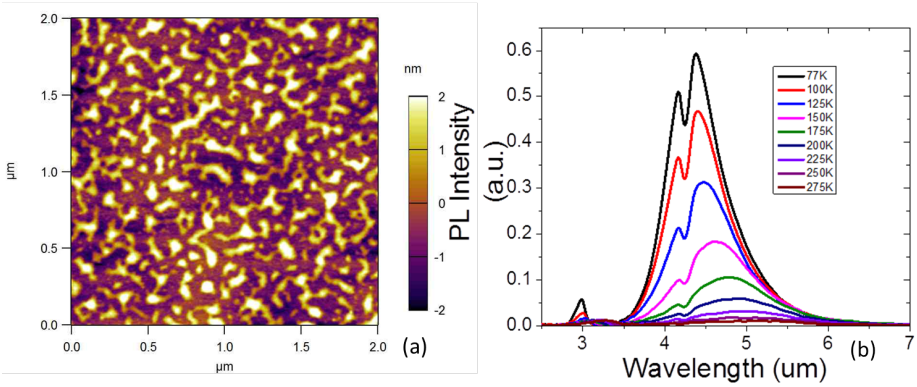

Figure 6.7: (a) AFM scanned from the surface layer of a 1.75 ML InGaSb thin layers sample. (b) T-dependent PL of this sample.

Figure 6.7 shows the AFM and T-PL of sample #2 in table 6.2. The AFM shows that there are semi-isolated features 1.7 nm high, which we think reflects the transition from 2D layer growth and 3D quantum structure

formation. At the same time, since we are not sure if we have enough material to form QDs, we also grew a sample with 2.25 ML $In_{0.6}Ga_{0.4}Sb$, with all the other parameters the same (#3 in table 6.2). From figure 6.8 (a), we can see

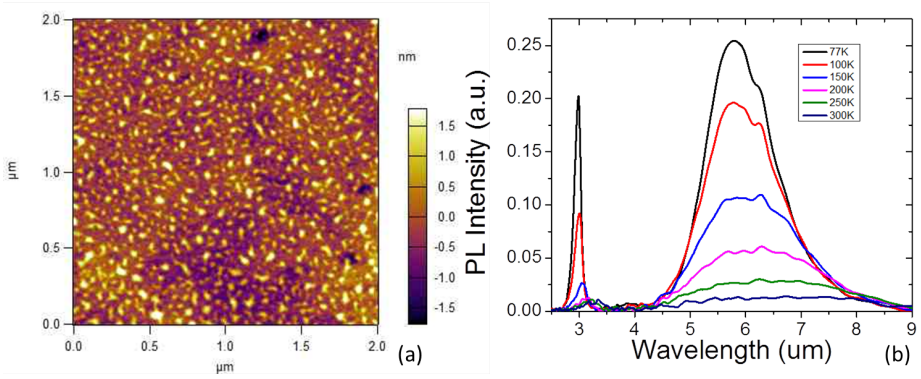

Figure 6.8: (a) AFM scanned from the surface layer of a 2.25 ML InGaSb thin layers sample. (b) T-dependent PL of this sample.

that the structures formed on the 2.25 ML sample are smaller, more isolated from each other and more like quantum dots. At first look, this might seem counterintuitive, as one would expect that the deposition of more material would lead to larger and denser QD formation. However, it is possible that the extra 0.5 ML material falls into the gap between the features shown in figure 6.7, which also gives us a smaller average height of the structures formed on the surface. From the temperature-dependent data, we can see that the sample with 2.25 ML InGaSb has better temperature performance, emitting all the way up to 300 K, while that with 1.75 ML only emits up to 275 K. This can be seen more clearly in the comparison of integrated T-PL shown in figure 6.9.

For the sample with 1.75 ML InGaSb, the integrated PL intensity at 275 K drops to 3.3% of the PL intensity at 77 K, while, for the sample with 2.25 ML InGaSb, the integrated PL intensity at 300 K only drops to 12% of that at 77 K. This indicates that the sample with more 3D-like structure formation would have better optical performance at high temperatures.

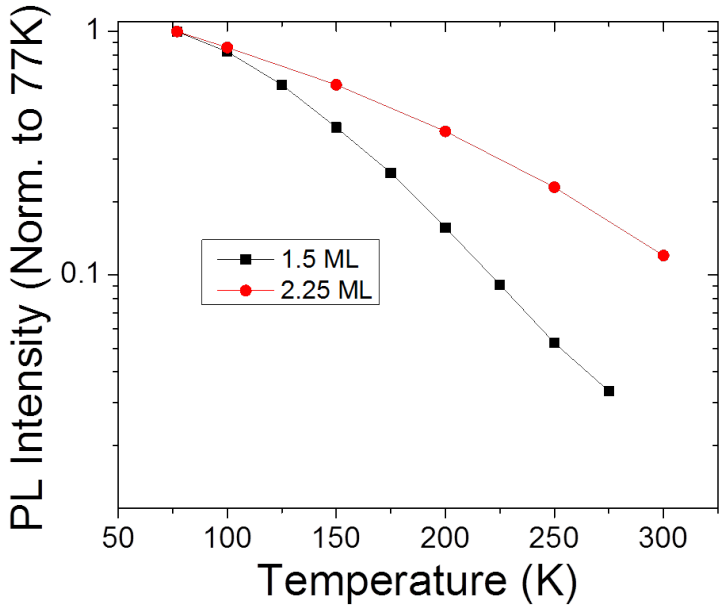

Figure 6.9: Comparison of integrated T-PL from two samples: one with 1.75 ML InGaSb and one with 2.25 ML InGaSb. All the data is normalized to its only value at 77 K.

6.5 In/Ga Ratio Study

In order to understand the effect of In/Ga ratio on 3D structure formation, we also grow another three samples containing: 1.75 ML InSb, 1.75 ML $In_{0.8}Ga_{0.2}Sb$ and 1.75 ML $In_{0.5}Ga_{0.5}Sb$. So this study contains four samples if the previously mentioned 1.75 ML $In_{0.6}Ga_{0.4}Sb$ is included. Table 6.3 shows

Table 6.3: Growth parameters used for In/Ga ratio study

Sample	Tsub (^{o}C)	P(Sb) (10^{-7} Torr)	GR (ML/s)	Ga/In ratio	Thickness (ML)
1	470	2.5	0.12	0.0/1.0	1.75
2	470	2.5	0.12	0.2/0.8	1.75
3	470	2.5	0.12	0.4/0.6	1.75
4	470	2.5	0.12	0.5/0.5	1.75

the parameters used for the samples grown. The AFMs of the surface layers are shown in figure 6.10. When there is no Ga added (figure 6.10(a)), a smooth surface is observed, which we believe will result in QW formation for

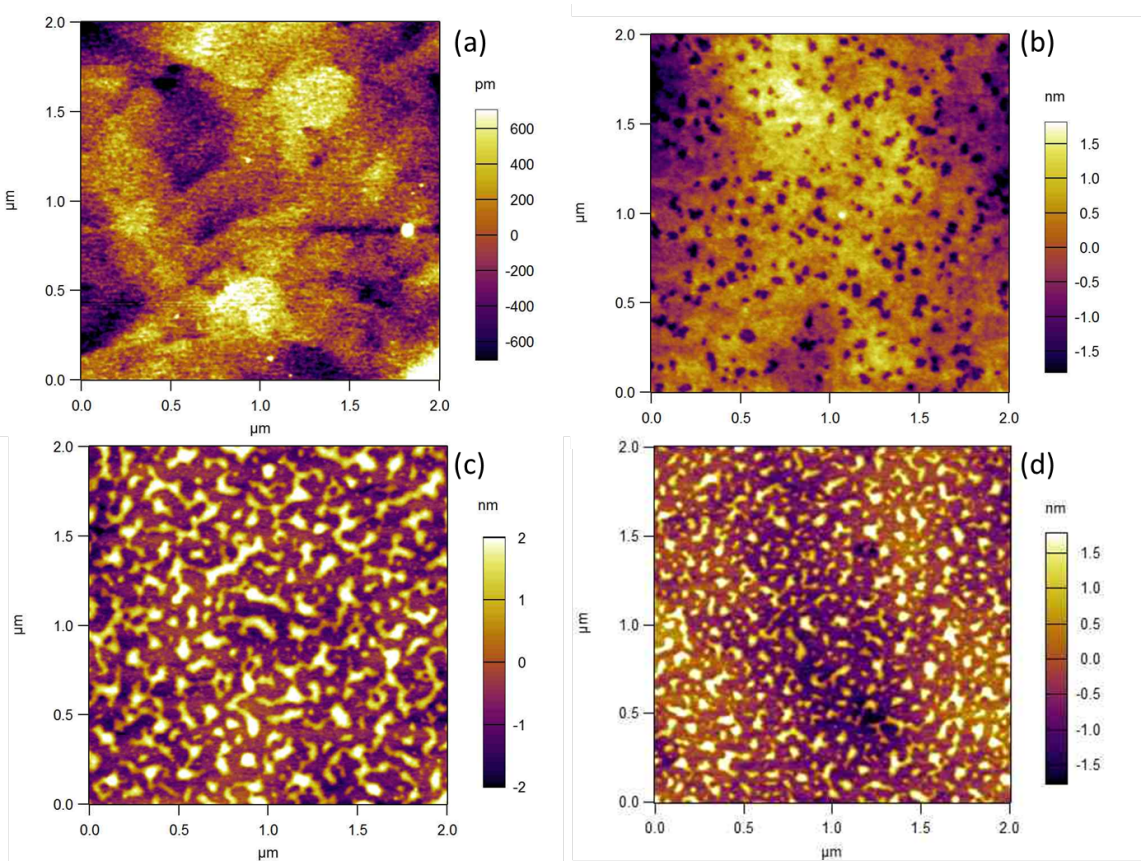

Figure 6.10: AFM of the surface layer from (a) 1.75 ML InSb (b) 1.75 ML $In_{0.8}Ga_{0.2}Sb$ (c) 1.75 ML $In_{0.6}Ga_{0.4}Sb$ (d)1.75 ML $In_{0.5}Ga_{0.5}Sb$.

the buried layers; when we add 20% Ga in the layer, the thin film starts to form nano-holes instead of a complete surface (figure 6.10 (b)); when 40% Ga is added, large islands are formed (figure 6.10 (c)); when 60% Ga is added, more isolated, smaller structures start to form (figure 6.10 (d)). This indicates that adding Ga indeed helps to reduce the surface diffusion length of In, which then helps to form 3D structures. It should be mentioned here that the continued addition of more Ga will not necessarily result in better QD formation, because it will decrease the strain in the thin layer, which is one of the most important conditions for QD formation. The structure formed in the sample containing 1.75 ML $In_{0.6}Ga_{0.4}Sb$ is higher (1.8 nm high) than the structure formed in the sample containing 1.75 ML $In_{0.5}Ga_{0.5}Sb$ (1.3 nm high), as shown in figure 6.10, meaning that as more Ga is added, more material is needed before 3D structure formation.

Integrated T-PL is shown in figure 6.11. As the Ga content increases from

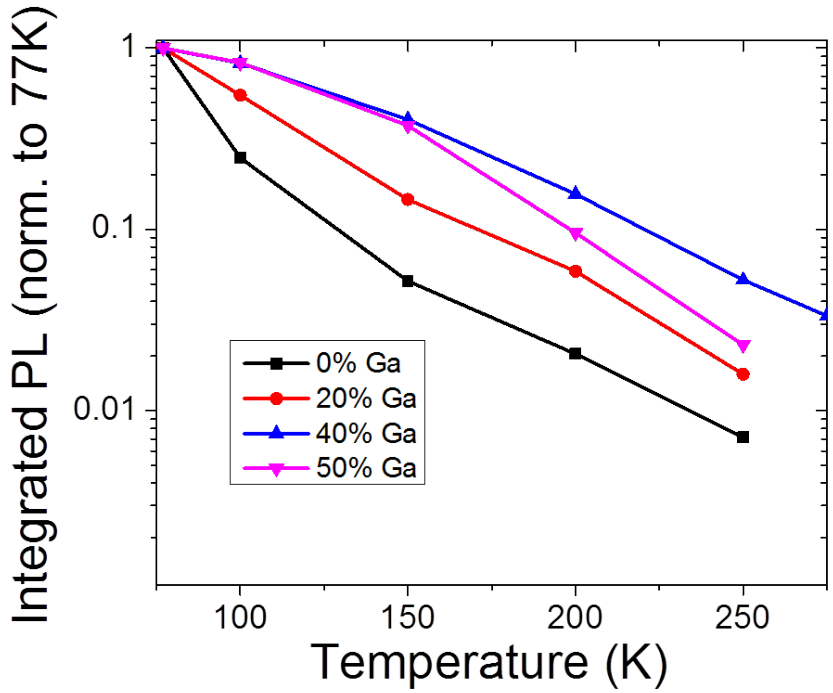

Figure 6.11: Integrated PL of four samples containing: 1.75 ML InSb (black), 1.75 ML $In_{0.8}Ga_{0.2}Sb$ (red), 1.75 ML $In_{0.6}Ga_{0.4}Sb$ (magenta), 1.75 ML $In_{0.5}Ga_{0.5}Sb$ (blue).

0% to 40%, the PL intensity decays more slowly. However, the sample with 60% Ga content has slightly worse temperature performance than that with only 40% Ga. This may be because as more Ga is added, more material is needed before quantum structure formation, so the main PL signal may be mainly from the layer under the isolated structure (a wetting layer of sorts) seen by AFM. According to both the structural image and the optical data, the best Ga composition is 30% to 40% according to our study.

6.6 Final Growth of QDs and Its Characterization

After optimizing the growth parameters, we have grown a few samples with very promising results. In this section, we talk about one sample with nicely formed QDs as an example.

The QD sample we are showing here is very interesting. As can be seen from the AFM (figure 6.12), the QDs formed on this sample have very circular

shape, which has never been demonstrated in the literature before. There are mainly two sizes of QDs formed on this sample, one with 30 ± 3 nm, diameter and 1.5 nm height, and one with 10 ± 5 nm diameter and 0.7 nm height. The growth parameters used in this sample are: Tsub = 470 ^{o}C, growth rate (GR) = 0.2 ML/s, Sb pressure = $1.5 * 10^{-7}$ Torr, thickness = 2.25 ML, In/Ga = 0.6:0.4, annealing under Sb for 15 s after thin layer deposition. The

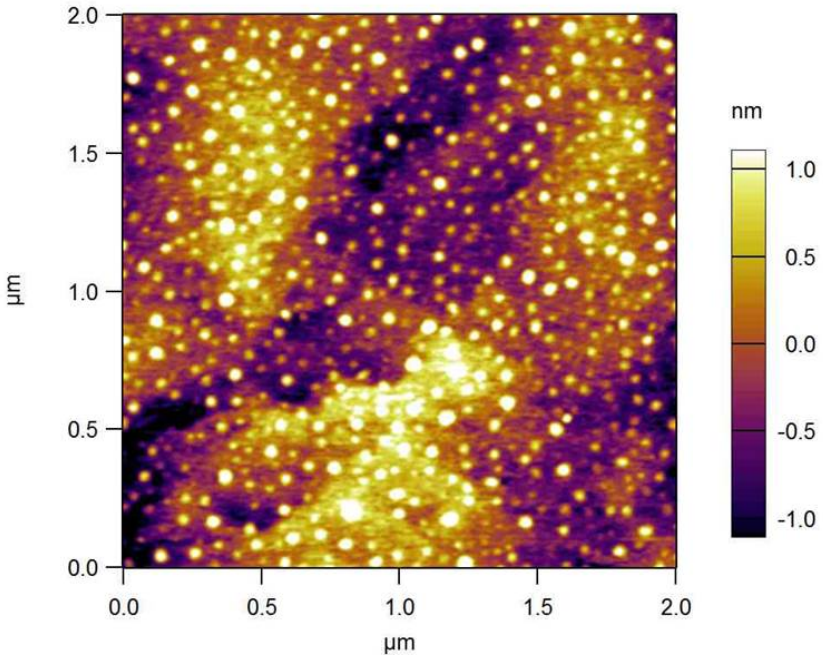

Figure 6.12: AFM of the surface layer showing clear QD formation.

T-dependent PL as well as the integrated T-PL is shown in figure 6.13. At 275 K, the integrated PL intensity drops to 19.7 %, which is better than any other samples we have so far. This indicates that the QD structure indeed has the best temperature-dependent optical performance among all the other structures.

The TRPL at low excitation at 77 K is shown in figure 6.14. The linear region shown in the figure is the low excess carrier region where SRH recombination dominates. Using the fitting method described in section 2.3, we can extract the A and B values from the TRPL data of the QD sample. Table 6.4 shows the extracted A and B value from the QD sample and the sample with obvious nano-structure formation (and better optical performance than other samples) discussed in the previous chapter. From the figure, we can see that the two samples have very similar B and C value, which are better

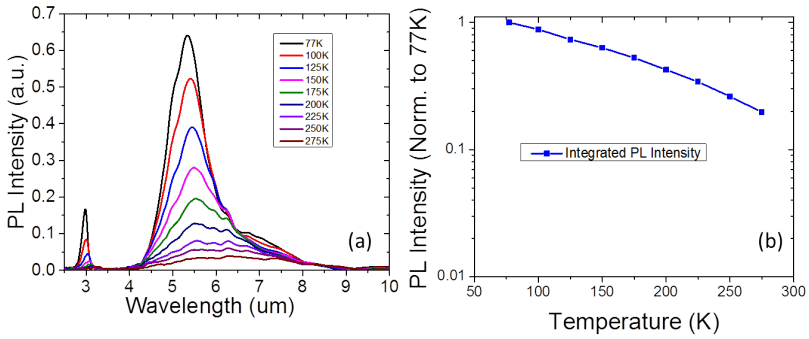

Figure 6.13: (a) T-dependent PL from QD sample, (b) Integrated T-PL from this sample.

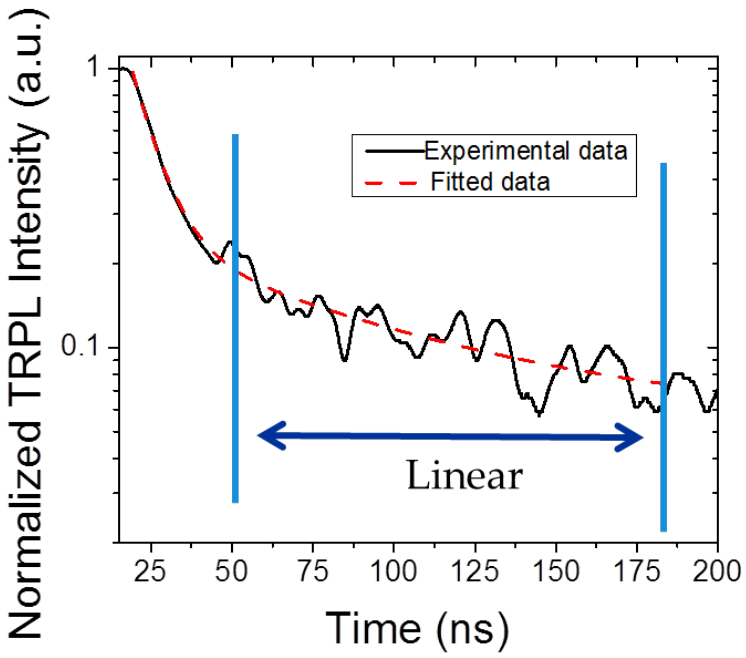

Figure 6.14: TRPL of the QD sample at 77 K with both experimental data (black solid line) and fitted data (red dash line)

than all the other samples studied in the last chapter. However, the A value of the QD sample is only half that of the sample with nano-structures. This indicates that there are less defects formed in the QD sample, which can be explained by the fact that the circular QD structure is a strain-relaxed structure which reduces the dislocation in our highly strained material system.

In this chapter, we discussed the approach to grow InGaSb QDs in an InAs matrix. We reported the growth of high-uniformity QDs with good optical performance. The quantum dots sample reported in section 6.6 has the small-

Table 6.4: Comparison of A and B values between QD sample and the sample shown nano-structure in chapter 5

Sample	A ($*10^7$/s)	B ($*10^{-9}$ cm^3/s)
InGaSb nanostructure	3.5	6.2
QD	1.9	7.5

est SRH recombination rate, largest radiative recombination rate, smallest Auger recombination rate and the best T-PL performance among all of the samples studied in this work, which makes this sample the best candidate for laser application in the future. Moreover, this is the first comprehensive study of both optical properties and carrier recombination mechanism in the InAs/In(Ga)Sb material system.

CHAPTER 7

ROOM TEMPERATURE MID-IR QUANTUM WELL LASERS ON MULTI-FUNCTIONAL METAMORPHIC BUFFERS

In the past few years, we have collaborated with Professor Minjoo Larry Lee's group at Yale on a project focusing on InAs QW emitter and laser devices grown on InAsP metamorphic buffer layers on InP substrate. My role in this project is to fabricate the emitter and laser devices and characterize the optical properties of the samples and devices. In this chapter, I am going to discuss the fabrication process of the laser device and the characterization of the laser device. Figure 7.3 and figure 7.6 are based on the figures used in our paper in the published paper [93]: Daehwan Jung, Lan Yu, Sukrith Dev, Daniel Wasserman, Minjoo Larry Lee, "Room-temperature mid-infrared quantum well lasers on multi-functional metamorphic buffers."

7.1 Introduction

Short-wavelength infrared (SWIR), referring to a wavelength range from 1.5 μm to 3.5 μm, is very important for applications such as long distance communication, gas sensing and food quality control. For those applications, low-cost and high-efficiency emitter or laser light sources are desired. However, only very limited light sources have been developed covering the wavelength range from 2 μm to 3 μm. Besides, within this wavelength range, most of the laser designs are small bandgap type-I QWs materials (GaInAsSb) using GaSb substrate due to the small lattice mismatch between the QW material and the substrate. But GaSb is not an ideal substrate material when compared with InP substrate because GaSb has lower thermal conductivity, which can be an issue for high-power laser device operation. In addition, InP substrate is widely used for telecommunication laser diodes (1.55 μm) [94], which makes it a more mature commercial processing infrastructure. So far, researchers have fabricated type-I laser diodes on InP wafer with room-

temperature operation at 2.4 μm using highly strained InAs QWs [95],[96] and InGaAs/GaAsSb type-II laser diodes on InP with RT CW operation at 2.5 μm [97]. There is still a gap for room temperature CW lasers based on InP substrates for the wavelength range from 2.5 μm to 3 μm because of the extremely high strain in the QW active region.

In the past few years, metamorphic graded buffers, for example, $In_xAl_{1-x}As$ and $InAs_xP_{1-x}$, have been studied and applied on InP substrate-based optical devices to reduce the strain effect. With the help of a graded buffer, much thicker InAs QWs can be grown on InP substrates which enables the emission wavelengths longer than 2.5 μm. In 2015, a InAs QW laser grown on $In_xAl_{1-x}As$ metamorphic buffer layers emitting at 2.9 μm has been demonstrated, lasing up to 180 K at CW mode [98]. Since it is very difficult to engineer material quality (caused by lattice mismatch), carrier confinement and the optical confinement all at the same time for this InP-based material system, there is still not a InP based, high-efficiency room-temperature laser reported covering the wavelength from 2.5 μm to 3 μm.

This chapter discusses an InAs QW laser grown on InP substrate with $InAs_xP_{1-x}$ metamorphic buffer layers lasing up to 300 K at pulsed mode and 200 K at CW mode.

7.2 Single QW Laser

The first laser diode we investigated which demonstrated lasting was a single QW laser (the structure is shown in figure 7.1). The material study of this laser device can be found in D Jung's PhD thesis [99]. This sample is fabricated into an array of 100 um x 1 mm broad-area laser bars at Yale. We tested the EL and lasing spectra in our lab. Figure 7.2 (a) shows the EL spectra below threshold current ($J = 30$ A/cm^2) and lasing spectra with 1.2 x threshold current ($J_{th} = 60$ A/cm^2). There is a significant decrease of the linewidth from spontaneous emission to stimulated emission, which is the evidence of lasing. The kink in the LI curve shown in figure 7.2 (b) at threshold current also indicates the device is lasing. However, this laser bar only works up to 90 K. A few things can be done to improve the laser performance, such as increasing the gain material by using more QWs, improving material quality by optimizing growth conditions and reducing thermal car-

rier leakage by using higher barrier material on each side of the QW. In addition, the optical confinement factor, which is defined as the fraction of power guided in the waveguide [100], in this QW laser is only 0.62%. This can be improved by introducing more QWs in the active region. The next section discusses a multiple QW (MQW) laser device with increased gain and optical confinement factor.

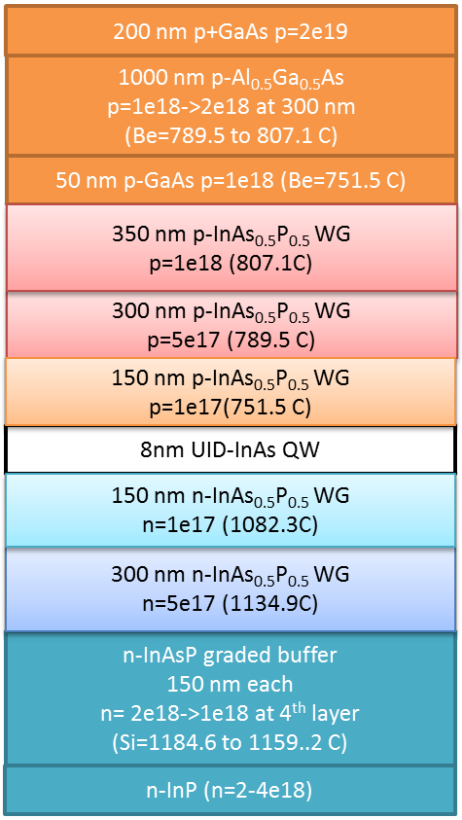

Figure 7.1: Structure of the first laser diode that actually lases.

7.3 Multiple QW Laser Device

The biggest challenge for MQW laser growth is increased strain in the MQW region, which will increase the number of dislocations and affect the laser performance. In our active regions, a strain balanced InAsP barrier is used to compensate the strain induced by MQWs. Three samples are studied to prove the effectiveness of the strain-balanced structure: a single QW sample, a 4 QW sample without strain-balancing, and a 4 QW sample with strain-

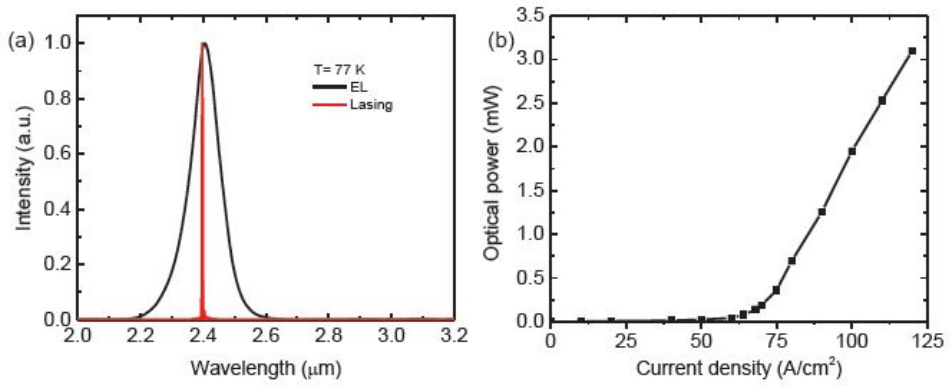

Figure 7.2: (a) Normalized EL and lasing spectra of the single QW laser device at 77 K. (b) L-I curve of this device at 77 K, cw mode.

balanced barrier. The low T PL from all three of these samples is illustrated in figure 7.3, and indicates that the sample with strain balanced structure has the best PL intensity under the same excitation conditions. The PL intensity of the four QW sample without strain-balancing is even worse than that of the single QW sample. This is because high strain in the MQW region results in a higher density of dislocations, which can serve as non-radioactive recombination centers, and will thus negatively affect the emission efficiency of the material (figure 7.3 (b)).

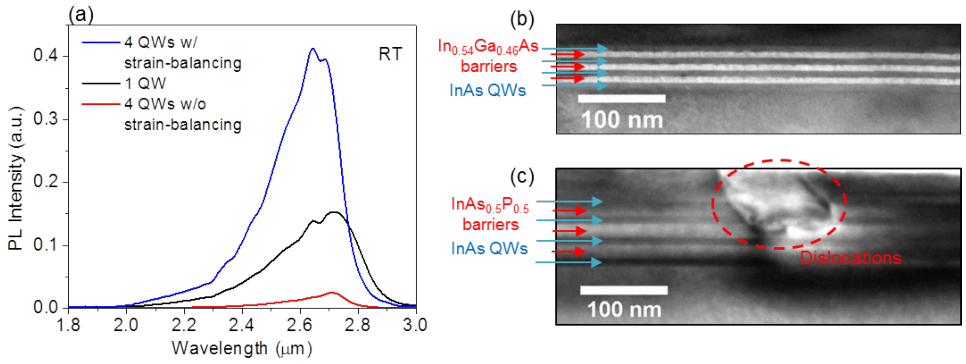

Figure 7.3: (a) RT PL spectra from 4 QW sample with strain-balancing (blue), 1 QW sample (black), and 4 QW sample without strain-balancing (red). (b) Bright-field TEM image on 4 QW sample with strain-balancing, and (c) without strain-balancing.

After demonstrating that the strain-balanced structure indeed helps to improve the material quality as well as the optical property of the emitter, our collaborators at Yale grew a nine-QW laser structure on metamorphic graded

buffers. Our laser diodes were grown on (001) n-type InP in a Veeco Mod Gen-II molecular beam epitaxy chamber. The laser diodes were fabricated using a multi-step process. Figure 7.4 is a simplified flow chart showing the laser fabrication process. We first deposited a layer of SiO_2 (200 nm thick) on the as-grown wafer, followed by UV lithography to define the SiO_2 etch mask. The SiO_2 etch mask was then etched using freon reactive ion etching (RIE), and a second dry etch using inductively coupled plasma (ICP)-RIE, with the SiO_2 as an etch mask, was used to define the laser ridge (the laser presented in this work has a ridge width of 10 μm). The remaining SiO_2 was then removed by buffered oxide etching (BOE). We subsequently deposited a 300 nm SiO_2 isolation layer, and used UV lithography in order to define a 6 μm wide opening on the 10 μm wide waveguide. The opening in the SiO_2 was made with Freon RIE. We then used UV lithography to define 300 μm wide contact pads covering the opening on the waveguide. Finally, a Ti/Pt/Au (20 nm : 20 nm : 250 nm) was evaporated as p-contact to the top of the wafer. Cross-sectional SEM was taken of a 10 μm laser bar after top metal deposition (shown in figure 7.5). The samples were then lapped to a thickness of 150-200 μm, and a Ge/Au/Ni/Au (27 nm : 55 nm : 22 nm : 300 nm) n-contact layer was evaporated on the back side of the sample. After metal deposition, the sample was annealed at 405 ^{o}C for 5 minutes to alloy the metal. Then the fabricated sample was cleaved into 1 mm long laser bars and mounted on a copper block with In paste. Copper blocks were mounted in a continuous flow cryostat.

Emission spectra were measured using a Bruker v80v Fourier transform infrared spectroscopy (FTIR) emission spectrometer. EL spectra were measured using amplitude step-scan FTIR spectroscopy. Laser emission was measured using rapid scan FTIR spectroscopy, with the background blackbody spectrum (background emission collected with the laser off) subtracted from the rapid scan spectra. For the LI curves, single facet laser output was collimated using a 2 inch diameter Ge lens and focused onto a liquid nitrogen cooled InSb detector using a parabolic mirror with a 2 inch diameter and 4 inch focal length. Our InSb detector was calibrated to a thermal power meter, and the detector response was measured to be linear over the output powers observed from our laser devices.

Light output power versus current density (LI) curves are presented in figure 7.6(a) and 7.6(b) for pulsed and CW operation, respectively. The LI

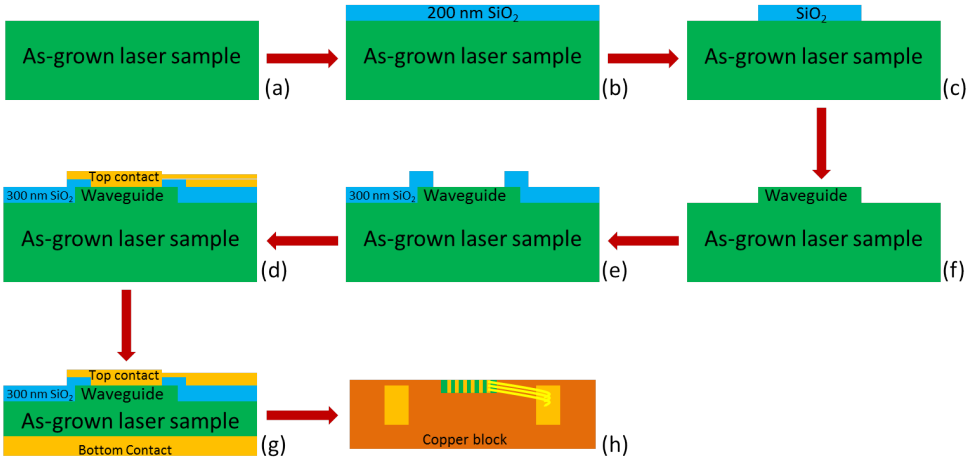

Figure 7.4: Laser fabrication process: (a) As-grown sample. (b) Deposit 200 nm SiO_2. (c) After first lithography, SiO_2 is reshaped into 10 μm wide etch mask. (d) Waveguide defined by dry etching. (e) Define a opening on top of the waveguide for metal contact. (f) Evaporation of top metal contact. (g) Thin down sample to 150 μm and evaporate bottom metal contact. (h) Cleave lasers into 1 mm-long bars and mount on copper block, then wire bond lasers to Au-coated ceramic stand-offs for mounting into cryostat.

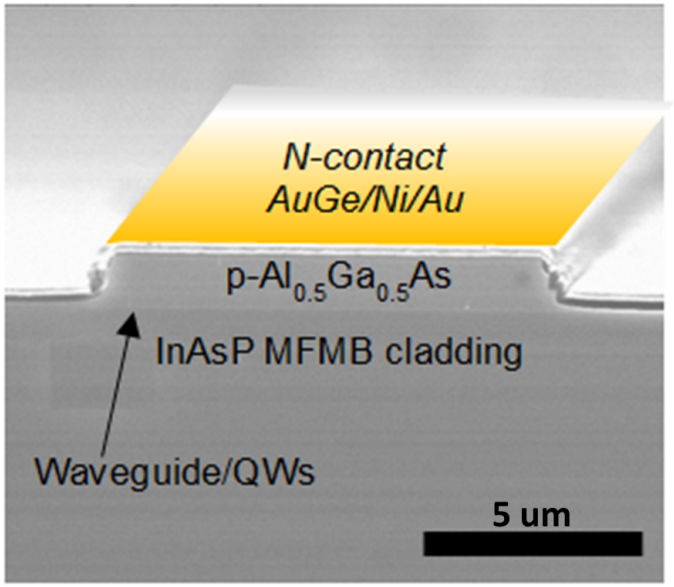

Figure 7.5: Cross section SEM taken after the top contact deposition.

curves show a clear slope change, indicative of lasing threshold, up to 300 K in pulsed mode operation and 200 K in CW operation. Figure 7.6(c) shows the normalized temperature-dependent emission spectra from our laser, operated in pulsed mode (200 ns pulses, 50 kHz repetition rate) with current

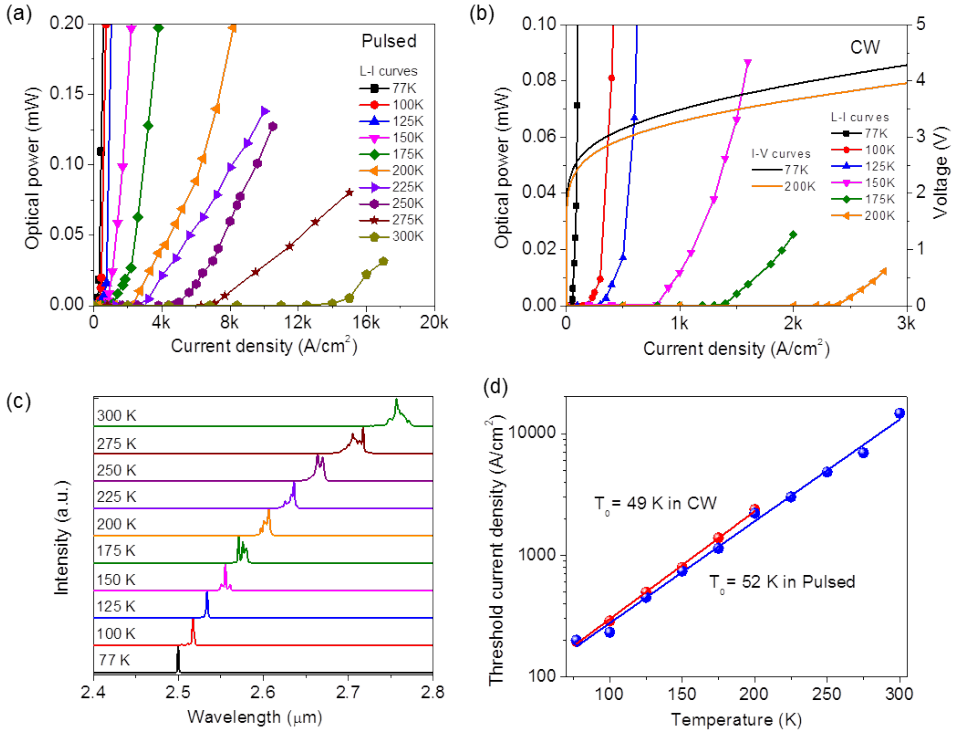

Figure 7.6: Temperature-dependent laser characterizations. (a) Temperature-dependent pulsed mode LI curves. (b) CW mode LIV curves. (c) Pulsed mode lasing spectra. (d) Threshold current density versus temperature plots in CW (red) and pulsed mode (blue). Solid line is a semi-log fit.

pulse amplitude of I $1.2 * I_{th}$. The spectra show the expected red-shift of the lasing wavelength as the heat sink temperature is increased to 300 K, commensurate with the change in bandgap of the InAs QWs. The threshold current density (both pulsed and CW) increases exponentially with temperature (figure 7.6(d)), and the characteristic temperature (T_0) extracted is 52 K for pulsed operation and 49 K for CW operation. The threshold current density of the laser at cw operation mode is only slightly higher than that of pulsed mode, meaning that the device has good heat conductivity. In this collaborative effort, we demonstrated room temperature pulsed emission from InAs QW lasers grown on InP substrates using multi-functional metamorphic buffer layers. The ability to grown SWIR lasers on the technologically mature InP material system offers a potential SWIR coherent source compatible with standard optoelectronic processing techniques. We demonstrate pulsed laser operation up to 300K and CW operation up to 200K. Though

our laser efficiency decreases with increasing temperature (with threshold current densities as high as $J_{th} = 1400$ A/cm^2 for pulsed mode operation at RT), there are potential improvements to both the design and fabrication which could result in significantly improved performance. In addition, it can be observed that our devices show an unusually high turn on voltage, given the bandgap of the diode materials suggesting a significant voltage drop our side of the pn-junction. This could be a result of poor contact resistance, or alternatively, series resistance in our cladding layers. In either case, improved transport in our laser devices could significantly reduce ohmic heating and could result in improved device performance. Thus, not only do our devices already demonstrate room temperature pulsed operation, but with improvements in device design, growth, and fabrication, improved laser efficiency and RT CW performance are certainly achievable.

CHAPTER 8

CONCLUSION AND FUTURE WORK

This thesis presents the study of semiconductor quantum structures for mid-IR light emission. In the first part of the thesis, nanosphere lithography-defined QDs are fabricated and characterized. Optically active nano-pillars with diameters as small as 90 nm are fabricated, and narrow linewidth (18 meV) electroluminescence from a fabricated diode structure is observed, with an emission blue-shift of over 37 meV from the original quantum well sample luminescence. The results presented offer the potential for low-cost, large-area patterning of quantum nanostructures for optoelectronic applications. In the future, smaller NS (less than 100 nm diameter) with good size uniformity can potentially be used as QCL active regions for intersubband based QD mid-IR emitters or lasers. In the second part of the thesis, I demonstrated control of the ground state energies in submonolayer InAs quantum dot structures. In this work, I was able to control the QD ground state energy of the SML QD structures across a 500 meV range (from 1.38 eV to 1.88 eV), providing a possible way to make QDCL using the submonolayer QDs. In the future, more study is needed in order to grow high-density and high-uniformity SML QD for QCL applications.

In the third part of this thesis, emission from type-II thin deposited In(Ga)Sb in InAs matrix is studied and mid-IR emission across the 3-8 μm wavelength range is demonstrated. This material system offers strong potential for low-cost mid-IR emitter development. However, the type-II emitters in narrow bandgap semiconductors are known to suffer from strong Auger recombination, limiting their effectiveness as efficient mid-IR sources. For this reason, I developed a time-resolved mid-IR PL system to study the carrier dynamics in the type-II mid-IR emitter devices. In the future, more research is needed to integrate the type-II QDs into an emitter structure. Furthermore, the efficiency of this emitter system needs to be studied in order to make low-cost and high-efficiency mid-IR emitters.

In the final section of my thesis, an InAs QW laser grown on InP with the help of an InAsP metamorphic buffer layer is fabricated and characterized. This laser gives promising results as it operates from 77 K up to 300 K in pulsed mode operation, and up to 200 K in CW operation. The performance of these lasers is characterized, as well as their limitations. I discuss potential routes towards improved laser performance. In total, this thesis investigates a range of paths towards mid-IR lasers and LEDs. In particular, I discuss the growth and fabrication of semiconductor quantum dots (both self-assembled and top-down fabricated) for potential integration in to quantum dot cascade lasers. In addition, I discuss the growth and characterization of a novel type of mid-IR emitter based on type-II quantum structures in the InAs/In(Ga)Sb material system. Finally, I present collaborative work demonstrating room temperature lasting from InAs QWs grown on InP substrates with multi-functional metamorphic buffer layers. The results presented here offer a number of potential routes towards next-generation mid-IR sources.. In the future, a few things can be done in terms of laser fabrication to improve the laser performance. For example, an anti-reflection coated facet can be introduced to improve the laser output power, and a distributed feedback grating can be fabricated on top of the waveguide for single-mode operation.

REFERENCES

[1] R. Martini, C. Gmachl, R. Paiella, F. Capasso, E. Whittaker, H. Liu, H. Hwang, D.L.Sivco, J. Baillargeon, and A. Cho, "High-speed digital data transmission using mid-infrared quantum cascade lasers," *Electron. Lett.*, vol. 37, pp. 1290–1291, 2001.

[2] "The correct material for infrared applications (edmund optics)," 2008. [Online]. Available: http://www.edmundoptics.eu/

[3] M. Chaplin, "Water structure and science," 2016. [Online]. Available: http://www1.lsbu.ac.uk/water/

[4] W. Chen, K. Long, M. Lu, V. Chaudhery, H. Yu, J. Choi, J. Polans, Y. Zhuo, B. A. Harley, and B. T. Cunningham, "Photonic crystal enhanced microscopy for imaging of live cell adhesion," *Analyst*, vol. 138, 2013.

[5] E. P. A. spectral database, "Molecular absorption data," 1999. [Online]. Available: http://www.epa.gov/ttnemc01/ftir/data.html

[6] "Introduction to Fourier Transform Infrared Spectrometry (thermal nicolet corporation)." [Online]. Available: http://www.niu.edu/analyticallab/_pdf/ftir/FTIRintro.pdf

[7] J. Keller, "Raytheon to develop advanced ir focal plane arrays for army night vision," 2014. [Online]. Available: http://www.militaryaerospace.com/articles/print/volume-25/issue-3/eo-watch/raytheon-to-develop-advanced-ir-focal-plane-arrays-for-army-night-vision.html

[8] D. Pham, "Inhabitats green home expert series," 2011. [Online]. Available: http://inhabitat.com/inhabitats-green-home-expert-series-launches-next-week/

[9] J. Faist, F. Capasso, D. L. Sivco, C. Sirtori, A. L. Hutchinson, and A. Y. Cho, "Quantum cascade laser," *Science*, vol. 264, no. 5158, pp. 553–556, 1994.

[10] P. Q. Liu, A. J. Hoffman, M. D. Escarra, K. J. Franz, J. B. Khurgin, Y. Dikmelik, X. Wang, J.-Y. Fan, and C. F. Gmachl, "Highly power-efficient quantum cascade lasers," *Nature Photonics*, vol. 4, pp. 95–98, 2010.

[11] M. Beck, D. Hofstetter, T. Aellen, J. Faist, U. Oesterle, M. Ilegems, E. Gini, and H. Melchior, "Continuous wave operation of a mid-infrared semiconductor laser at room temperature," *Science*, vol. 295, no. 301, 2002.

[12] C. A. Wang, A. Goyal, R. Huang, J. Donnelly, D. Calawa, G. Turner, A. Sanchez-Rubio, A. Hsu, Q. Hu, and B. Williams, "Strain-compensated GaInAs/AlInAs/InP quantum cascade laser materials," *Journal of Crystal Growth*, vol. 312, pp. 1157–1164, 2010.

[13] A. Lyakh, R. Maulini, A. Tsekoun, R. Go, S. Von der Porten, C. Pflgl, L. Diehl, F. Capasso, and C. K. N. Patel, "High-performance continuous-wave room temperature 4.0-μm quantum cascade lasers with single-facet optical emission exceeding 2 w," *Proceedings of the National Academy of Sciences*, vol. 107, no. 44, pp. 18 799–18 802, 2010.

[14] "Quantum-cascade lasers: QCLs enable applications in IR spectroscopy (laser focus world)," 2015. [Online]. Available: http://www.laserfocusworld.com/articles/print/volume-49/issue-01/features/quantum-cascade-lasers–qcls-enable-applications-in-ir-spectrosc.html

[15] A. Lyakh, C. Pflugl, L. Deihl, Q. Wang, F. Capasso, X. Wang, J. Fan, T. Tanbun-Ek, R. Maulini, A. Tsekoun, R. Go, and C. Patel, "1.6 W high wall plug efficiency, continuous wave room temperature quantum cascade laser emitting at 4.6 μm," *Appl. Phys. Lett.*, vol. 92, no. 111110, 2008.

[16] Y. Bai, S. Darvish, S. Slivken, W. Zhang, A. Evans, J. Nguyen, and M. Razeghi, "Room temperature continuous wave operation of quantum cascade lasers with watt-level optical power," *Appl. Phys. Lett.*, vol. 92, no. 101105, 2008.

[17] Y. Bai, S. Slivken, S. Kuboya, S. Darvish, and M. Razeghi, "Quantum cascade lasers that emit more light than heat," *Nature Photon*, vol. 4, no. 99, 2010.

[18] B. G. Lee, M. A. Belkin, and F. Capasso, "Array of tiny quantum cascade lasers provides tunable mid-ir output," 2008. [Online]. Available: http://www.photonics.com/Article.aspx?AID=33534

[19] G. Sun, *The Intersubband Approach to Si-based Lasers*. InTech, 2010.

[20] C. Gmachl, H. M. Ng, and A. Y. Cho, "Intersubband absorption in GaN/AlGaN multiple quantum wells in the wavelength range of lambda 1.75-4.2 um," *Applied Physics Letters*, vol. 7, no. 3, pp. 334–336, 2000.

[21] P. Crump, J. Wang, T. Crum, S. Zhang, M. Grimshaw, W. Dong, M. DeFranza, S. Das, M. DeVito, and J. Farmer, "Optimized performance GaAs-based diode lasers: Reliable 800 nm 125 W bars and 83.5 percent efficient 975 nm single emitters," *SSDLTR*, 2005.

[22] R. Yang, "Infrared laser based on intersubband transitions in quantum wells," *Superlatt. Microstruct*, vol. 17, pp. 77–83, 1995.

[23] I. Vurgaftman, J. R. Meyer, and L. R. Ram-Mohan, "Mid-ir vertical-cavity surface-emitting lasers," *IEEE J. Quantum Electron*, vol. 34, pp. 147–156, 1997.

[24] M. Kim, C. Canedy, W. Bewley, C. Kim, J. Lindle, J. Abell, I. Vurgaftman, and M. J. R, "Interband cascade laser emitting at $\lambda = 3.75$ μm in continuous wave above room temperature," *Appl. Phys. Lett*, vol. 92, no. 191110, 2008.

[25] I. Vurgaftman, R. Weih, M. Kamp, J. R. Meyer, C. L. Canedy, C. S. Kim, M. Kim, W. W. Bewley, C. D. Merritt, J. Abell, and S. Hofling, "Interband cascade lasers," *J. Phys. D: Appl. Phys*, vol. 48, no. 123001, 2015.

[26] W. Bewley, J. Lindle, C. Canedy, M. Kim, C. Kim, D. Larrabee, I. Vurgaftman, and M. J. R, "Gain, loss, and internal efficiency in interband cascade lasers emitting at $\lambda = 3.6$-4.1 μm," *J. Appl. Phys*, vol. 103, no. 013114, 2008.

[27] G. Belenky, "Type-i diode lasers for spectral region above 3 μm," *IEEE Journal of Selected Topics in Quantum Electronics*, vol. 17, no. 5, 2011.

[28] I. Vurgaftman, J. R. Meyer, and L. R. Ram-Mohan, "Band parameters for iii-v compound semiconductors and their alloys," *Journal of Applied Physics*, vol. 89, 2001.

[29] G. P. Donati, R. Kaspi, and K. J. Malloy, "Interpolating semiconductor alloy parameters: Application to quaternary III-V band gaps," *J. Appl. Phys*, vol. 94, p. 58145819, 2003.

[30] J. Chen, D. Donetsky, L. Shterengas, M. Kisin, G. Kipshidze, and G. Belenky, "Effect of quantum well compressive strain above 1% on differential gain and threshold current density in type-I gasb-based diode lasers," *IEEE Journal of Quantum Electron*, vol. 44, 2008.

[31] T. Hosoda, G. Kipshidze, L. Shterengas, and G. Belenky, "200 mw type-i gasb-based laser diodes operating at 3 μm: Role of waveguide width," *Applied Physics Letters*, vol. 94, 2009.

[32] S. Seki, T. Yamanaka, W. Lui, and K. Yokoyama, "Theoretical analysis of differential gain of 1.55 μm InGaAsP/InP compressive-strained multiplequantum- well lasers," *J. Appl. Phys*, vol. 75, p. 12991303, 1994.

[33] I. Vurgaftman, J. R. Meyer, and L. R. Ram-Mohan, "Band parameters for iii-v compound semiconductors and their alloys," *J. Appl. Phys*, vol. 89, p. 58155875, 2001.

[34] T. Hosoda, G. Kipshidze, G. Tsvid, L. Shterengas, and G. Belenky, "Type-i GaSb-based laser diodes operating in 3.1- to 3.3-μm wavelength range," *IEEE Photon. Technol. Lett*, vol. 22, p. 718 to 720, 2010.

[35] D. Arsenijevic, C. Liu, A. Payusov, M. Stubenrauch, and D. Bimberg, "Temperature-dependent characteristics of single-mode InAs submonolayer quantum-dot lasers," *IEEE Photon. Technol. Lett*, vol. 24, no. 11, 2012.

[36] A. Y. Liu, C. Zhang, J. Norman, A. Snyder, D. Lubyshev, J. M. Fastenau, A. W. K. Liu, A. C. Gossard, and J. E. Bowers, "High performance continuous wave 1.3 μm quantum dot lasers on silicon," *Applied Physics Letters*, vol. 104, no. 041104, 2014.

[37] J.-Y. Marzin, J.-M. Gérard, A. Izrael, D. Barrier, and G. Bastard, "Photoluminescence of single InAs quantum dots obtained by self-organized growth on GaAs," *Physical Review Letters*, vol. 73, no. 5, p. 716, 1994.

[38] N.-M. Park, C.-J. Choi, T.-Y. Seong, and S.-J. Park, "Quantum confinement in amorphous silicon quantum dots embedded in silicon nitride," *Physical Review Letters*, vol. 86, no. 7, p. 1355, 2001.

[39] J. R. Heath, J. Shiang, and A. Alivisatos, "Germanium quantum dots: Optical properties and synthesis," *The Journal of Chemical Physics*, vol. 101, no. 2, pp. 1607–1615, 1994.

[40] Y. Chen and Z. Rosenzweig, "Luminescent CdS quantum dots as selective ion probes," *Analytical Chemistry*, vol. 74, no. 19, pp. 5132–5138, 2002.

[41] B. L. Wehrenberg, C. Wang, and P. Guyot-Sionnest, "Interband and intraband optical studies of PbSe colloidal quantum dots," *The Journal of Physical Chemistry B*, vol. 106, no. 41, pp. 10 634–10 640, 2002.

[42] K. Arshak and M. Mihov, "State-of-the-art of focused ion beam nanolithography," *J Optoelectron Adv Mater*, vol. 7, pp. 193–198, 2005.

[43] P. Atkinson, M. B. Ward, S. P. Bremner, D. Anderson, T. Farrow, G. A. C. Jones, A. J. Shields, and D. A. Ritchie, "Site-control of InAs quantum dots using ex-situ electron-beam lithographic patterning of GaAs substrates," *Japanese Journal of Applied Physics*, vol. 45, p. 2519, 2006.

[44] D. Leonard, M. Krishnamurthy, C. M. Reaves, S. P. Denbaars, and P. M. Petroff, "Direct formation of quantum-sized dots from uniform coherent islands of InGaAs on GaAs surfaces," *Applied Physics Letters*, vol. 63, no. 23, pp. 3203–3205, 1993.

[45] J. Christen, M. Krahl, and D. Bimberg, "Visualization of the transition from 2D to 3D and from non-k-conservation to k-conservation in the lineshapes of quantum wells and true superlattices," *Superlattices and Microstructures*, vol. 7, no. 1, 1990.

[46] M. Imada, S. Noda, A. Chutinan, T. Tokuda, M. Murata, and G. Sasaki, "Coherent two-dimensional lasing action in surface-emitting laser with triangular-lattice photonic crystal structure," *Applied Physics Letters*, vol. 75, no. 3, pp. 316–318, 1999.

[47] S. Law, L. Yu, and D. W. A. Rosenberg, "All-semiconductor plasmonic nanoantennas for infrared sensing," *Nano letters*, vol. 13, 2013.

[48] M. Qi and H. I. Smith, "Achieving nanometer-scale, controllable pattern shifts in x-ray lithography using an assembly-tilting technique," *Journal of Vacuum Science and Technology: B*, vol. 20, no. 6, pp. 2991–2994, 2002.

[49] X. Qian, J. Li, D. Wasserman, and W. D. Goodhue, "Uniform InGaAs quantum dot arrays fabricated using nanosphere lithography," *Applied Physics Letters*, vol. 93, no. 23, 2008.

[50] H. W. Deckman and J. H. Dunsmuir, "Natural lithography," *Applied Physics Letters*, vol. 41, no. 4, pp. 377–379, 1982.

[51] N. Vogel, S. Goerres, K. Landfester, and C. K. Weiss, "A convenient method to produce close- and non-close-packed monolayers using direct assembly at the air water interface and subsequent plasma-induced size reduction," *Macromolecular Chemistry and Physics*, vol. 212, no. 16, pp. 1719–1734, 2011.

[52] X. Qian, S. Vangala, D. Wasserman, and W. D. Goodhue, "High-optical-quality nanosphere lithographically formed ingaas quantum dots using molecular beam epitaxy assisted gaas mass transport and overgrowth," *Journal of Vacuum Science and Technology B*, vol. 28, no. 3, 2010.

[53] H. Lee, W. Yang, and P. C. Sercel, "Temperature and excitation dependence of photoluminescence line shapein InAs/GaAs quantum-dot structures," *Phys. Rev. B*, vol. 55, pp. 9757–9762, 1997.

[54] D. L. Huffaker, G. Park, Z. Zou, O. B. Shchekin, and D. G. Deppe, "1.3 μm room-temperature GaAs-based quantum-dot laser," *Applied Physics Letters*, vol. 73, no. 18, pp. 2564–2566, 1998.

[55] C. Reese, C. Becher, A. Imamolu, E. Hu, B. D. Gerardot, and P. M. Petroff, "Photonic crystal microcavities with self-assembled InAs quantum dots as active emitters," *Applied Physics Letters*, vol. 78, no. 16, pp. 2279–2281, 2001.

[56] Y. Nakata, K. Mukai, M. Sugawara, K. Ohtsubo, H. Ishikawa, and N. Yokoyama, "Molecular beam epitaxial growth of InAs self-assembled quantum dots with light-emission at 1.3 μm," *Journal of Crystal Growth*, vol. 208, no. 14, pp. 93 – 99, 2000.

[57] K. Eberl, M. Lipinski, Y. Manz, W. Winter, N. Jin-Phillipp, and O. Schmidt, "Self-assembling quantum dots for optoelectronic devices on Si and GaAs," *Physica E: Low-dimensional Systems and Nanostructures*, vol. 9, no. 1, pp. 164 – 174, 2001.

[58] J. M. Moison, F. Houzay, F. Barthe, L. Leprince, E. Andr, and O. Vatel, "Self organized growth of regular nanometer scale InAs dots on GaAs," *Applied Physics Letters*, vol. 64, no. 2, pp. 196–198, 1994.

[59] S. Guha, A. Madhukar, and K. C. Rajkumar, "Onset of incoherency and defect introduction in the initial stages of molecular beam epitaxical growth of highly strained InxGa1xAs on GaAs(100)," *Applied Physics Letters*, vol. 57, no. 20, pp. 2110–2112, 1990.

[60] D. Leonard, M. Krishnamurthy, C. M. Reaves, S. P. Denbaars, and P. M. Petroff, "Direct formation of quantumsized dots from uniform coherent islands of InGaAs on GaAs surfaces," *Applied Physics Letters*, vol. 63, no. 23, pp. 3203–3205, 1993.

[61] D. J. Eaglesham and M. Cerullo, "Dislocation-free stranski-krastanow growth of Ge on Si(100)," *Phys. Rev. Lett.*, vol. 64, pp. 1943–1946, 1990.

[62] H. Lee, W. Yang, and P. C. Sercel, "Temperature and excitation dependence of photoluminescence line shape in InAs/GaAs quantum-dot structures," *Phys. Rev. B*, vol. 55, pp. 9757–9762, 1997.

[63] N. Ledentsov, D. Bimberg, F. Hopfer, A. Mutig, V. Shchukin, A. Savel'ev, G. Fiol, E. Stock, H. Eisele, M. Dähne, D. Gerthsen, U. Fischer, D. Litvinov, A. Rosenauer, S. Mikhrin, A. Kovsh, N. Zakharov, and P. Werner, "Submonolayer quantum dots for high speed surface emitting lasers," *Nanoscale Research Letters*, vol. 2, no. 9, p. 417, 2007.

[64] N. N. Ledentsov, A. F. Tsatsulnikov, A. Y. Egorov, P. S. Kopev, A. R. Kovsh, M. V. Maximov, V. M. Ustinov, B. V. Volovik, A. E. Zhukov, Z. I. Alferov, I. L. Krestnikov, D. Bimberg, and A. Hoffmann, "Intrinsic optical confinement and lasing in InAsAlGaAs submonolayer superlattices," *Applied Physics Letters*, vol. 74, no. 2, pp. 161–163, 1999.

[65] Z. Xu, D. Birkedal, J. M. Hvam, Z. Zhao, Y. Liu, K. Yang, A. Kanjilal, and J. Sadowski, "Structure and optical anisotropy of vertically correlated submonolayer InAs/GaAs quantum dots," *Applied Physics Letters*, vol. 82, no. 22, pp. 3859–3861, 2003.

[66] L. Yu, D. Jung, S. Law, J. Shen, J. J. Cha, M. L. Lee, and D. Wasserman, "Controlling quantum dot energies using submonolayer bandstructure engineering," *Applied Physics Letters*, vol. 105, no. 8, 2014.

[67] V. Bressler-Hill, A. Lorke, S. Varma, P. M. Petroff, K. Pond, and W. H. Weinberg, "Initial stages of InAs epitaxy on vicinal GaAs(001)," *Phys. Rev. B*, vol. 50, pp. 8479–8487, 1994.

[68] A. Lenz, H. Eisele, J. Becker, J. Schulze, T. Germann, F. Luckert, K. Potschke, E. Lenz, L. Ivanova, A. Strittmatter, D. Bimberg, U. Pohl, and M. Dahne, "Atomic structure and optical properties of InAs submonolayer depositions in GaAs," *Journal of Vacuum Science and Technology B*, vol. 29, no. 4, 2011.

[69] T. Kita, N. Tamura, O. Wada, M. Sugawara, Y. Nakata, H. Ebe, and Y. Arakawa, "Artificial control of optical gain polarization by stacking quantum dot layers," *Applied Physics Letters*, vol. 88, no. 21, 2006.

[70] J. O. Kim, S. Sengupta, A. V. Barve, Y. D. Sharma, S. Adhikary, S. J. Lee, S. K. Noh, M. S. Allen, J. W. Allen, S. Chakrabarti, and S. Krishna, "Multi-stack InAs/InGaAs sub-monolayer quantum dots infrared photodetectors," *Applied Physics Letters*, vol. 102, no. 1, 2013.

[71] S. Fafard, Z. R. Wasilewski, C. N. Allen, D. Picard, M. Spanner, J. P. McCaffrey, and P. G. Piva, "Manipulating the energy levels of semiconductor quantum dots," *Phys. Rev. B*, vol. 59, pp. 15 368–15 373, 1999.

[72] S. Fafard, Z. R. Wasilewski, C. N. Allen, D. Picard, M. Spanner, J. P. McCaffrey, and P. G. Piva, "Manipulating the energy levels of semiconductor quantum dots," *Phys. Rev. B*, vol. 59, pp. 15 368–15 373, 1999.

[73] A. F. Tsatsul'Nikov, B. V. Volovik, N. N. Ledentsov, M. V. Maximov, A. Egorov, A. R. Kovsh, V. M. Ustinov, A. E. Zhukov, P. S. Kop'Ev, Z. I. Alferov, I. A. Kozin, M. V. Belousov, I. P. Soshnikov, P. Werner, D. Litvinov, U. Fischer, A. Rosenauer, and D. Gerthsen, "Lasing in structures with InAs quantum dots in an (Al, Ga)As matrix grown by submonolayer deposition," *Journal of Electronic Materials*, vol. 28, no. 5, pp. 537–541, 1999.

[74] A. Lenz, H. Eisele, J. Becker, L. Ivanova, E. Lenz, F. Luckert, K. Ptschke, A. Strittmatter, U. W. Pohl, D. Bimberg, and M. Dhne, "Atomic structure of buried InAs sub-monolayer depositions in GaAs," *Applied Physics Express*, vol. 3, no. 10, p. 105602, 2010.

[75] P. Ballet, J. B. Smathers, and G. J. Salamo, "Morphology of InAs self-organized islands on AlAs surfaces," *Applied Physics Letters*, vol. 75, no. 3, pp. 337–339, 1999.

[76] P. M. Petroff, R. C. Miller, A. C. Gossard, and W. Wiegmann, "Impurity trapping, interface structure, and luminescence of GaAs quantum wells grown by molecular beam epitaxy," *Applied Physics Letters*, vol. 44, no. 2, pp. 217–219, 1984.

[77] C. Gmachl, F. Capasso, D. L. Sivco, and A. Cho, "Recent progress in quantum cascade lasers and applications," *Reports on Progress in Physics*, vol. 64, 2001.

[78] N. Bandyopadhyay, S. Slivken, Y. Bai, and M. Razeghi, "High power, continuous wave, room temperature operation of $\lambda = 3.4$ μm and $\lambda = 3.55$ μm inp-based quantum cascade lasers," *Applied Physics Letters*, vol. 100, 2012.

[79] R. Q. Yang, J. L. Bradshaw, J. D. Bruno, J. T. Pham, and D. E. Wortman, "Mid-infrared type-ii interband cascade lasers," *Quantum Electron*, vol. 38, 2002.

[80] I. Vurgaftman, C. L. Canedy, C. S. Kim, M. Kim, W. W. Bewley, J. R. Lindle, J. Abell, and J. R. Meyer, "Mid-infrared interband cascade lasers operating at ambient temperatures," *New Journal of Physics*, vol. 11, 2009.

[81] R. M. Biefeld, S. R. Kurtz, and A. A. Allerman, "The metal-organic chemical vapor deposition growth and properties of InAsSb mid-infrared (3-6 μm) lasers and LEDs," *IEEE Quantum Electron*, vol. 3, 1997.

[82] P. J. P. Tang, H. Hardaway, J. Heber, C. C. Phillips, M. J. Pullin, R. A. Stradling, W. T. Yuen, and L. Hart, "Efficient 300 K light-emitting diodes at $\lambda = 5$ and 8 μm from InAs/In(As1-xSbx) single quantum wells," *Applied Physics Letters*, vol. 72, 1998.

[83] D. Lackner, O. J. Pitts, M. Steger, A. Yang, M. L. W. Thewalt, and S. P. Watkins, "Strain balanced InAs/InAsSb superlattice structures with optical emission to 10 μm,," *Applied Physics Letters*, vol. 95, 2009.

[84] K. D. Moiseev, Y. A. Parkhomenko, A. V. Ankudinov, E. V. Gushchina, M. P. Mikhalova, A. N. Titkov, and Y. P. Yakovlev, "InSb–InAs quantum dots grown by liquid phase epitaxy,," *Tech. Phys. Lett.*, vol. 33, 2007.

[85] S. Shusterman, Y. Paltiel, A. Sher, V. Ezersky, and Y. Rosenwaks, "High-density nanometer-scale InSb dots formation using droplets heteroepitaxial growth by MOVPE,," *Journal of Crystal Growth*, vol. 291, 2006.

[86] F. Hatami, S. M. Kim, H. B. Yuen, and J. S. Harris, "InSb and InSb:N multiple quantum dots," *Applied Physics Letters*, vol. 89, 2005.

[87] S. V. Ivanov, A. N. Semenov, V. A. Solovev, O. G. Lyublinskaya, Y. V. Terentev, B. Y. Meltser, L. G. Prokopova, A. A. Sitnikova, A. A. Usikova, A. A. Toropov, and P. S. Kopev, "Molecular beam epitaxy of type ii InSb/InAs nanostructures with InSb sub-monolayers,," *Journal of Crystal Growth*, vol. 278, 2005.

[88] B. V. Olson, E. A. Kadlec, J. K. Kim, J. F. Klem, S. D. Hawkins, and E. A. Shaner, "Intensity- and temperature- dependent carrier recombination in InAs = InAsSb type-ii superlattices," *Physical Review Applied*, vol. 3, no. 044010, 2015.

[89] Q. Zhang, P. J. Carrington, and A. Krier, "Growth optimization of self-organized InSb-InAs quantum dots," *Journal of Physics D: Applied Physics*, vol. 41, no. 232003, pp. 4–8, 2008.

[90] K. Moiseev, Y. Parkhomenko, E. Gushchina, A. Ankudinov, V. Mikhailova, N. Bert, and Y. Yakovlev, "Specific features of the epitaxial growth of narrow-gap InSb quantum dots on an InAs substrate," *Semiconductors*, vol. 43, no. 4, pp. 1102–1109, 2009.

[91] B. R. Bennett and B. Shanabrook, *Molecular Beam Epitaxy of Sb-based Semiconductors*. Naval Research Laboratory, 1998.

[92] O. G. Lyublinskaya, V. A. Solovev, A. N. Semenov, B. Y. Meltser, Y. V. Terentev, L. A. Prokopova, A. A. Toropov, A. A. Sitnikova, O. V. Rykhova, S. V. Ivanov, K. Thonke, and R. Sauer, "Temperature-dependent photoluminescence from type-ii InSbInAs quantum dots," *Journal of Applied Physics*, vol. 99, no. 9, 2006.

[93] D. Jung, L. Yu, S. Dev, D. Wasserman, and M. L. Lee, "Room-temperature mid-infrared quantum well lasers on multi-functional metamorphic buffers," *Applied Physics Letters*, vol. 109, no. 21, 2016.

[94] C.-H. Chang, Z.-L. Li, C.-H. Pan, H.-T. Lu, C.-P. Lee, and S.-D. Lin, "Room-temperature mid-infrared m-type GaAsSb/InGaAs quantum well lasers on InP substrate," *Journal of Applied Physics*, vol. 115, no. 6, 2014.

[95] T. Sato, M. Mitsuhara, T. Kakitsuka, T. Fujisawa, and Y. Kondo, "Metalorganic vapor phase epitaxial growth of InAs/InGaAs multiple quantum well structures on InP substrates," *IEEE Journal of Selected Topics in Quantum Electronics*, vol. 14, no. 4, pp. 992–997, 2008.

[96] Y. Gu, Y. Zhang, Y. Cao, L. Zhou, X. Chen, H. Li, and S. Xi, "2.4 m InP-based antimony-free triangular quantum well lasers in continuous-wave operation above room temperature," *Applied Physics Express*, vol. 7, no. 3, 2014.

[97] C.-H. Chang, Z.-L. Li, C.-H. Pan, H.-T. Lu, C.-P. Lee, and S.-D. Lin, "Room-temperature mid-infrared m-type GaAsSb/InGaAs quantum well lasers on InP substrate," *Journal of Applied Physics*, vol. 115, no. 6, 2014.

[98] Y. Gu, Y. G. Zhang, Y. J. Ma, L. Zhou, X. Y. Chen, S. P. Xi, and B. Du, "InP-based type-I quantum well lasers up to 2.9μm at 230K in pulsed mode on a metamorphic buffer," *Applied Physics Letters*, vol. 106, no. 12, 2015.

[99] D. Jung, "Novel mid-infrared materials and devices grown on InP: from metamorphic lasers to self-assembled nanocomposites," Ph.D. dissertation, Univ. of Yale, Newark, 2016.

[100] S. Chuang, *Physics of Photonic Devices*. John Wiley and Sons. Inc, 2009.